Wide-Bandgap Halide Perovskite Materials for Photovoltaic and Optoelectronic Applications

Emil Grove Dyrvik

Linacre College

A thesis submitted for the degree of

Doctor of Philosophy

at the University of Oxford

Trinity Term 2023

Til mor og far

Abstract

With increasing global surface temperatures due to greenhouse gas emissions from human activity, the global society is in urgent need of pivoting the energy system towards low or zero-emission energy sources. Photovoltaic solar energy has the potential to deliver substantial emission reductions and is expected to make up a major portion of the energy mix in the remainder of the 21st century. Over the last decade, halide perovskite materials have shown great promise in bolstering and diversifying photovoltaic solar technologies, as well as the potential for efficient and colour-pure light-emitting diodes.

Leaps of progress have been made on halide perovskite-based single-junction and tandem solar cell technologies, but triple-junction solar cells, which theoretically could provide an even higher power conversion efficiency, are still in the infancy. For mainly perovskite-based triple-junctions to reach the highest realistic power conversion efficiencies, top cell bandgaps in the range 1.95 to 2.05 eV are required. Herein, we review the achievements and progress that have been made on the topic of perovskite triple-junction solar cells and the important wide-bandgap (2 eV) top cell. We then go on to characterize our $FAPb(Br_{0.7}I_{0.3})_3$-based 2.0 eV single-junction solar cells. We

identify the main reasons for V_{OC}-loss in these cells and look into the effect of halide segregation on the performance. Finding that nonradiative recombination in the bulk is the main cause of V_{OC}-loss and that halide segregation may be significantly more detrimental to the J_{SC} than the V_{OC}. Further, we investigate halide segregation and degradation trends in isolated films of this 2 eV material under the influence of different atmospheres. We observe untypical wavelength-shifts in the photoluminescence spectrum which may be linked to iodide-depletion under light exposure.

Finally, we improve the performance of our green perovskite LEDs by introducing a novel composite p-contact comprising the organic hole-transporting polymer TFB deposited by solution processing and Al_2O_3 deposited by atomic layer deposition. Due to the different chemical reactivity of the trimethyl aluminium precursor of the ALD process towards the oxide surface groups and the TFB polymer, the Al_2O_3 has the dual function of being able to insulate any bare patches of the underlying transparent conducting oxide electrode, which were not adequately covered during the TFB processing, and intergrow in the porosities of the TFB layer and cause a swelling, further blocking any potential nonradiative recombination sites.

Acknowledgements

So, at last, the thesis is mostly written and the time has come to put gratitude down on paper. Arguably the most difficult task of all, and it goes without saying that after 4 unforgettable years in this strange city, it will be impossible to list everyone who deserves a mention.

Let me start off by thanking all the friends, classmates, professors and PhD candidates at NTNU (and SINTEF and RWTH) that made the first chapter of my academic adventure so enjoyable and stimulating that towards the end of my studies, I was left without doubt that a PhD was the right next step. It definitely was, and I have never regretted, even at the lowest points of the PhD rollercoaster.

I am also incredibly grateful to Bjørn, the administration, the committee and all fellow scholars at Aker Scholarship, both for opening so many opportunities for my PhD adventure and for making me part of such a fantastic network of nice, diverse and driven people – an undepletable source of good conversations.

Thank you also to my supervisors, Henry and Robert, for taking me on and to help guide me through the science labyrinth. You both possess a contagious enthusiasm for science and I have been very lucky to have access to both of you, whether that be for

Henry's endless stream of experiment ideas or for guidance on scientific or academic topics from Robert.

Many other people in the Physics department deserve a mention. Clare, thank you for all the helpfulness, you are the cornerstone of the Snaith group and I am convinced it would be a fragile structure without you. Jonny, thank you for taking me under your wings and for being such a great colleague and teammate, mentoring a first-year student in that stressful third year must have been a daunting task but you did a great job. Manuel and Jarla for providing the best chat and company through all 4 years – although it is a shame you never ended the stay in Potsdam and came back to us, Jarla. Ben and Jake for making up Team 2eV on the ground. Alex, Robbie, Ashley, Harry, Suhas, Pietro and Joel for all the generous guidance and good discussions. Akash, for providing me with so many good excuses to procrastinate and banter, I have appreciated every distraction. Andreas and Mathias, for the Scandinavian interludes in this otherwise anglophone setting. Mike and Augustin for all you do to keep the lab running, you guys deliver way above expectation and create so much value for all of us. And to so many others that either have done, or still do, make the Snaith lab a good environment in both a scientific and social sense, including Bernard, James, Grey, Melissa, Heon, Florine, Tino, Shaoni, Philippe, David, Zhongcheng and more.

To the combined entity of the city of Oxford and the university and colleges for being such a magnificent place to spend formative years of one's youth. With its beautiful buildings, green spaces, many waterways, weird habits, particular events, good talks, great discussions, and infinite pool of interesting people, I could not imagine a better location to learn the art of research. I have learned a lot about solar cells and LEDs but even more about everything else in life and the universe.

In that environment, a particular heartfelt gratitude to the community of Linacre Boat Club. There are many deserving a mention, but I will reserve it for Lauren, Ashvina and Martin for being so pivotal in keeping both the boat club and my sanity afloat during that winter of 2020-21. You guys are amazing.

To the amazing housemates and friends that have been so important during both the great and the challenging times, be it due to pandemic or academia, in no particular order: Laura, Simon, Chloé M., Nick, Morgan, James, Valentin, Kumaran, Fabi, Felipe, Lisa, Anna, Marian, Simone, Ohad, Dina, Chloé B., Isabel, Fabiano and Emanuele.

To Irene, for all your love and support, for battling the pandemic together, for battling the PhD studies together, and for all the adventures you make me come along to. My Oxford experience would have been a lot more monotonous without you and I am endlessly grateful for you being there to shape the experience from the beginning!

Lastly, to my parents, for being such good role models, for encouraging me to follow my own way, and for always supporting me in my life choices.

Contents

List of Figures

List of Tables

List of Abbreviations

a-Si	amorphous silicon solar cells
AFM	atomic force microscopy
ALD	atomic layer deposition
ALD-Al_2O_3	Al_2O_3 deposited by ALD
AS-ALD	area-selective atomic layer deposition
BCP	2,9-dimethyl-4,7-diphenyl-1,10-phenanthroline, bathocuproine
c-Si	crystalline silicon solar cells
CdTe	cadmium telluride solar cells
CIGS	copper indium gallium diselenide solar cells
CTL	charge transport layer
EDS	energy dispersive X-ray spectroscopy
EL	electroluminescence
ETL	electron transport layer
EQE_{EL}	electroluminescent external quantum efficiency

EQE_{PV}	photovoltaic external quantum efficiency
FA	formamidinium
FF	fill factor
FTO	fluorine-doped tin oxide
FTPS	Fourier-transform photocurrent spectroscopy
HTL	hole transport layer
IoT	internet of things
ITO	indium-doped tin oxide
J_{mpp}	maximum power point current density
J_{SC}	short-circuit current density
JV	current density–voltage
JVL	current density–voltage–luminance
LED	light-emitting diode
LP	longpass
MA	methylammonium
Me-4PACz	(4-(3,6-dimethyl-9H-carbazol-9-yl)butyl)phosphonic acid
MPP	maximum power point
MPPT	maximum power point tracking
np-Al_2O_3	Al_2O_3 nanoparticles
OLED	organic light-emitting diode
OOE	optical outcoupling efficiency
PCBM	phenyl-C_{61}-butyric acid methyl ester
PCE	power conversion efficiency
PEABr	phenylethylammonium bromide
PeLED	perovskite light-emitting diode
PL	photoluminescence
PLQY	photoluminescent quantum yield

poly-TPD	poly(N,N'-bis-4-butylphenyl-N,N'-bisphenyl)benzidine
PSC	perovskite solar cells
PV	photovoltaics
QFLS	quasi-Fermi level splitting
RMS	root mean square (roughness)
SAM	self-assembled monolayer
SEM	scanning electron microscopy
SS	steady-state
TCO	transparent conducting oxide
TFB	poly(9,9-dioctylfluorene-alt-N-(4-sec-butylphenyl)-diphenylamine
TPBi	2,2',2"-(1,3,5-benzinetriyl)-tris(1-phenyl-1-H-benzimidazole)
$\mathbf{V_{mpp}}$	maximum power point voltage
$\mathbf{V_{OC}}$	open circuit voltage
XRD	X-ray diffraction
XRR	X-ray reflectivity

CHAPTER 1

Introduction

1.1 Global Warming

127 years ago, the Swedish physicist Svante Arrhenius published the article *On the influence of carbonic acid in the air upon the temperature of the ground*, where he calculated that a doubling of the concentration of CO_2 in the atmosphere would lead to a temperature increase between 5 to 6 °C.[1] In hindsight, this could be seen as the first warning of man-made climate change (due to the use of, for example, fossil fuels), however, the criticality of a global warming was not really observed at the time.

Over the decades since, concerns about man-made climate change from greenhouse gas emissions and the role of fossil fuels has increased. The intermediate scenario (SSP2-4.5) in the latest report from the Intergovernmental Panel on Climate Change[2], where global greenhouse gas emissions continue a gradual increase until starting to decrease in the 2040s, predicts a "very likely" global surface temperature at the end of the century that is 2.1 to 3.5 °C higher than the average of the years 1850 to 1900. At such a temperature, the Arctic sea is predicted to be practically ice-free (in

September) and extreme heat waves that previously would occur every tenth year are expected to occur every second year and to be more intense. (See also Figure 1.1.)

On the other hand, to reach the target stipulated in the Paris agreement of *"holding the increase in the global average temperature to well below 2 °C above pre-industrial levels and pursuing efforts to limit the temperature increase to 1.5 °C above pre-industrial levels,"*[4] the modelling shows that immediate and sustained reduction in global greenhouse gas emissions are needed, with a reduction from an estimated 55 Gt CO_2-eq yr^{-1} in 2019 to 31 Gt CO_2-eq yr^{-1} in 2030 and 9 Gt CO_2-eq yr^{-1} in 2050.[5] Cuts have to come from a broad spectrum of sectors, but notably, solar and wind energy have the potential to contribute to more than 8 Gt CO_2-eq yr^{-1} worth of reductions by 2030 – a third of the required reductions![6] Similar messages have been repeated for years.[7]

Widespread action to reduce dependence on fossil fuels and replace it with green, renewable energy sources has, nevertheless, delayed to our present time. In 2021, the global primary energy share from fossil fuels was still at 79 %.[8] Electric cars made up only 4.6 % of the cars sold globally in 2020.[9]

1.2 Renewable Energy Sources

In spite of the clear necessity, a deployment in the order of 100 EJ (>27000 TWh)[10] of low-emission energy production by 2030 is not entirely uncontroversial either. Any industrial installation comes with environmental impact, and each renewable energy source has its controversies. The four largest non-fossil fuel energy sources are nuclear, wind, hydro and solar power.[11] Conventional nuclear power produces radioactive waste that necessitates careful and costly handling and storage, and carry a risk of nuclear meltdown that can lead to nuclear disasters.[12] (The discussion whether or not nuclear power can be considered a renewable energy source is omitted.) Many hydro power projects include damming of watercourses into large reservoirs during the construction phase, with following unnatural variations in water flow rates in the lower-lying part

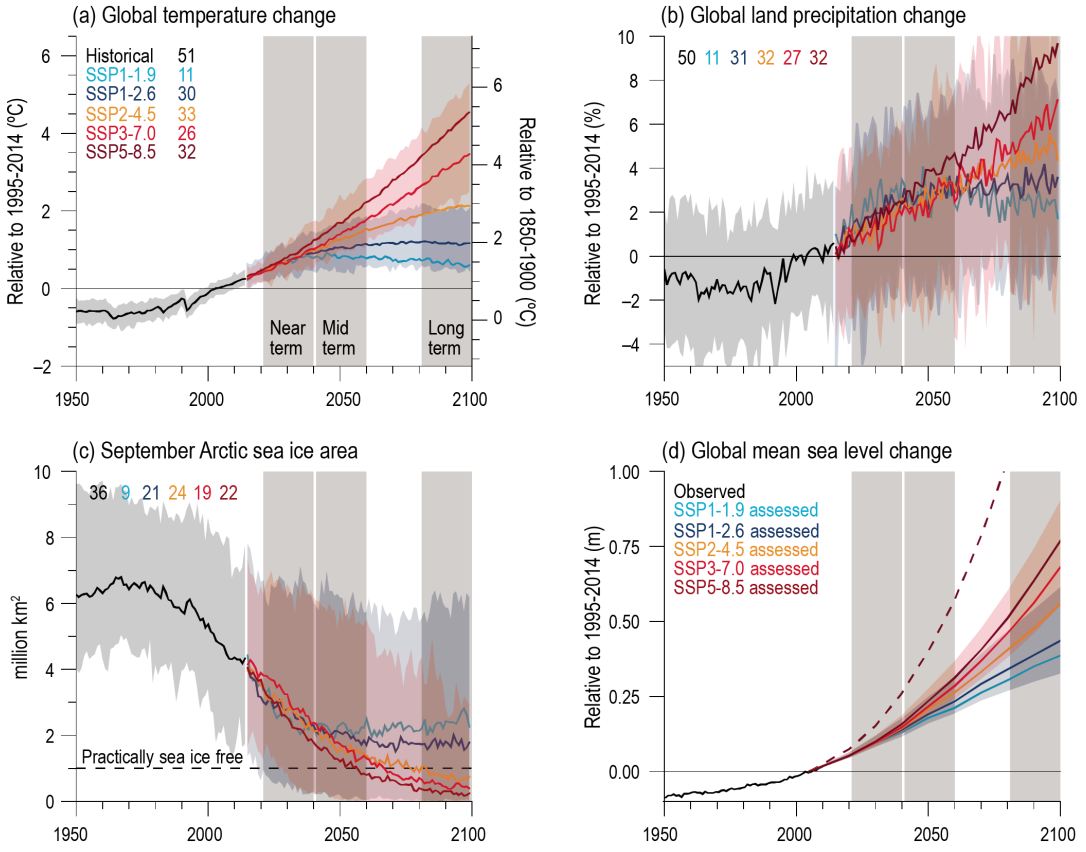

Figure 1.1: Selected indicators of global climatechange from CMIP6 historical and scenario simulations. (a) Global surface air temperature changes relative to the 1995–2014 average (left axis) and relative to the 1850–1900 average (right axis; offset by 0.82 °C, which is the multi-model mean and close to observed best estimate, Cross-Chapter Box 2.1, Table 1). (b) Global land precipitation changes relative to the 1995–2014 average. (c) September Arctic sea ice area. (d) Global mean sea level (GMSL) change relative to the 1995–2014 average. (a), (b) and (d) are annual averages, (c) are September averages. In (a–c), the curves show averages over the CMIP6 simulations, the shadings around the SSP1-2.6 and SSP3-7.0 curves show 5–95 % ranges, and the numbers near the top show the number of model simulations used. Results are derived from concentration-driven simulations. In (d), the barystatic contribution to GMSL (i.e., the contribution from land-ice melt) has been added offline to the CMIP6 simulated contributions from thermal expansion (thermosteric). The shadings around the SSP1-2.6 and SSP3-7.0 curves show 5–95 % ranges. The dashed curve is the low confidence and low likelihood outcome at the high end of SSP5-8.5 and reflects deep uncertainties arising from potential ice-sheet and ice-cliff instabilities. This curve at year 2100 indicates 1.7 m of GMSL rise relative to 1995–2014. Reproduced with permission from [3].

of the watercourse during operation, both having negative consequences on the local environment. Wind power is estimated to cause between 0.95 and 11.67 deaths of birds per MW per year due to impact with the rotating blades, as an example of one ecological impact during operation.[13] Installation and maintenance also involve ecosystem modifications and a non-negligible environmental impact. In addition to this, when built in the vicinity of human settlement, both visual and noise pollution can cause significant controversy.

Perhaps the least environmentally invasive of these "big four" is solar power. Of the two main categories, thermal and photovoltaic solar power, photovoltaic solar power is of the higher relevance to this thesis and we will leave thermal solar with only this mention. Photovoltaic solar power, unlike the 3 big rivals previously mentioned, does not produce harmful radioactive waste, nor does it lethally impact local wildlife during operation, nor cause noise pollution. (The visual pollution by solar cells is, however, arguable.) The main environmental impact of (conventional, silicon) solar cells comes from the mining of the raw materials, as well as the chemical and energy use during the production stage.[14] The negative environmental impact of photovoltaic solar power during installation and operation is limited, except if placed directly on arable land or if land is cleared for establishing solar farms. At the end-of-life, solar modules will have to be effectively recycled in order to prevent large masses ending up in landfill. Because of the long operative lifetime of commercial solar cells, relatively low amounts of solar installations have reached the end-of-life stage yet, but 8 Mt cumulative mass of end-of-life PV modules are projected by 2030, and 80 Mt by 2050.[15] Currently, bulk mass such as the glass packaging, aluminium frames and external copper wires are recycled, whereas recycling of the more valuable materials contained in individual cells (silver, copper, lead, and silicon wafer) is limited and under development.[15] On the positive side, solar cells can be placed on a multitude of already developed areas such as roofs and facades of buildings, on top of vehicles such as cars, trains, drones or airplanes (if sufficiently lightweight), and in dual-use situations such as solar canopies or as beneficial shading over agricultural crops. Another advantage of photovoltaic

solar energy is that it is inherently predictable. It might not be sunny every day, but there is daylight at predictable times daily and weather forecasts can be used to predict variations in power output.

1.3 Photovoltaic Solar Power Technologies

Presently available, crystalline silicon-based (c-Si) photovoltaics (PV) technologies are already commercially and technologically viable for many of these purposes. However, despite the falling cost of c-Si, the research community has looked for decades for an even cheaper alternative: A technology comprising abundant and cheap raw materials, low energy-need during fabrication, and processability in very thin layers. So called "thin-film" solar cells. Many technologies have been developed for decades, including cadmium telluride cells (CdTe), copper indium gallium diselenide cells (CIGS) and amorphous silicon cells (a-Si).[16] However, during the rapid increase in PV installations in the last decade, no thin-film technology has managed to seriously challenge the market share of c-Si and make its mark on the industry. In 2021, thin-film market share was at 5 %, down from 30 % at the end of the 1980s in an almost continuous decline.[17] This might be about to change. Since halide perovskites (from now on only referred to as "perovskites") were identified as a promising material for photovoltaics in the turn of the 2000s to 2010s,[18–21] developments have been moving fast.

Although the structural and optoelectronic properties of this class of materials had briefly been investigated previously,[22–37] perovskites first seriously came into the attention of the PV community when applied as sensitizers in dye-sensitized solar cells in a report in 2009.[18] Within only a few years, the potential for perovskites as the standalone absorber of the solar cell in a more conventional thin-film architecture, without mesoporous charge separation and transport scaffolds, became clear.[38] This kickstarted a renaissance for photovoltaic and optoelectronic research on perovskites which has resulted in thousands of research articles published yearly.[39]

1.4 The Potential for Perovskite Photovoltaics

Perovskite PV ticks many of the boxes of the perfect thin-film PV technology. Low-temperature, low-cost fabrication,[40–42] abundant materials,[43] and strong absorption[44] at sub-micron thicknesses combined with long carrier diffusion lengths[45], which has resulted in incredible efficiencies in a short timeframe.[46] (However, efficiencies over large-area cell sizes and modules still lag behind chalcogenide thin-film technologies.)[47–49] On the road to commercialization, two routes stand out as more obvious to the author: the silicon-perovskite tandem cell, and the lightweight and/or flexible perovskite cell.

Perovskite materials have a lot of synergy potential with existing silicon PV. Because the bandgap of perovskite materials can be tuned over a wide range with high accuracy,[50] development of absorbers with ideal bandgap for a tandem cell with a silicon bottom cell is attainable. An obvious commercial route is thus to take advantage of the already large, existing c-Si value chain and, with relatively small modifications and additions to the conventional c-Si manufacturing process, fabricate perovskite cells on top of the c-Si bottom cells in a (monolithic) tandem configuration. This offers a way to increase the power output per area of "conventional" solar module technologies at low added manufacturing cost, and take a market share in the rooftop PV market, where particularly area is at a premium.[43] For the c-Si industry, silicon–perovskite tandems could be a natural next step for continued acceleration of PV deployment through increased module efficiency, following the currently ongoing roll-out of technologies based on n-type Si, such as "Tunnel Oxide Passivated Contact" (TOPCon) and "Interdigitated Back Contact" (IBC) architectures.[51]

Since perovskite solar cells already deliver solar energy conversion at a very high efficiency on their own in single-junction configuration[46], (and also in perovskite–perovskite and CIGS–perovskite tandem structures,[52,53]) the obvious alternative to silicon–perovskite PV is to develop a perovskite PV value chain that is separate to the silicon PV value chain. However, competing with the already existing c-Si value chain

that has been optimized for decades would require massive investment. It therefore makes more sense to develop perovskite PV for niche markets where c-Si is less suitable and less widespread. Three such niches could be: *(i)* Flexible solar cells, which in theory could be incorporated on any surface without a pre-defined required shape for the module to be designed in. The thin-film processability of perovskite PV on bendable polymer substrates makes this a possibility. *(ii)* Applications where light weight is essential, such as aerospace applications like drones or airplanes. Again, this is a property that perovskite PV owes to it's thin-film processing.[54,55] *(iii)* Indoor light-harvesting (for e.g. internet of things (IoT)), which requires bandgaps much wider than that of c-Si due to the bluer and narrower spectra of non-halogen based indoor light sources compared to the solar spectrum.[56]

Some key challenges still remain to be addressed for perovskite PV to make a commercial breakthrough. The main being stability, efficiency over large areas, and reproducible manufacturing in higher volumes.[47] Efficiency-wise, single-junction perovskite cells[57] and silicon–perovskite tandems[58] have already come a long way in development, but all-perovskite tandems still do not significantly outperform their single-junction counterparts. The development of triple-junction devices (for example, silicon–perovskite–perovskite or all-perovskite), which in the future could be a low-cost competitor to high-efficiency III–V technology multijunction cells, is still in its infancy.

Environmental concerns have been raised over the presence of Pb, a toxic but essential element in high-efficiency perovskite solar cells. However, most c-Si solar panels today contain Pb in the solders or front contact, on the order of 10 g Pb per panel,[59] whereas the Pb weight in the perovskite layer of a solar panel would be on the order of 1 g Pb per panel.[60] Even if all the Pb in the perovskite of a panel was to leach out into the nearby soil, it would not raise the Pb content of the soil above common background levels.[61] However, on the same note, establishing good recollection and recycling procedures will be important to avoid valuable resources like lead, indium and noble metals ending in landfills, where larger amounts of Pb could cause environmental problems if leached out in the long-term. Recycling of

all-perovskite thin-film solar modules could be comparable to the recycling of CdTe modules, which have been effectively recycled since 2005.[62] With silicon–perovskite tandems, the perovskite cell adds one or more layers of complexity to the recycling process. Advantageously, the perovskite layer can be dissolved in a variety of solvents, and the recycling of perovskite solar cells is a topic under active research.[63]

1.5 Perovskite Light-emitting Diodes

Following the enormous interest garnered in perovskite PV, other applications of halide perovskites have also caught the attention of the research field. One such application, and perhaps the closest related to photovoltaic cells, is that of light-emitting diodes (LEDs). Since the first room-temperature perovskite LED was reported in 2014,[64] the perovskite LED (PeLED) field has grown to become a large field of research in itself. Commercially, perovskites are investigated as colour-conversion phosphors or LEDs in displays for e.g. smart phones, computers and televisions.[65] The properties that make perovskites desirable for these technologies are the narrow emission bandwidth as well as the bandgap tunability, which enable a wider colour gamut than current commercial competitors. The good absorption properties of perovskites also allows the use of very thin colour-conversion films, which both lowers material use (and thus cost) and enables higher-resolution patterning which is required for high-resolution applications such as near-eye displays.[65] However, like for perovskite PV, the operational stability of perovskite LEDs and technologies for reproducible, large-volume production are key challenges that need to be resolved to make it onto the commercial market.[65]

1.6 Material Properties of Halide Perovskites

Halide perovskite materials are characterized by being crystallized in the ABX_3 "perovskite" crystal structure (Figure 1.2), where the anion (X) is one of the halides I^-, Br^- or Cl^-. On the B location in the unit cell sits a divalent cation, often a relatively heavy cation such as Pb^{2+} or Sn^{2+}. The A-site hosts a monovalent cation among a

range of organic and inorganic candidates, where the most common in perovskite PV are methylammonium (MA), formamidinium (FA) and Cs^+. Lead halide perovskites are direct bandgap semiconductors with low exciton binding energies, where the A-site cations do not participate in bonding and the top of the valence band is dominated by *p*-states from the anion (and some Pb-*s* states) while the bottom of the conduction band is of Pb-*p* and I-*p* character.[66] The exact energetic positioning of the band edges depend on which halides occupy the X-sites, providing ample room for bandgap tunability.

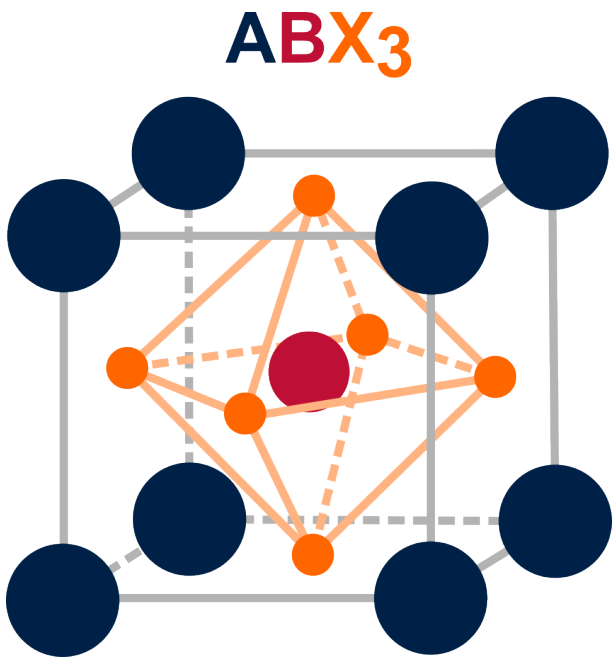

Figure 1.2: Schematic of the ABX_3 "perovskite" unit cell.

1.7 Scope of this Thesis

The scope of this thesis is two-folded. The majority of the chapters dwell on the topic of halide perovskite absorbers with bandgap around 2.0 eV for use in solar cells, with the overarching goal of improving the understanding of performance-limiting mechanisms in these materials and achieve performance improvements. This again is motivated by the long-term goal of enabling highly efficient triple-junction solar cells

at low cost. The other aspect of the thesis is the topic of halide perovskite-based LEDs, with an engineering-oriented focus at improving device performance.

Chapter 2 presents a literature study on perovskite triple-junctions, 2 eV material development, and halide segregation, as well as a theoretical introduction to important relations used for quantifications in Chapter 4.

Chapter 3 provides details of all experimental methods used.

Chapter 4 deals with the quantification of loss types in our 2 eV solar cells, with a particular focus on V_{OC} loss.

Chapter 5 inspects the evolution of photoluminescence under the course of halide segregation in 2 eV materials over prolonged times in various atmospheres and looks at the connection to degradation that occurs.

Chapter 6 presents a novel hole-selective contact for perovskite LEDs using a combination of an organic hole transporting polymer and atomic layer deposition of the insulator Al_2O_3.

References

1. S. Arrhenius, "XXXI. On the influence of carbonic acid in the air upon the temperature of the ground," *The London, Edinburgh, and Dublin Philosophical Magazine and Journal of Science*, vol. 41, no. 251, pp. 237–276, 1896.

2. Intergovernmental Panel on Climate Change, "IPCC, 2021: Summary for Policymakers," in *Climate Change 2021: The Physical Science Basis. Contribution of Working Group I to the Sixth Assessment Report of the Intergovernmental Panel on Climate Change* (V. Masson-Delmotte, P. Zhai, A. Pirani, S. Connors, C. Péan, S. Berger, N. Caud, Y. Chen, L. Goldfarb, M. Gomis, M. Huang, K. Leitzell, E. Lonnoy, J. Matthews, T. Maycock, T. Waterfield, O. Yelekçi, R. Yu, and B. Zhou, eds.), pp. 13–14, Cambridge, United Kingdom and New York, NY, USA: Cambridge University Press, 2021.

3. Intergovernmental Panel on Climate Change, "IPCC, 2021: Chapter 4. Future Global Climate: Scenario-Based Projections and Near-Term Information. (Figure 4.2)," in *Climate Change 2021: The Physical Science Basis. Contribution of Working Group I to the Sixth Assessment Report of the Intergovernmental Panel on Climate Change* (V. Masson-Delmotte, P. Zhai, A. Pirani, S. Connors, C. Péan, S. Berger, N. Caud, Y. Chen, L. Goldfarb, M. Gomis, M. Huang, K. Leitzell, E. Lonnoy, J. Matthews, T. Maycock, T. Waterfield, O. Yelekçi, R. Yu, and B. Zhou, eds.), p. 571, Cambridge, United Kingdom and New York, NY, USA: Cambridge University Press, 2021.

4. United Nations Framework Convention on Climate Change, "Paris Agreement." `https://www.un.org/en/climatechange/paris-agreement`, 2016. Accessed: 2023-06-27.

5. Intergovernmental Panel on Climate Change, "IPCC, 2022: Summary for Policymakers (Table SPM.2)," in *Climate Change 2022: Mitigation of Climate Change. Contribution of Working Group III to the Sixth Assessment Report of the Intergovernmental Panel on Climate Change* (P. Shukla, J. Skea, R. Slade, A. Al Khourdajie, R. van Diemen, D. McCollum, M. Pathak, S. Some, P. Vyas, R. Fradera, M. Belkacemi, A. Hasija, G. Lisboa, S. Luz, and J. Malley, eds.), pp. 18–19, Cambridge, UK and New York, NY, USA: Cambridge University Press, 2022.

6. Intergovernmental Panel on Climate Change, "IPCC, 2022: Summary for Policymakers (Figure SPM.7)," in *Climate Change 2022: Mitigation of Climate Change. Contribution of Working Group III to the Sixth Assessment Report of the Intergovernmental Panel on Climate Change* (P. Shukla, J. Skea, R. Slade, A. Al Khourdajie, R. van Diemen, D. McCollum, M. Pathak, S. Some, P. Vyas, R. Fradera, M. Belkacemi, A. Hasija, G. Lisboa, S. Luz, and J. Malley, eds.), p. 38, Cambridge, UK and New York, NY, USA: Cambridge University Press, 2022.

References

7. Intergovernmental Panel on Climate Change, "Policymakers Summary," in *IPCC 1990 FAR - Working Group III: The IPCC Response Strategies* (F. Bernthal, E. Dowdeswell, J. Luo, D. Attard, P. Vellinga, and R. Karimanzira, eds.), Cambridge, United Kingdom: Cambridge University Press, 1990.
8. International Energy Agency, "Table 5.1," in *World Energy Outlook 2022*, p. 239, Paris: OECD Publishing, 2022.
9. International Energy Agency, "Executive Summary," in *Global EV Outlook 2021: Accelerating ambitions despite the pandemic*, pp. 4–7, Paris: OECD Publishing, 2021.
10. International Energy Agency, "Figure 3.3," in *World Energy Outlook 2022*, p. 128, Paris: OECD Publishing, 2022.
11. International Energy Agency, "Table 6.1," in *World Energy Outlook 2022*, p. 281, Paris: OECD Publishing, 2022.
12. F. von Hippel, M. G. Bunn, A. Diakov, M. Ding, T. Katsuta, C. McCombie, M. Ramana, T. Suzuki, S. Voss, and S. Yu, "The Uncertain Future of Nuclear Energy," tech. rep., International Panel on Fissile Materials, 2010.
13. Intergovernmental Panel on Climate Change, "Renewable Energy Sources and Climate Change Mitigation: Special Report of the Intergovernmental Panel on Climate Change," p. 100, Cambridge: Cambridge University Press, 2011.
14. Intergovernmental Panel on Climate Change, "Renewable Energy Sources and Climate Change Mitigation: Special Report of the Intergovernmental Panel on Climate Change," p. 66, Cambridge: Cambridge University Press, 2011.
15. G. A. Heath, T. J. Silverman, M. Kempe, M. Deceglie, D. Ravikumar, T. Remo, H. Cui, P. Sinha, C. Libby, S. Shaw, K. Komoto, K. Wambach, E. Butler, T. Barnes, and A. Wade, "Research and development priorities for silicon photovoltaic module recycling to support a circular economy," *Nat Energy*, vol. 5, no. 7, pp. 502–510, 2020.
16. R. Birkmire, "Thin-Film Solar Cells and Modules," in *Solar Cells and their Applications*, ch. 6, pp. 137–157, John Wiley & Sons, Ltd, 2010.
17. S. Philipps and W. Warmuth, "Photovoltaics report," tech. rep., Fraunhofer ISE and PSE Projects GmbH, 2023.
18. A. Kojima, K. Teshima, Y. Shirai, and T. Miyasaka, "Organometal Halide Perovskites as Visible-Light Sensitizers for Photovoltaic Cells," *J. Am. Chem. Soc.*, vol. 131, no. 17, pp. 6050–6051, 2009.
19. J.-H. Im, C.-R. Lee, J.-W. Lee, S.-W. Park, and N.-G. Park, "6.5% efficient perovskite quantum-dot-sensitized solar cell," *Nanoscale*, vol. 3, no. 10, pp. 4088–4093, 2011.
20. M. M. Lee, J. Teuscher, T. Miyasaka, T. N. Murakami, and H. J. Snaith, "Efficient Hybrid Solar Cells Based on Meso-Superstructured Organometal Halide Perovskites," *Science*, vol. 338, no. 6107, pp. 643–647, 2012.
21. H.-S. Kim, C.-R. Lee, J.-H. Im, K.-B. Lee, T. Moehl, A. Marchioro, S.-J. Moon, R. Humphry-Baker, J.-H. Yum, J. E. Moser, M. Grätzel, and N.-G. Park, "Lead Iodide Perovskite Sensitized All-Solid-State Submicron Thin Film Mesoscopic Solar Cell with Efficiency Exceeding 9%," *Sci Rep*, vol. 2, no. 1, p. 591, 2012.
22. D. Weber, "CH $_3$ NH $_3$ PbX $_3$, ein Pb(II)-System mit kubischer Perowskitstruktur / CH $_3$ NH $_3$ PbX $_3$, a Pb(II)-System with Cubic Perovskite Structure," *Zeitschrift für Naturforschung B*, vol. 33, no. 12, pp. 1443–1445, 1978.
23. A. Poglitsch and D. Weber, "Dynamic disorder in methylammoniumtrihalogenoplumbates (II) observed by millimeter-wave spectroscopy," *J. Chem. Phys.*, vol. 87, no. 11, pp. 6373–6378,

1987.

24. M. Hirasawa, T. Ishihara, T. Goto, K. Uchida, and N. Miura, "Magnetoabsorption of the lowest exciton in perovskite-type compound (CH3NH3)PbI3," *Physica B: Condensed Matter*, vol. 201, pp. 427–430, 1994.

25. M. Hirasawa, T. Ishihara, and T. Goto, "Exciton Features in 0-, 2-, and 3-Dimensional Networks of [PbI6]4- Octahedra," *J. Phys. Soc. Jpn.*, vol. 63, no. 10, pp. 3870–3879, 1994.

26. D. B. Mitzi, C. A. Feild, W. T. A. Harrison, and A. M. Guloy, "Conducting tin halides with a layered organic-based perovskite structure," *Nature*, vol. 369, no. 6480, pp. 467–469, 1994.

27. D. B. Mitzi, S. Wang, C. A. Feild, C. A. Chess, and A. M. Guloy, "Conducting Layered Organic-inorganic Halides Containing ⟨110⟩-Oriented Perovskite Sheets," *Science*, vol. 267, pp. 1473–1476, 1995.

28. D. B. Mitzi, C. A. Feild, Z. Schlesinger, and R. B. Laibowitz, "Transport, Optical, and Magnetic Properties of the Conducting Halide Perovskite CH3NH3SnI3," *Journal of Solid State Chemistry*, vol. 114, no. 1, pp. 159–163, 1995.

29. H. Ishida, H. Maeda, A. Hirano, Y. Kubozono, and Y. Furukawa, "Local Structures around Pb(II) and Sn(II) in CH3NH3PbX3 (X = Cl, Br, I) and CH3NH3SnX3 (X = Br, I) Studied by Pb LIII-Edge and Sn K-Edge EXAFS," *physica status solidi (a)*, vol. 159, no. 2, pp. 277–282, 1997.

30. M. Maeda, M. Hattori, A. Hotta, and I. Suzuki, "Dielectric Studies on CH 3NH 3PbX 3 (X = Cl and Br) Single Cystals," *J. Phys. Soc. Jpn.*, vol. 66, no. 5, pp. 1508–1511, 1997.

31. K. Gesi, "Effect of hydrostatic pressure on the structural phase transitions in CH3NH3PbX3 (X = Cl, Br, I)," *Ferroelectrics*, vol. 203, no. 1, pp. 249–268, 1997.

32. Y. Kawamura, H. Mashiyama, and K. Hasebe, "Structural Study on Cubic–Tetragonal Transition of CH3NH3PbI3," *J. Phys. Soc. Jpn.*, vol. 71, no. 7, pp. 1694–1697, 2002.

33. L. Chi, I. Swainson, L. Cranswick, J.-H. Her, P. Stephens, and O. Knop, "The ordered phase of methylammonium lead chloride CH3ND3PbCl3," *Journal of Solid State Chemistry*, vol. 178, no. 5, pp. 1376–1385, 2005.

34. K. Matsuishi, T. Ishihara, S. Onari, Y. H. Chang, and C. H. Park, "Optical properties and structural phase transitions of lead-halide based inorganic–organic 3D and 2D perovskite semiconductors under high pressure," *physica status solidi (b)*, vol. 241, no. 14, pp. 3328–3333, 2004.

35. M. Shimizu, J.-I. Fujisawa, and J. Ishi-Hayase, "Influence of dielectric confinement on excitonic nonlinearity in inorganic-organic layered semiconductors," *Phys. Rev. B*, vol. 71, no. 20, p. 205306, 2005.

36. Y. Takeoka, K. Asai, M. Rikukawa, and K. Sanui, "Systematic Studies on Chain Lengths, Halide Species, and Well Thicknesses for Lead Halide Layered Perovskite Thin Films," *BCSJ*, vol. 79, no. 10, pp. 1607–1613, 2006.

37. H. Mashiyama, Y. Kawamura, H. Kasano, T. Asahi, Y. Noda, and H. Kimura, "Disordered Configuration of Methylammonium of CH3NH3PbBr3 Determined by Single Crystal Neutron Diffractometry," *Ferroelectrics*, vol. 348, no. 1, pp. 182–186, 2007.

38. J. M. Ball, M. M. Lee, A. Hey, and H. J. Snaith, "Low-temperature processed meso-superstructured to thin-film perovskite solar cells," *Energy & Environmental Science*, vol. 6, no. 6, pp. 1739–1743, 2013.

39. A. S. Shikoh and A. Polyakov, "A Quantitative Analysis of the Research Trends in Perovskite Solar Cells in 2009–2019," *physica status solidi (a)*, vol. 217, no. 23, p. 2000441, 2020.

References

40. X. Tian, S. D. Stranks, and F. You, "Life cycle energy use and environmental implications of high-performance perovskite tandem solar cells," *Science Advances*, vol. 6, no. 31, p. eabb0055, 2020.

41. B. Smith, M. Woodhouse, K. Horowitz, T. Silverman, J. Zuboy, and R. Margolis, "Photovoltaic (PV) Module Technologies: 2020 Benchmark Costs and Technology Evolution Framework Results," Tech. Rep. NREL/TP-7A40-78173, 1829459, MainId:32082, National Renewable Energy Lab. (NREL), 2021.

42. M. Roffeis, S. Kirner, J.-C. Goldschmidt, B. Stannowski, L. Miranda Perez, C. Case, and M. Finkbeiner, "New insights into the environmental performance of perovskite-on-silicon tandem solar cells – a life cycle assessment of industrially manufactured modules," *Sustainable Energy & Fuels*, vol. 6, no. 12, pp. 2924–2940, 2022.

43. C. Kamaraki, M. T. Klug, T. Green, L. Miranda Perez, and C. Case, "Perovskite/silicon tandem photovoltaics: Technological disruption without business disruption," *Appl. Phys. Lett.*, vol. 119, no. 7, p. 070501, 2021.

44. W.-J. Yin, T. Shi, and Y. Yan, "Unique Properties of Halide Perovskites as Possible Origins of the Superior Solar Cell Performance," *Advanced Materials*, vol. 26, no. 27, pp. 4653–4658, 2014.

45. S. D. Stranks, G. E. Eperon, G. Grancini, C. Menelaou, M. J. P. Alcocer, T. Leijtens, L. M. Herz, A. Petrozza, and H. J. Snaith, "Electron-Hole Diffusion Lengths Exceeding 1 Micrometer in an Organometal Trihalide Perovskite Absorber," *Science*, vol. 342, no. 6156, pp. 341–344, 2013.

46. National Renewable Energy Laboratory, "Best research-cell efficiency chart," 2023. Accessed: 2023-06-26.

47. T. D. Siegler, A. Dawson, P. Lobaccaro, D. Ung, M. E. Beck, G. Nilsen, and L. L. Tinker, "The Path to Perovskite Commercialization: A Perspective from the United States Solar Energy Technologies Office," *ACS Energy Lett.*, vol. 7, no. 5, pp. 1728–1734, 2022.

48. National Renewable Energy Laboratory, "Champion photovoltaic module efficiency chart," 2023. Accessed: 2023-06-26.

49. Y. Cheng, Y. Peng, A. K.-Y. Jen, and H.-L. Yip, "Development and Challenges of Metal Halide Perovskite Solar Modules," *Solar RRL*, vol. 6, no. 3, p. 2100545, 2022.

50. G. E. Eperon, S. D. Stranks, C. Menelaou, M. B. Johnston, L. M. Herz, and H. J. Snaith, "Formamidinium lead trihalide: a broadly tunable perovskite for efficient planar heterojunction solar cells," *Energy Environ. Sci.*, vol. 7, no. 3, p. 982, 2014.

51. Radovan Kopecek, Florian Buchholz, Valentin D. Mihailetchi, Joris Libal, Ning Chen, Haifeng Chu, Christoph Peter, Dominik Rudolph, Razvan Roescu, Pirmin Preis, Lejo J. Koduvelikulathu, Tom Kollek, Thomas Buck, Jan Lossen, Tudor Timofte, and Andreas Halm, "Why TBC will follow shortly after TOPCon." `https://www.pv-tech.org/why-tbc-will-follow-shortly-after-topcon/`, 2023.

52. R. Lin, J. Xu, M. Wei, Y. Wang, Z. Qin, Z. Liu, J. Wu, K. Xiao, B. Chen, S. M. Park, G. Chen, H. R. Atapattu, K. R. Graham, J. Xu, J. Zhu, L. Li, C. Zhang, E. H. Sargent, and H. Tan, "All-perovskite tandem solar cells with improved grain surface passivation," *Nature*, vol. 603, no. 7899, pp. 73–78, 2022.

53. M. Jošt, E. Köhnen, A. Al-Ashouri, T. Bertram, Š. Tomšič, A. Magomedov, E. Kasparavicius, T. Kodalle, B. Lipovšek, V. Getautis, R. Schlatmann, C. A. Kaufmann, S. Albrecht, and M. Topič, "Perovskite/CIGS Tandem Solar Cells: From Certified 24.2% toward 30% and Beyond," *ACS Energy Lett.*, vol. 7, no. 4, pp. 1298–1307, 2022.

54. H. S. Jung, G. S. Han, N.-G. Park, and M. J. Ko, "Flexible Perovskite Solar Cells," *Joule*, vol. 3, no. 8, pp. 1850–1880, 2019.

55. Y. Hu, T. Niu, Y. Liu, Y. Zhou, Y. Xia, C. Ran, Z. Wu, L. Song, P. Müller-Buschbaum, Y. Chen, and W. Huang, "Flexible Perovskite Solar Cells with High Power-Per-Weight: Progress, Application, and Perspectives," *ACS Energy Lett.*, vol. 6, no. 8, pp. 2917–2943, 2021.

56. I. Mathews, S. N. Kantareddy, T. Buonassisi, and I. M. Peters, "Technology and Market Perspective for Indoor Photovoltaic Cells," *Joule*, vol. 3, no. 6, pp. 1415–1426, 2019.

57. Solarquarter, "UNIST Scientists Develop Technology for Highly Efficient Perovskite Solar Cells." `https://solarquarter.com/2023/03/03/unist-scientists-develop-technology-for-highly-efficient-perovskite-solar-cells/`, 2023. Accessed: 2023-06-27.

58. pv magazine, "KAUST claims 33.7% efficiency for perovskite/silicon tandem solar cell." `https://www.pv-magazine.com/2023/05/30/kaust-claims-33-7-efficiency-for-perovskite-silicon-tandem-solar-cell/`, 2023. Accessed: 2023-06-27.

59. O. Malandrino, D. Sica, M. Testa, and S. Supino, "Policies and Measures for Sustainable Management of Solar Panel End-of-Life in Italy," *Sustainability*, vol. 9, no. 4, p. 481, 2017.

60. D. Fabini, "Quantifying the Potential for Lead Pollution from Halide Perovskite Photovoltaics," *J. Phys. Chem. Lett.*, vol. 6, no. 18, pp. 3546–3548, 2015.

61. F. Schmidt, L. Ledermann, A. Schäffer, H. J. Snaith, and M. Lenz, "Rapid sequestration of perovskite solar cell-derived lead in soil," *Journal of Hazardous Materials*, vol. 436, p. 128995, 2022.

62. M. Bomgardner, "How First Solar recycles its CdTe panels," *C&EN Global Enterp*, vol. 96, no. 15, pp. 40–40, 2018.

63. F.-W. Liu, G. Biesold, M. Zhang, R. Lawless, J.-P. Correa-Baena, Y.-L. Chueh, and Z. Lin, "Recycling and recovery of perovskite solar cells," *Materials Today*, vol. 43, pp. 185–197, 2021.

64. Z.-K. Tan, R. S. Moghaddam, M. L. Lai, P. Docampo, R. Higler, F. Deschler, M. Price, A. Sadhanala, L. M. Pazos, D. Credgington, F. Hanusch, T. Bein, H. J. Snaith, and R. H. Friend, "Bright light-emitting diodes based on organometal halide perovskite," *Nature Nanotech*, vol. 9, no. 9, pp. 687–692, 2014.

65. T.-H. Han, K. Y. Jang, Y. Dong, R. H. Friend, E. H. Sargent, and T.-W. Lee, "A roadmap for the commercialization of perovskite light emitters," *Nat Rev Mater*, vol. 7, no. 10, pp. 757–777, 2022.

66. M. R. Filip, G. Volonakis, and F. Giustino, "Hybrid Halide Perovskites: Fundamental Theory and Materials Design," in *Handbook of Materials Modeling: Applications: Current and Emerging Materials* (W. Andreoni and S. Yip, eds.), pp. 295–324, Cham: Springer International Publishing, 2020.

CHAPTER 2

Background on 2 eV Solar Cells

In the race to increase renewable energy capacity and limit global warming to 1.5 °C,[1] photovoltaics play a key role.[2] Perovskite solar cells (PSCs) possess complimentary properties to existing silicon solar technology – such as high absorption coefficients, bandgap tunability, and low-temperature vapour processing – offering the prospect of increased power output per area through multijunction technology at an affordable cost. Large steps have already been made towards this with tandem devices (where there are two junctions) of silicon bottom cells and perovskite top cells (Si–perovskite tandems), with multiple groups exceeding the record efficiency of single-junction Si cells[3] and the current certified world record standing at 33.9 % power conversion efficiency (PCE).[4] Also all-perovskite tandems are showing potential, with certified efficiencies now surpassing 28 %.[5]

In comparison, triple-junction technologies are still immature and undeveloped. Eight publications have reported triple-junction solar cells with PSCs to date, with the only certified efficiency reported to date only at 23.29 %,[6–13], far below the detailed balance limit of 49 % for a generic triple-junction[14] and the best reported perovskite

tandem cells. Half of these eight publications are from within the last 12 months, indicating that interest in the topic is picking up. The increase in number of junctions in a multijunction solar cell comes with the advantage of improved spectral utilization – and thus efficiency – but with the disadvantage of increased manufacturing complexity and cost. The improved spectral utilization also comes with diminishing returns for each added junction, putting a practical limitation on the number of junctions worth investigating with a commercial mindset. More than four or five junctions are considered unrealistic for practically all applications.[15]

2.1 Perovskite Triple-junction Solar Cells

Werner et al.[6] reported the first example of a Si–perovskite–perovskite triple-junction in 2018. The device was made on double-side textured Si wafers using a sequential deposition method for the perovskite absorbers by coevaporation of a template layer of inorganic salts and subsequently spincoating a solution with the organic salt. In 2019, McMeekin et al.[7] demonstrated the first all-perovskite triple-junction device. In this device, all perovskite layers were solution processed. The 20 % PCE barrier was broken in 2020 by Xiao et al.,[8] this was a solution-processed all-perovskite triple-junction with a champion PCE of 20.1 %. Another all-perovskite device was reported in the same year by J. Wang et al. using a two-step solution process.[10] In 2022, the record for Si–perovskite–perovskite was brought to 20.1 % PCE by Zheng et al.[9] and an organic–perovskite–perovskite with a PCE of 19.4 % and record V_{OC} of 3.03 V was reported by Isikgor et al.[13] Recently, records were broken again when Z. Wang et al.[11] brought the all-perovskite triple-junction record to a certified efficiency of 23.29 % by employing an all-inorganic top cell with a bandgap of 2.0 eV but with a relatively low bromide content of 42 % by substituting 15 % of the Cs with Rb. The Si–perovskite–perovskite record was also increased to 22.38 % by Y. J. Choi et al.[12] who used a volatile solvent system for the top cell to eliminate the need for additional protection layers between the top and the middle cell.

In 2017 Hörantner et al.[16] calculated that efficiencies of 33.1 % for all-perovskite (with 1.22 eV bottom cell) and 35.3 % for Si–perovskite–perovskite triple junctions could realistically be achieved with the state-of-the-art absorber, transport and recombination layers at the time, and that future improvements could take these numbers to 36.6 % and 38.8 %, respectively. To reach the peak efficiencies in these calculations, the bandgap of the top cell perovskite absorber needs to be 2.05 and 1.95 eV, respectively. (Figure 2.1.) Furthermore, the peak efficiency calculated for Si–perovskite–perovskite with 1.95 eV top cell requires a 1.44 eV middle cell – only achievable with PbSn – while if the middle cell is restricted to 1.50 eV, which can be achieved without Sn, the requirement on the top cell bandgap becomes 2.0 eV (at 34.6 % PCE). It is clear that if the true potential of triple-junction PSCs is to be realized, efficient and stable top cells with bandgap close to 2.0 eV will be required. Henceforth, we will be referring to devices and materials with bandgap close to 2.0 eV as "2 eV" materials or devices.

2.2 2 eV Perovskite Absorbers and Solar Cells

Similar to the limited amount of reported work on triple-junction devices with perovskites, relatively little work has been published on the development of the stable and efficient 2 eV materials and devices. However, the development of this category of perovskite materials and the understanding of the specific challenges involved is key to achieving high-quality triple-junction devices. While many publications on triple-junction devices report some minor optimization of materials and cells in the 1.90 to 2.10 eV bandgap range[7,9,13] or perform basic characterization of said materials as part of a study of a wider range of bandgaps,[17–19] only four publications to date report thorough investigations into development and understanding of 2 eV absorbers for solar cells.

K. Choi et al.[20] developed a post-hot processing (PHP) protocol for use with a $FAPb(Br_xI_{1-x})_3$ absorber, focusing particularly on an absorber with a Br percentage of 73 %. (Henceforth we will refer to absorbers with formamidinium as the only cation

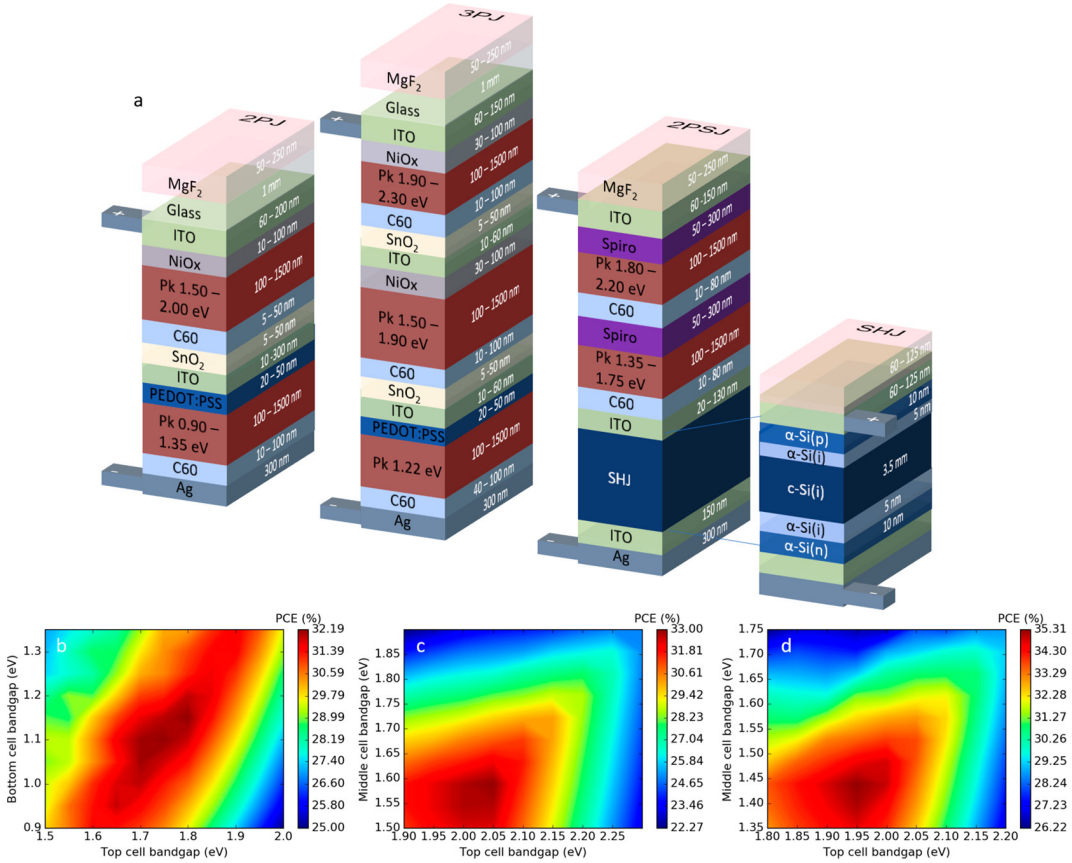

Figure 2.1: (a) Illustration of the perovskite tandem junction, all-perovskite triple-junction, and perovskite-on-silicon triple-junction device architectures. The thickness range used in the optical model for each layer is written upon the illustration. (b) All-perovskite double-junction PCE for varied band gap combinations of bottom and top absorber. (c) All-perovskite triple-junction solar cell PCE for varied band gap combinations of bottom and top absorber on top of perovskite base absorber with fixed 1.22 eV band gap. (d) Perovskite–perovskite–silicon triple-junction solar cell PCE for varied band gap combinations of bottom and top perovskite absorber on top of fixed band gap SHJ base absorber. Reproduced with permission from [16].

as "neat FA" absorbers. We will also class their absorber as neat FA, even if they state the use of MACl as a processing agent.) In their protocol, the perovskite is spin-coated from a DMF:DMSO solution with a diethyl ether antisolvent quenching step, the film is then annealed at atmospheric pressure before it is subjected to a PHP step at 80 MPa at elevated temperature. They found that at temperatures $\geq$ 150 °C the PHP treatment resulted in in-plane grain growth and a reduction of surface roughness. They report a reduction in the severity of halide segregation and improved photostability of their 2.00 eV device, which they attribute to the reduction in grain boundary area and the reduction of grain boundary defects such as iodide vacancies. The best PCE of devices made with their PHP method was 11.86 % with a V_{OC} of 1.35 V.

This year, Cheng et al.[21] reported an absorber with target composition $FA_{0.8}Cs_{0.2}Pb(Br_{0.7}I_{0.3})_3$ fabricated through a green solvent method using a spin-coated template layer of lead and caesium acetate from an acetic acid solution followed by two rounds of spin-coating of organic precursors (FABr, MABr and MAI) from an isopropanol solution. The 2.0 eV shows higher photostability than a reference film with the same composition fabricated with DMF:DMSO and the antisolvent quenching route, and the device performance is better. They attribute this to acetate anions mitigating defects such as halide vacancies. The green solvent also exhibits less tendency to dissolve underlying perovskite films in a multijunction configuration. Their champion device exhibited a PCE of 10.62 % and a V_{OC} of 1.325 V.

Also Y. J. Choi et al.[12] developed a 2 eV perovskite fabricated with a solvent system designed not to cause damage to the underlying cells in a multijunction configuration. They used the volatile system of acetonitrile–methylamine in ethanol developed and employed in lower bandgap absorbers by Noel et al.[7,22] Employing a $MAPb(I_{0.5}Br_{0.35}Cl_{0.15})_3$ composition with a bandgap of 1.96 eV and using a urea additive, they obtained well-performing top cells with a champion efficiency of 13.88 % PCE and 1.28 V V_{OC}, as well as the aforementioned record Si–perovskite–perovskite triple junction record.

Wang et al.[11] took the approach of developing an inorganic top cell. They incorporated Rb^+ to increase the bandgap at lower Br^- content and to introduce lattice distortion. They found Rb^+ could be incorporated into the lattice at concentrations depending on the Br^- concentration. They report reduced halide segregation, mobile ion concentrations and electronic disorder in their $Cs_{0.85}Rb_{0.15}PbBr_{1.25}I_{1.75}$ absorber and their single-junction devices exhibited a PCE of 13.41 % and a V_{OC} of 1.312 V. As mentioned, their triple-junctions with this absorber are the record to date across all perovskite-containing triple-junction devices.

2.3 Halide Segregation

A general trait of 2 eV bulk halide perovskite materials is that the tuning of the bandgap requires a mixed halide composition with a rather large bromide content. However, perovskite with iodide–bromide mixtures tend to be subjected to the phenomenon of halide segregation.[23] There is wide consensus that with the presence of excited charge carriers, either through photogeneration or charge injection, these materials suffer the formation of small iodide-rich domains with a lower bandgap than the parent "mixed phase".[23–26] This is most evident in time-dependent PL or EL spectra, where a peak at longer wavelength develops over time under illumination or injection.[23,27] The longer-wavelength ("segregated") peak tends to grow much brighter than the mixed phase due to charge funnelling from the surrounding high-bandgap phase to the low-bandgap domains.[28] The iodide-rich domains can be nanoscale-sized clusters that make up a much smaller fraction of the absorber material than their relative luminescence intensity would suggest.[28] An important characteristic of the halide segregation phenomenon is that it is reversible under the absence of an excitation source through entropic mixing of the halides.[23,29,30] During illumination of a completely unsegregated absorber, the segregated PL peak has typically been observed to arise at a wavelength between the PL of the mixed phase and that of a 100 % iodide absorber, and then gradually red-shift towards a terminal wavelength that is often found to

correspond to approximately 80 % iodide.[23] In some studies on neat-MA absorbers, this has been found to be preceded by a flash formation of a quite red-shifted PL, which then quickly blue-shifts in the course of the first 5 to 15 s before the aforementioned red-shift to terminal position begins.[31,32] This has been attributed to formation of tiny iodide-rich clusters which then blue-shifts due to kinetic trapping of bromide during the fast initial growth.[25,31,32] Another important aspect of the halide segregation is that it has been observed to be intensity-dependent and to have a threshold intensity with temperature dependence.[33,34] The phenomenon has also been observed with chloride.[24]

Several approaches exist to mitigate halide segregation in halide perovskites. Among them are: alloying of the A and/or B cation sites in the ABX_3 structure; alloying of the anion (X) site with Cl^- as a third anion; improved crystallinity and increased grain size; passivation of bulk and interface trap states; reduction of halide vacancy concentration by stoichiometric excess of halides; temperature control; and application of compressive strain.[24]

Multiple theories have also been proposed for the driving force for halide segregation, including polaron-induced strain gradients, local electric fields caused by electron-hole pairs, gradients in carrier generation, and free energy reduction due to the bandgap difference.[29,33,35–38] Perhaps the most mature theory to date is the "unified theory" by Chen et al.[25] They consider the compositional Helmholtz free energy of 5 perovskite compounds with varying bromide concentration using binary alloying theory and combine this with a term describing the free energy of the distribution of photogenerated carriers, the combined sum is then minimized to establish the phase diagrams. They find that upon illumination, large metastable regions appear in the phase diagram. The area of the metastable regions in the phase diagram depends strongly on the illumination intensity, and the binodals (coexistence curves) that separate the stable and metastable regions depend strongly on temperature, thus explaining the threshold intensity and the temperature dependence of the threshold intensity. The driving force for the halide segregation is the bandgap difference between

the mixed and segregated phases, allowing the photogenerated carriers to lower their free energy by funnelling to iodide-rich phases. This energetically incentivizes the nucleation and growth of the iodide-rich phase. Small iodide-rich clusters that can become nuclei are expected to arise due to stochastic fluctuations. They suggest the main reason for the improved stability of mixed FA–Cs alloys is that the unit cell volume is reduced and therefore also the bandgap difference between the mixed and segregated phase. The theory does not take any surface free energy between the phases or kinetics into account.

Because reversible halide segregation is not a long-term degradation effect, its main consequence is its immediate effect on the working performance of a solar cell from day zero of that solar cell's life. Given the nature of the halide segregation, the effect on performance can be expected to manifest within a certain timespan from the beginning of each illumination cycle, where the onset timespan can vary between just a few seconds to hours, depending on the quality of the perovskite material. For a long time, halide segregation was thought to be the culprit of a "V_{OC} pinning" of wide-gap perovskite solar cells, where – despite increasing absorber bandgap – V_{OC} would rarely exceed approximately 1.2 V. This was known as the "Hoke effect" or "Hoke limit".[26] In 2019, Mahesh et al.[39] estimated that the upperbound for V_{OC} loss due to halide segregation for a 1.94 eV cell was 220 mV, and 97 mV for a 1.77 eV cell, because of increased subgap absorption causing increased radiative dark current. However, the actual V_{OC} loss was lower in both cases, which they attribute to the improved radiative efficiency of the segregated minority phase. In comparison, they found that approximately 400 mV of the total V_{OC} loss was due to nonradiative recombination in the bulk or interface. Peña-Camargo et al. later found that nonradiative losses at the interfaces became an increasingly dominant source of V_{OC} losses for higher bromide content.[40] The wider the bandgap of the mixed-halide perovskite, the higher are thus both the possible V_{OC} loss and the interface loss, with today's state of the art materials.

2.4 Theory

2.4.1 Quasi-Fermi Level Splitting

2.4.1.1 Quasi-Fermi Levels

The electron distribution across the density of states in a semiconductor is described by the Fermi distribution:

$$f(E) = \frac{1}{\exp\left\{(E - E_{\mathrm{F}})/k_{\mathrm{B}}T\right\}}, \tag{2.1}$$

where E_{F} is the Fermi level, which indicates the energy level at which there is a 50 percent probability that the state is occupied. For an intrinsic semiconductor in the dark, this would be in the centre of the bandgap. The density of electrons in the conduction band can then be described as

$$n_{\mathrm{e}} = N_{\mathrm{C}} \exp\Big\{ - \frac{E_{\mathrm{C}} - E_{\mathrm{F}}}{k_{\mathrm{B}}T}\Big\}, \tag{2.2}$$

and for holes in the valence band as

$$n_{\mathrm{h}} = N_{\mathrm{V}} \exp\Big\{ - \frac{E_{\mathrm{F}} - E_{\mathrm{V}}}{k_{\mathrm{B}}T}\Big\}, \tag{2.3}$$

where N_{C} and N_{V} are the effective densities of states of the conduction and valence band, respectively, E_{C} is the conduction band edge and E_{V} is the valence band edge. This gives the relation:

$$n_{\mathrm{e}} n_{\mathrm{h}} = N_{\mathrm{C}} N_{\mathrm{V}} \exp\Big\{ - \frac{E_{\mathrm{C}} - E_{\mathrm{V}}}{k_{\mathrm{B}}T}\Big\} = N_{\mathrm{C}} N_{\mathrm{V}} \exp\Big\{ - \frac{E_{\mathrm{G}}}{k_{\mathrm{B}}T}\Big\} =: n_i^2, \tag{2.4}$$

where E_{G} is the bandgap.

Under irradiation, the electron density in the conduction band and hole density in the valence band both increase, thus the characteristic energy describing their Fermi distributions, the Fermi level, must be closer to the conduction band for the electrons in the conduction band and closer to the valence band for the electrons in the valence band.[41] We can therefore describe electrons in the conduction band with a Fermi distribution

$$f_{\mathrm{e,C}}(E) = \frac{1}{\exp\left\{(E - E_{\mathrm{F,C}})/k_{\mathrm{B}}T\right\}}, \tag{2.5}$$

and electrons in the valence band with a Fermi distribution

$$f_{\mathrm{e,V}}(E) = \frac{1}{\exp\left\{(E - E_{\mathrm{F,V}})/k_{\mathrm{B}}T\right\}}, \tag{2.6}$$

where $E_{\mathrm{F,C}}$ is the quasi-Fermi level of the electrons or holes in the conduction band and $E_{\mathrm{F,V}}$ is the quasi-Fermi level of the electrons or holes in the valence band, which replace E_{F} as the characteristic energy describing their distribution. The distribution of holes is given by $f_{\mathrm{h,C}}(E) = 1 - f_{\mathrm{e,C}}(E)$ and $f_{\mathrm{h,V}}(E) = 1 - f_{\mathrm{e,V}}(E)$ for the conduction and valence band, respectively. See also Figure 2.2. Consequently, the product $n_{\mathrm{e}}n_{\mathrm{h}}$ becomes:

$$\begin{aligned} n_{\mathrm{e}}n_{\mathrm{h}} &= N_{\mathrm{C}}N_{\mathrm{V}} \exp\Big\{-\frac{E_{\mathrm{C}} - E_{\mathrm{F,C}}}{k_{\mathrm{B}}T}\Big\} \exp\Big\{-\frac{E_{\mathrm{F,V}} - E_{\mathrm{V}}}{k_{\mathrm{B}}T}\Big\} \\ &= N_{\mathrm{C}}N_{\mathrm{V}} \exp\Big\{-\frac{E_{\mathrm{C}} - E_{\mathrm{V}}}{k_{\mathrm{B}}T}\Big\} \exp\Big\{\frac{E_{\mathrm{F,C}} - E_{\mathrm{F,V}}}{k_{\mathrm{B}}T}\Big\} \\ &= n_i^2 \exp\Big\{\frac{E_{\mathrm{F,C}} - E_{\mathrm{F,V}}}{k_{\mathrm{B}}T}\Big\} =: n^2. \end{aligned} \tag{2.7}$$

In this equation, $E_{\mathrm{F,C}} - E_{\mathrm{F,V}}$ is known as the quasi-Fermi level splitting ($QFLS$).

It can be shown[41] that the electrochemical potential of the carrier species, η_i, relates to the quasi-Fermi levels through

$$\eta_{\mathrm{e}} = E_{\mathrm{F,C}}, \tag{2.8}$$

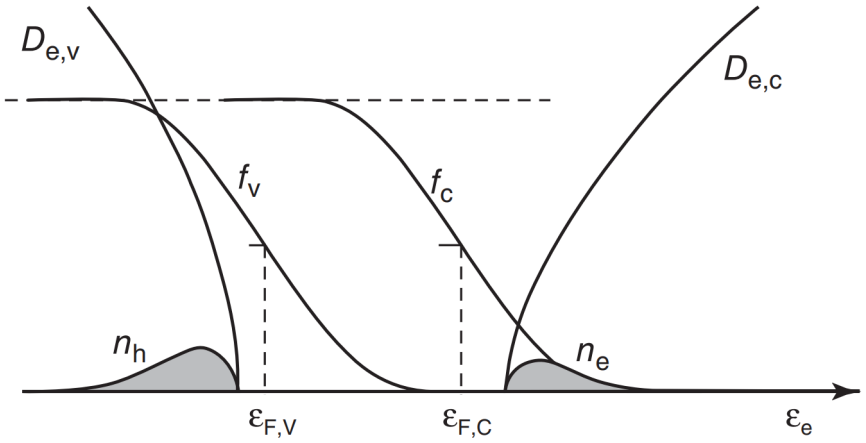

Figure 2.2: In an illuminated semiconductor, the occupations of the conduction band and the valence band are described by different Fermi distributions $f_{\mathrm{e,C}}(E)$ (f_{C}) and $f_{\mathrm{e,V}}(E)$ (f_{V}). Reproduced with permission from[41].

and

$$\eta_{\mathrm{h}} = -E_{\mathrm{F,V}}, \tag{2.9}$$

and thus that the electrochemical potential for an electron–hole pair is

$$\eta_{\mathrm{e}} + \eta_{\mathrm{h}} = (\mu_{\mathrm{e}} + z_{\mathrm{e}}e\varphi) + (\mu_{\mathrm{h}} + z_{\mathrm{h}}e\varphi) = \mu_{\mathrm{e}} + \mu_{\mathrm{h}} = E_{\mathrm{F,C}} - E_{\mathrm{F,V}} = QFLS, \tag{2.10}$$

where the electrostatic potential term cancels because of the opposite signs of z_{e} and z_{h} (the charge polarities). (φ is the electrostatic potential.)

The quasi-Fermi level splitting, or the (electro)chemical potential of the electron–hole pair, $\mu_{\mathrm{eh}} = \mu_{\mathrm{e}} + \mu_{\mathrm{h}}$, largely defines how much radiation energy a solar cell can convert into electrical energy and represents the upper boundary for the measurable potential difference (V) between the electrodes of the solar cell.

2.4.1.2 Probing the QFLS

The photoluminescence quantum yield of a semiconducting material is the ratio of emitted photon flux, ϕ_{emitted}, to absorbed photon flux, ϕ_{absorbed} (Equation (2.11) (i)). Considering this in the perspective of a species of excited charge carrier in the material, we can rewrite to Equation (2.11) (ii), where $J_{\mathrm{R,rad}}$ is the radiative recombination

current density of the species and J_{G} is the generation current density of excited carriers of the species.

$$PLQY \overset{\text{i}}{=} \frac{\phi_{\text{emitted}}}{\phi_{\text{absorbed}}} \overset{\text{ii}}{=} \frac{J_{\mathrm{R,rad}}}{J_{\mathrm{G}}}. \tag{2.11}$$

Further, we recall from Equation (2.7) that the carrier densities under irradiation, n^2, is related to the intrinsic carrier densities, n_i^2 and the $QFLS$. Solving Equation (2.7) for $QFLS$ and making use of the relations $J_{\mathrm{R,rad}} = edkn^2$ and $J_{0,\mathrm{rad}} = edkn_i^2$, where $J_{0,\mathrm{rad}}$ is the dark radiative recombination current, e is the elementary charge, d is the thickness of the material and k is the recombination constant, and the relation $J_{\mathrm{R,rad}} = PLQY \cdot J_{\mathrm{G}}$ from Equation (2.11), we get

$$\begin{aligned} QFLS &= k_{\mathrm{B}}T \ln\left\{\frac{n^2}{n_i^2}\right\} \\ &= k_{\mathrm{B}}T \ln\left\{\frac{J_{\mathrm{R,rad}}}{J_{0,\mathrm{rad}}}\right\} \\ &= k_{\mathrm{B}}T \ln\left\{PLQY \frac{J_{\mathrm{G}}}{J_{0,\mathrm{rad}}}\right\} \\ &= k_{\mathrm{B}}T \ln\left\{PLQY\right\} + k_{\mathrm{B}}T \ln\left\{\frac{J_{\mathrm{G}}}{J_{0,\mathrm{rad}}}\right\}. \end{aligned} \tag{2.12}$$

In the radiative limit, where $PLQY = 100\% = 1$, we get that $QFLS = k_{\mathrm{B}}T \ln\{J_{\mathrm{G}}/J_{0,\mathrm{rad}}\} =: QFLS_{\mathrm{rad}}$, where we define the quantity $QFLS_{\mathrm{rad}}$ as the $QFLS$ in the radiative limit, and we end up with Equation (2.13):

$$QFLS = QFLS_{\mathrm{rad}} + k_{\mathrm{B}}T \ln\left\{PLQY\right\} \tag{2.13}$$

We now need to be able to quantify $QFLS_{\mathrm{rad}}$ by estimating J_{G} and $J_{0,\mathrm{rad}}$. Under the assumption that all excited carriers are extracted at the contacts at short-circuit conditions, we can approximate $J_{\mathrm{G}} \approx J_{\mathrm{SC}}$, and determine J_{G} through

$$J_{\mathrm{G}} \approx J_{\mathrm{SC}} = q \int EQE_{\mathrm{PV}}(E)\phi_{\mathrm{AM1.5}}(E)dE. \tag{2.14}$$

Based on the principles of optical reciprocity by Rau,[42] which we discuss below, we can calculate $J_{0,\mathrm{rad}}$ in a similar manner:

$$J_{0,\mathrm{rad}} = q \int EQE_{\mathrm{PV}}(E)\phi_{\mathrm{BB}}(E)dE, \tag{2.15}$$

2.4.2 Reciprocity

2.4.2.1 Rau's First Reciprocity Theorem

The reciprocity theorems by Rau[42] provide an important framework that connects characteristics of the two different operation modes of the optoelectronic devices we employ as solar cells: the photovoltaic (solar cell) mode and the light-emitting (LED) mode.

The principle behind Rau's reciprocity theorems is that a solar cell cannot distinguish between current generated by the sun and the current generated by the ambient (blackbody) spectrum. A solar cell in thermal equilibrium with its surroundings at a temperature T, must have a net zero current flowing through the device. Since we know there will be an incident radiation from the ambient, $\phi_{\mathrm{eq}} = \cos\theta\phi_{\mathrm{BB}}$, that will give rise to excited carriers that can be collected as a current at the electrodes, $J_{0,\mathrm{SC}}$, we can reason that there will be an equivalent injection current in the opposite direction, $J_{0,\mathrm{inj}}$ leading to radiative emission, $\phi_{0,\mathrm{EL}}$.

Rau further postulates that any excess emission, ϕ_{EL}, stemming from an applied bias follows the diode law, and finally he arrives at the integral form of his first reciprocity theorem:

$$\Phi_{\mathrm{EL}}(E_\gamma) = \int_\Omega \int_{\mathrm{S}} Q(\boldsymbol{r}_{\mathrm{S}}, \theta, \varphi, E_\gamma)\phi_{\mathrm{eq}}(E_\gamma, \theta)d\Omega dS \cdot \left[\exp\left\{\frac{qV}{k_{\mathrm{B}}T}\right\} - 1\right], \tag{2.16}$$

where $Q(\boldsymbol{r}_{\mathrm{S}}, \theta, \varphi, E_\gamma)$ is the probability of an incident photon leading to a carrier being collected at the electrodes. In the case that the incident radiation is normal to

the surface, as is normally the case in a laboratory test environment for solar cells, we can rewrite as follows

$$\phi_{\mathrm{EL}}(E_\gamma) = EQE_{\mathrm{PV}}(E_\gamma)\phi_{\mathrm{BB}}(E_\gamma)\Big[\exp\Big\{\frac{qV}{k_{\mathrm{B}}T}\Big\} - 1\Big]. \tag{2.17}$$

2.4.2.2 Rau's Second Reciprocity Theorem

In the same article, Rau goes on to show that $V_{\mathrm{OC,rad}}$ can be calculated analogously to what we showed for $QFLS_{\mathrm{rad}}$ in Section 2.4.1, with the equation:

$$V_{OC,\mathrm{rad}} = \frac{k_{\mathrm{B}}T}{q}\ln\Big\{\frac{J_{\mathrm{SC}}}{J_{0,\mathrm{rad}}}\Big\}, \tag{2.18}$$

and that the V_{OC} in a nonradiative context can be related to the LED performance indicator, EQE_{EL}, through

$$V_{OC} = V_{OC,\mathrm{rad}} + \frac{k_{\mathrm{B}}T}{q}\ln\Big\{EQE_{\mathrm{EL}}\Big\}. \tag{2.19}$$

This is Rau's second reciprocity theorem.

2.4.2.3 Würfel's Generalization of Kirchoff's Law

In addition to the reciprocity theorems by Rau, we should take note of Würfel's Generalization of Kirchoff's Law[41,43] which he derives after introducing the concept of a chemical potential for a photon. Würfel derives the relation

$$J_\gamma = a(E_\gamma)\frac{E_\gamma^2}{4\pi^2\hbar^3c^2}\Big[\exp\Big\{\frac{E_\gamma - (\mu_{\mathrm{C}} - \mu_{\mathrm{V}})}{k_{\mathrm{B}}T}\Big\} - 1\Big]^{-1}, \tag{2.20}$$

where J_γ is the emitted photon current, E_γ is the photon energy and $\mu_\gamma = \mu_{\mathrm{C}} - \mu_{\mathrm{V}}$ is the chemical potential of the photon described by the chemical potential of electrons in the conduction and valence bands, respectively.

This can be rephrased to give us an expression for the photoluminescent flux in terms of the blackbody radiation of the ambient and the $QFLS$:

$$\begin{aligned}\phi_{PL}(E_\gamma) &= C \cdot a(E_\gamma)\phi_{\mathrm{BB}}(E_\gamma) \cdot \left[\exp\left\{\frac{E_\gamma}{k_\mathrm{B}T}\right\} - 1\right]\left[\exp\left\{\frac{E_\gamma - (\mu_\mathrm{C} - \mu_\mathrm{V})}{k_\mathrm{B}T}\right\} - 1\right]^{-1} \\ &\overset{*}{\approx} C \cdot a(E_\gamma)\phi_{\mathrm{BB}}(E_\gamma) \cdot \exp\left\{\frac{E_\gamma}{k_\mathrm{B}T}\right\}\exp\left\{\frac{E_\gamma - (\mu_\mathrm{C} - \mu_\mathrm{V})}{k_\mathrm{B}T}\right\}^{-1} \\ &= C \cdot a(E_\gamma)\phi_{\mathrm{BB}}(E_\gamma) \cdot \exp\left\{\frac{E_\gamma - E_\gamma + (\mu_\mathrm{C} - \mu_\mathrm{V})}{k_\mathrm{B}T}\right\} \\ &= C \cdot a(E_\gamma)\phi_{\mathrm{BB}}(E_\gamma) \cdot \exp\left\{\frac{QFLS}{k_\mathrm{B}T}\right\},\end{aligned} \tag{2.21}$$

where the approximation (*) comes from $\exp(...) \gg 1$ which for $E_\gamma > E_\mathrm{G}$ is mostly quite accurate at ambient temperatures ($k_\mathrm{B}T$ small), and where C is an arbitrary constant. Equation (2.21) is nearly identical to Equation (2.17), where EQE_PV sits in the place of the absorptance, $a(E_\gamma)$, and qV sits in the place of the $QFLS$.

References

1. United Nations Framework Convention on Climate Change, "Paris Agreement." https://www.un.org/en/climatechange/paris-agreement, 2016. Accessed: 2023-06-27.
2. Intergovernmental Panel on Climate Change, "IPCC, 2022: Summary for Policymakers (Figure SPM.7)," in *Climate Change 2022: Mitigation of Climate Change. Contribution of Working Group III to the Sixth Assessment Report of the Intergovernmental Panel on Climate Change* (P. Shukla, J. Skea, R. Slade, A. Al Khourdajie, R. van Diemen, D. McCollum, M. Pathak, S. Some, P. Vyas, R. Fradera, M. Belkacemi, A. Hasija, G. Lisboa, S. Luz, and J. Malley, eds.), p. 38, Cambridge, UK and New York, NY, USA: Cambridge University Press, 2022.
3. National Renewable Energy Laboratory, "Best research-cell efficiency chart," 2023. Accessed: 2023-06-26.
4. LONGi, "LONGi sets a new world record of 33.9% for the efficiency of crystalline silicon-perovskite tandem solar cells." https://www.longi.com/en/news/new-world-record-for-the-efficiency-of-crystalline-silicon-perovskite-tandem-solar-cells//, 2023. Accessed: 2023-12-02.
5. R. Lin, Y. Wang, Q. Lu, B. Tang, J. Li, H. Gao, Y. Gao, H. Li, C. Ding, J. Wen, P. Wu, C. Liu, S. Zhao, K. Xiao, Z. Liu, C. Ma, Y. Deng, L. Li, F. Fan, and H. Tan, "All-perovskite tandem solar cells with 3D/3D bilayer perovskite heterojunction," *Nature*, pp. 1–3, 2023.
6. J. Werner, F. Sahli, F. Fu, J. J. Diaz Leon, A. Walter, B. A. Kamino, B. Niesen, S. Nicolay, Q. Jeangros, and C. Ballif, "Perovskite/Perovskite/Silicon Monolithic Triple-Junction Solar Cells with a Fully Textured Design," *ACS Energy Lett.*, vol. 3, no. 9, pp. 2052–2058, 2018.
7. D. P. McMeekin, S. Mahesh, N. K. Noel, M. T. Klug, J. Lim, J. H. Warby, J. M. Ball, L. M. Herz, M. B. Johnston, and H. J. Snaith, "Solution-Processed All-Perovskite Multi-junction Solar Cells," *Joule*, vol. 3, no. 2, pp. 387–401, 2019.
8. K. Xiao, J. Wen, Q. Han, R. Lin, Y. Gao, S. Gu, Y. Zang, Y. Nie, J. Zhu, J. Xu, and H. Tan, "Solution-Processed Monolithic All-Perovskite Triple-Junction Solar Cells with Efficiency Exceeding 20%," *ACS Energy Lett.*, vol. 5, no. 9, pp. 2819–2826, 2020.
9. J. Zheng, G. Wang, W. Duan, M. A. Mahmud, H. Yi, C. Xu, A. Lambertz, S. Bremner, K. Ding, S. Huang, and A. W. Y. Ho-Baillie, "Monolithic Perovskite–Perovskite–Silicon Triple-Junction Tandem Solar Cell with an Efficiency of over 20%," *ACS Energy Lett.*, vol. 7, no. 9, pp. 3003–3005, 2022.
10. J. Wang, V. Zardetto, K. Datta, D. Zhang, M. M. Wienk, and R. A. J. Janssen, "16.8%

Monolithic all-perovskite triple-junction solar cells via a universal two-step solution process," *Nat Commun*, vol. 11, no. 1, p. 5254, 2020.

11. Z. Wang, L. Zeng, T. Zhu, H. Chen, B. Chen, D. J. Kubicki, A. Balvanz, C. Li, A. Maxwell, E. Ugur, R. dos Reis, M. Cheng, G. Yang, B. Subedi, D. Luo, J. Hu, J. Wang, S. Teale, S. Mahesh, S. Wang, S. Hu, E. D. Jung, M. Wei, S. M. Park, L. Grater, E. Aydin, Z. Song, N. J. Podraza, Z.-H. Lu, J. Huang, V. P. Dravid, S. De Wolf, Y. Yan, M. Grätzel, M. G. Kanatzidis, and E. H. Sargent, "Suppressed phase segregation for triple-junction perovskite solar cells," *Nature*, vol. 618, no. 7963, pp. 74–79, 2023.

12. Y. J. Choi, S. Y. Lim, J. H. Park, S. G. Ji, and J. Y. Kim, "Atomic Layer Deposition-Free Monolithic Perovskite/Perovskite/Silicon Triple-Junction Solar Cells," *ACS Energy Lett.*, pp. 3141–3146, 2023.

13. F. H. Isikgor, T. Maksudov, X. Chang, B. Adilbekova, Z. Ling, W. T. Hadmojo, Y. Lin, and T. D. Anthopoulos, "Monolithic Perovskite–Perovskite–Organic Triple-Junction Solar Cells with a Voltage Output Exceeding 3 V," *ACS Energy Lett.*, vol. 7, no. 12, pp. 4469–4471, 2022.

14. A. D. Vos, "Detailed balance limit of the efficiency of tandem solar cells," *J. Phys. D: Appl. Phys.*, vol. 13, no. 5, p. 839, 1980.

15. I. M. Peters, C. D. Rodríguez Gallegos, L. Lüer, J. A. Hauch, and C. J. Brabec, "Practical limits of multijunction solar cells," *Progress in Photovoltaics: Research and Applications*, vol. 31, no. 10, pp. 1006–1015, 2023.

16. M. T. Hörantner, T. Leijtens, M. E. Ziffer, G. E. Eperon, M. G. Christoforo, M. D. McGehee, and H. J. Snaith, "The Potential of Multijunction Perovskite Solar Cells," *ACS Energy Lett.*, vol. 2, no. 10, pp. 2506–2513, 2017.

17. B. Slimi, M. Mollar, I. Ben Assaker, A. Kriaa, R. Chtourou, and B. Marí, "Synthesis and characterization of perovskite FAPbBr3-x I x thin films for solar cells," *Monatsh Chem*, vol. 148, no. 5, pp. 835–844, 2017.

18. D. Forgács, D. Pérez-del Rey, J. Ávila, C. Momblona, L. Gil-Escrig, B. Dänekamp, M. Sessolo, and H. J. Bolink, "Efficient wide band gap double cation – double halide perovskite solar cells," *J. Mater. Chem. A*, vol. 5, no. 7, pp. 3203–3207, 2017.

19. M. Suri, A. Hazarika, B. W. Larson, Q. Zhao, M. Vallés-Pelarda, T. D. Siegler, M. K. Abney, A. J. Ferguson, B. A. Korgel, and J. M. Luther, "Enhanced Open-Circuit Voltage of Wide-Bandgap Perovskite Photovoltaics by Using Alloyed (FA1–xCsx)Pb(I1–xBrx)3 Quantum Dots," *ACS Energy Lett.*, vol. 4, no. 8, pp. 1954–1960, 2019.

20. K. Choi, M. J. Jeong, S. Lee, G. Alosaimi, J. Seidel, J. S. Yun, and J. H. Noh, "Suppressing Halide Segregation in Wide-Band-Gap Mixed-Halide Perovskite Layers through Post-Hot Pressing," *ACS Appl. Mater. Interfaces*, vol. 14, no. 21, pp. 24341–24350, 2022.

21. J. Cheng, I. Choi, W. Kim, H. Li, B. Koo, and M. J. Ko, "Wide-Band-Gap (2.0 eV) Perovskite Solar Cells with a VOC of 1.325 V Fabricated by a Green-Solvent Strategy," *ACS Appl. Mater. Interfaces*, vol. 15, no. 19, pp. 23077–23084, 2023.

22. N. K. Noel, S. N. Habisreutinger, B. Wenger, M. T. Klug, M. T. Hörantner, M. B. Johnston, R. J. Nicholas, D. T. Moore, and H. J. Snaith, "A low viscosity, low boiling point, clean solvent system for the rapid crystallisation of highly specular perovskite films," *Energy Environ. Sci.*, vol. 10, no. 1, pp. 145–152, 2017.

23. E. T. Hoke, D. J. Slotcavage, E. R. Dohner, A. R. Bowring, H. I. Karunadasa, and M. D. McGehee, "Reversible photo-induced trap formation in mixed-halide hybrid perovskites for photovoltaics," *Chem. Sci.*, vol. 6, no. 1, pp. 613–617, 2015.

24. A. J. Knight and L. M. Herz, "Preventing phase segregation in mixed-halide perovskites: a perspective," *Energy Environ. Sci.*, vol. 13, no. 7, pp. 2024–2046, 2020.

25. Z. Chen, G. Brocks, S. Tao, and P. A. Bobbert, "Unified theory for light-induced halide segregation in mixed halide perovskites," *Nat Commun*, vol. 12, no. 1, p. 2687, 2021.

26. E. L. Unger, L. Kegelmann, K. Suchan, D. Sörell, L. Korte, and S. Albrecht, "Roadmap and roadblocks for the band gap tunability of metal halide perovskites," *Journal of Materials Chemistry A*, vol. 5, no. 23, pp. 11401–11409, 2017.

27. I. L. Braly, R. J. Stoddard, A. Rajagopal, A. R. Uhl, J. K. Katahara, A. K.-Y. Jen, and H. W. Hillhouse, "Current-Induced Phase Segregation in Mixed Halide Hybrid Perovskites and its Impact on Two-Terminal Tandem Solar Cell Design," *ACS Energy Lett.*, vol. 2, no. 8, pp. 1841–1847, 2017.

28. P. Caprioglio, S. Caicedo-Dávila, T. C.-J. Yang, C. M. Wolff, F. Peña-Camargo, P. Fiala, B. Rech, C. Ballif, D. Abou-Ras, M. Stolterfoht, S. Albrecht, Q. Jeangros, and D. Neher, "Nano-emitting Heterostructures Violate Optical Reciprocity and Enable Efficient Photoluminescence in Halide-Segregated Methylammonium-Free Wide Bandgap Perovskites," *ACS Energy Lett.*, vol. 6, no. 2, pp. 419–428, 2021.

29. A. J. Knight, A. D. Wright, J. B. Patel, D. P. McMeekin, H. J. Snaith, M. B. Johnston, and L. M. Herz, "Electronic Traps and Phase Segregation in Lead Mixed-Halide Perovskite," *ACS Energy Lett.*, vol. 4, no. 1, pp. 75–84, 2019.

30. A. J. Knight, J. B. Patel, H. J. Snaith, M. B. Johnston, and L. M. Herz, "Trap States, Electric Fields, and Phase Segregation in Mixed-Halide Perovskite Photovoltaic Devices," *Advanced Energy Materials*, vol. 10, no. 9, p. 1903488, 2020.

31. K. Suchan, A. Merdasa, C. Rehermann, E. L. Unger, and I. G. Scheblykin, "Complex evolution of photoluminescence during phase segregation of MAPb(I1-xBrx)3 mixed halide perovskite," *Journal of Luminescence*, vol. 221, p. 117073, 2020.

32. F. Babbe, E. Masquelier, Z. Zheng, and C. M. Sutter-Fella, "Flash Formation of I-Rich Clusters during Multistage Halide Segregation Studied in MAPbI $_{1.5}$ Br $_{1.5}$," *J. Phys. Chem. C*, vol. 124, no. 45, pp. 24608–24615, 2020.

33. S. Draguta, O. Sharia, S. J. Yoon, M. C. Brennan, Y. V. Morozov, J. S. Manser, P. V. Kamat, W. F. Schneider, and M. Kuno, "Rationalizing the light-induced phase separation of mixed halide organic–inorganic perovskites," *Nat Commun*, vol. 8, no. 1, p. 200, 2017.

34. T. Elmelund, B. Seger, M. Kuno, and P. V. Kamat, "How Interplay between Photo and Thermal Activation Dictates Halide Ion Segregation in Mixed Halide Perovskites," *ACS Energy Lett.*, vol. 5, no. 1, pp. 56–63, 2020.

35. C. G. Bischak, C. L. Hetherington, H. Wu, S. Aloni, D. F. Ogletree, D. T. Limmer, and N. S. Ginsberg, "Origin of Reversible Photoinduced Phase Separation in Hybrid Perovskites," *Nano Lett.*, vol. 17, no. 2, pp. 1028–1033, 2017.

36. W. Mao, C. R. Hall, S. Bernardi, Y.-B. Cheng, A. Widmer-Cooper, T. A. Smith, and U. Bach, "Light-induced reversal of ion segregation in mixed-halide perovskites," *Nat. Mater.*, vol. 20, no. 1, pp. 55–61, 2021.

37. R. A. Belisle, K. A. Bush, L. Bertoluzzi, A. Gold-Parker, M. F. Toney, and M. D. McGehee, "Impact of Surfaces on Photoinduced Halide Segregation in Mixed-Halide Perovskites," *ACS Energy Lett.*, vol. 3, no. 11, pp. 2694–2700, 2018.

38. A. J. Barker, A. Sadhanala, F. Deschler, M. Gandini, S. P. Senanayak, P. M. Pearce, E. Mosconi, A. J. Pearson, Y. Wu, A. R. Srimath Kandada, T. Leijtens, F. De Angelis, S. E. Dutton, A. Petrozza, and R. H. Friend, "Defect-Assisted Photoinduced Halide Segregation in Mixed-Halide Perovskite Thin Films," *ACS Energy Lett.*, vol. 2, no. 6, pp. 1416–1424, 2017.

39. S. Mahesh, J. M. Ball, R. D. J. Oliver, D. P. McMeekin, P. K. Nayak, M. B. Johnston, and H. J. Snaith, "Revealing the origin of voltage loss in mixed-halide perovskite solar cells," *Energy*

Environ. Sci., vol. 13, no. 1, pp. 258–267, 2020.

40. F. Peña-Camargo, P. Caprioglio, F. Zu, E. Gutierrez-Partida, C. M. Wolff, K. Brinkmann, S. Albrecht, T. Riedl, N. Koch, D. Neher, and M. Stolterfoht, "Halide Segregation versus Interfacial Recombination in Bromide-Rich Wide-Gap Perovskite Solar Cells," *ACS Energy Lett.*, vol. 5, no. 8, pp. 2728–2736, 2020.
41. P. Würfel and U. Würfel, *Physics of Solar Cells: From Basic Principles to Advanced Concepts*, ch. 3, pp. 41–63. Weinheim, Germany: Wiley-VCH Verlag GmbH & Co. KGaA, 3 ed., 2016.
42. U. Rau, "Reciprocity relation between photovoltaic quantum efficiency and electroluminescent emission of solar cells," *Phys. Rev. B*, vol. 76, no. 8, p. 085303, 2007.
43. P. Wurfel, "The chemical potential of radiation," *J. Phys. C: Solid State Phys.*, vol. 15, no. 18, p. 3967, 1982.

CHAPTER 3

Methods

3.1 Sample Fabrication Procedures for 2 eV Solar Cells and Absorber Materials

3.1.1 Materials

Lead(II) bromide 99.999 % (35703, Alfa Aesar), lead(II) iodide 99.999 % (44314, Alfa Aesar) cesium iodide 99.999 % (914819, Sigma-Aldrich), formamidinium bromide 99.99 % (350000, Greatcell Solar Materials), ethanol (459836, Sigma-Aldrich), isopropanol (278475, Sigma-Aldrich), dimethyl sulfoxide (276855, Sigma-Aldrich), N,N-dimethylformamide (227056, Sigma-Aldrich), chlorobenzene (284513, Sigma-Aldrich), 1,2-dichlorobenzene (240664, Sigma-Aldrich), ethyl acetate (270989, Sigma-Aldrich), Me-4PACz (M3359, TCI), aluminium oxide (702129, Sigma-Aldrich), PCBM (Special Carbon), BCP (B2694, TCI) were all used as purchased without further purification.

3.1.2 Perovskite Film Fabrication

Perovskite precursor solutions were prepared by weighing precursor salts directly in to a single vial in a molar ratio of 0.55:0.45:1 $PbBr_2$:PbI_2:FABr for $FAPb(Br_{0.7}I_{0.3})_3$ and 0.17:0.635:0.365:0.83 CsI:$PbBr_2$:PbI_2:FABr for $FA_{0.83}Cs_{0.17}Pb(Br_{0.7}I_{0.3})_3$. DMF:DMSO at a 4:1 volumentric ratio was then added to the solution at a volume corresponding to a concentration of 1.0 M of Pb-ions. The solutions were stirred over night at room temperature. Perovskite films were fabricated by spin-coating with antisolvent quenching. The spin-coating routine started with a deposition of the perovskite solution on to the stationary substrate (185 µL solution for films on ITO substrates and 300 µL solution for films on Me-4PACz/np-Al_2O_3 in e.g. devices), then a ramp of 2000 rpm s^{-1} to 6000 rpm. Ethyl acetate antisolvent (325 µL) was deposited 10 s into the spin program for $FAPb(Br_{0.7}I_{0.3})_3$ and 5 s for $FA_{0.83}Cs_{0.17}Pb(Br_{0.7}I_{0.3})_3$. The total spin program duration was 35 s from the start of the ramp for $FAPb(Br_{0.7}I_{0.3})_3$ and 45 s for $FA_{0.83}Cs_{0.17}Pb(Br_{0.7}I_{0.3})_3$. After the spin-coating procedure the substrates were immediately moved to a hotplate and annealed for 30 minutes at 110 °C. All steps took place in a N_2-filled glovebox.

3.1.3 Solar Cell Fabrication

Glass substrates with a patterned layer of ITO (10 to 15 ohm sq^{-1}, transmittance >86 %) from Biotain Crystal Co., Ltd. were cleaned by scrubbing with a toothbrush in a solution of deionized (DI) water and Decon 90 detergent. The substrates were then sonicated for a minimum of 3 minutes per step in the detergent solution, deionized (DI) water, acetone and isopropanol, and then dried using a N_2 gun.

Before the deposition of the Me-4PACz layer, the cleaned ITO substrates were exposed to a 30 min UV-Ozone cleaning process. Immediately after the completion of the UV-ozone process, the substrates were transferred to a nitrogen glovebox and the Me-4PACz deposition started. Me-4PACz was deposited by spincoating from a

solution in ethanol at a concentration of 0.33 mg mL^{-1} dissolved over night in room temperature. The solution was dropped on the stationary substrate, allowed to spread for 3-5 s and then the ramp was started with an acceleration phase of 600 rpm s^{-1} to 3000 rpm for 30 s. The samples were then immediately annealed at 100 °C for 10 min.

Next, a np-Al_2O_3 layer was deposited for improving the wetting of the following perovskite layer. The np-Al_2O_3 solution was made by a 1:150 dilution in isopropanol of the colloidal solution (702129, Sigma-Aldrich) which was stirred over night. The solution was deposited on a stationary substrate which was then subjected to 20 s of spinning at 5000 rpm with 5000 rpm s^{-1} ramp. The samples were then annealed for 2 min at 100 °C.

Following this, the perovskite layer was deposited as described in Section 3.1.2.

After the perovskite layer, a layer of PCBM was deposited. The PCBM solution was prepared at a concentration of 20 mg mL^{-1} in 3:1 chlorobenzene:dichlorobenzene which was stirred over night in room temperature and then filtered through a 0.22 µm PTFE filter shortly before spin-coating. This was spin-coated with a dynamic deposition 3 s into the spin program at 2000 rpm for 20 s, followed by an anneal at 100 °C for 5 min.

As the last spin-coated layer, a BCP layer was deposited on top of the PCBM layer. The BCP solution was prepared at a concentration of 0.5 mg mL^{-1} in isopropanol dissolved at 75 °C over night. After a static deposition, the layer was spun with a 5000 rpm s^{-1} ramp to 5000 rpm for 20 s. The annealing afterwards was 2 min at 100 °C.

After the BCP layer, samples were taken out of the glovebox and material was scraped off where electrode contact with the ITO layer was desired. The samples were then loaded into a sample holder with shadow masks and placed in a Kurt J. Lesker NANO 36 thermal evaporator for electrode deposition. The 80 nm Au electrodes were deposited in a step-wise ramp. After electrode deposition, the samples were moved to a nitrogen glovebox and stored in the dark.

3.1.4 Non-device Sample Fabrication

Full stack and p-contact samples for PLQY were fabricated the same way as described in Section 3.1.3 for the devices, except for p-contact samples no layers were deposited after the perovskite layer, and for full stack samples no shadow masks were used during the Au evaporation.

Isolated perovskite films (used for PLQY, long-duration light soak and all halide segregation PL measurements except the in-situ XRD-PL measurements shown in Figure 5.6 and Figure 5.7) and n-contact samples for PLQY were deposited on Biotain Crystal Co., Ltd. ITO glass substrates that had been treated with 80 cycles of ALD-Al_2O_3 deposited in a Picosun ALD system at 300 °C. The Al_2O_3 layer serves to insulate the ITO film to nonradiative recombination at the perovskite–ITO interface while preserving the surface roughness of the ITO layer. The UV-Ozone cleaning step prior to perovskite deposition was 10 minutes for these samples. For n-contact samples, PCBM and BCP were subsequently deposited upon the perovskite layer.

Perovskite films for the in-situ XRD-PL measurements shown in Figure 5.6 and Figure 5.7) were deposited on 1 cm^2 quartz discs.

3.2 Sample Fabrication Procedures for LEDs and LED Materials

3.2.1 Materials

Lead(II) bromide 99.999 % (35703, Alfa Aesar), cesium bromide 99.999% (429392, Sigma-Aldrich), 18-crown-6 $\geq$ 99.0 % (1,4,7,10,13,16-hexaoxacyclooctadecane, $C_{12}H_{24}O_6$, 274984, Sigma-Aldrich), TFB (Poly(9,9-dioctylfluorene-alt-N-(4-sec-butylphenyl)-diphenylamine), AD259BE, American Dye Source, Inc.), TPBi (2,2',2''-(1,3,5-Benzinetriyl)-tris(1-phenyl-1-H-benzimadizole), LT-E302, Lumtec Inc.), Tin(IV) oxide (44592, Alfa Aesar), LiF (LT-E001, Lumtec Inc.), phenylethylamine (128945,

Sigma-Aldrich), ethanol (443611, Sigma-Aldrich), dimethyl sulfoxide (276855, Sigma-Aldrich), chlorobenzene (284513, Sigma-Aldrich), and trimethylaluminum (93-1360, Strem) were all used as purchased without further purification. PEABr was prepared in-house for a previous project, see Warby et al.[1]

3.2.2 Perovskite Film Fabrication

Perovskite precursor solutions were prepared by weighing out precursor salts in a molar ratio of 5:5:2 of $PbBr_2$:CsBr:PEABr directly into a single vial. DMSO was added to the vial to a volume corresponding to the $PbBr_2$ salt being at a 0.2 M concentration. The crown ether 18-crown-6 was included in the precursor solution as a structuring agent at a concentration of 4 mg mL^{-1}. The solutions were stirred over night at room temperature and then filtered with a 0.45 µm PTFE membrane filter. Perovskite films were fabricated by spin-coating. The spin-coating program consisted of a first step of 5 s duration at 1000 rpm (1000 rpm/s ramp) followed by a second step of 60 s duration at 3000 rpm (3000 rpm s^{-1} ramp). 100 µl solution was dispensed onto the spinning substrate 1 to 2 seconds into the first step. After the spin-coating procedure the substrates were immediately moved to a hotplate and annealed for 10 minutes at 100 °C. All steps took place in a N_2-filled glovebox.

3.2.3 LED Fabrication

Glass substrates with a patterned layer of ITO ($R_\mathrm{s} \leq 10$ ohm) from Shenzhen Huayu Union technology Co. Ltd. were cleaned by scrubbing with a toothbrush in a solution of deionized (DI) water and Decon 90 detergent. The substrates were then sonicated for a minimum of 3 minutes per step in the detergent solution, deionized (DI) water, acetone and isopropanol, and then dried using a N_2 gun. Before the deposition of any layers, the cleaned ITO substrates were exposed to a 10 min UV-Ozone cleaning process.

TFB solutions were prepared by weighing out TFB powder in a vial and adding chlorobenzene to obtain the desired concentration. The solutions were stirred over night at 70 °C and then filtered with a 0.22 µm PTFE filter. When testing multiple concentrations, a solution of the highest concentration was made and then diluted into separate vials after filtering to obtain a spectrum of concentrations. TFB layers were spin-coated onto the ITO substrates in ambient air at 4000 rpm for 30 s and then annealed at 120 °C for 10 min.

A home-made ALD system was used to deposit Al_2O_3 at 100 °C. In each cycle, TMA was introduced with a residence time of 5 s before purging for 30 s. DI H_2O vapor was subsequently introduced with a residence time of 5 s and a following purge for 40 s. N_2 was used as both carrier and purge gas for the process.

LiF was deposited by thermal evaporation in a vacuum chamber positioned in a N_2 glovebox. 2 nm was evaporated for the wetting layer below the perovskite, at a rate of 0.1 Å s^{-1}. From this step onwards, the samples were kept in an inert atmosphere at all times to prevent reactions with ambient water or oxygen. Perovskite was deposited on LiF-covered substrates by spin-coating as described above.

The samples were again transferred to the thermal evaporator and a 45 nm layer of TPBi at a rate of 1 Å s^{-1} and a 1 nm layer of LiF was evaporated. Then, 80 nm Al was evaporated at a rate of 1 Å s^{-1} using an evaporation mask defining the device layout.

3.2.4 Unipolar Device Fabrication

Unipolar, electron-only devices were fabricated using the same substrates and substrate cleaning procedure as for the LEDs. A 2.67 % SnO_2 solution was made by diluting the 15 % colloidal dispersion with DI water. The SnO_2 layer was spin-coated onto the ITO substrates using a 30 s spin program at 3000 rpm and dispensing 50 µL of the solution 2 s into the program. The samples were then annealed for 30 min at 150 °C. Before spin-coating TFB on top of the SnO_2, the samples were UV-Ozone cleaned for

another 10 min to improve wetting. The TFB, Al_2O_3, TPBi, LiF and Al layers were deposited as described for the LED fabrication.

3.2.5 Sample Fabrication for PLQY

Samples for PLQY measurements were prepared in the same way as for the LEDs for all layers up to the emitter. On the ITO-only sample the perovskite was spun onto the UV-ozone cleaned ITO without a LiF wetting layer. All other layers were deposited as described above. The samples were encapsulated with glass slides bonded on top of the perovskite emitter by use of a Dymax OP-29 UV curing glue, cured for 2 minutes. The glue was dispensed by a pre-programmed robot, ensuring optimal dispensing amount and minimal flow into the center of the sample, leaving a large area of pristine perovskite for the PLQY measurements.

3.2.6 Sample Fabrication for Ellipsometry, XRR, Profilometry

Samples for determination of TFB, TFB-Al_2O_3, and SnO_2 film thickness were made on various substrates: ITO, Si, glass. In each case, the substrate was wet-cleaned as described above for LED fabrication. The substrates were then UV-ozone cleaned (ITO, Si) or plasma cleaned (glass) for 10 minutes directly prior to spin-coating TFB or SnO_2. TFB or SnO_2 were spun with the same parameters as described for LED fabrication and unipolar device fabrication.

3.2.7 Sample Fabrication for AFM, SEM and EDS

Samples for AFM and SEM with ITO substrates were prepared following the exact same steps as described for LED devices. Glass substrate samples for AFM were prepared as described above for ellipsometry, XRR and profilometry. For EDS samples with masking, a polyimide tape was placed across parts of the ITO substrate before TFB spin-coating. A part of the tape was then removed prior to ALD to reveal a

TFB-free area. To increase the surface sensitivity and reduce charging of the SEM and EDS samples, a 1 nm layer of Pt or a 5 nm layer of Au was sputtered on top.

3.3 Characterization

3.3.1 Solar Simulator Measurements

Solar cells were tested in ambient air under a simulated AM1.5 solar spectrum from a Wavelabs Sinus-220 LED array at a calibrated intensity of 100 $mW\,cm^{-2}$. The device was controlled by a 2400 series Keithley source-measure unit. During measurements, the devices were masked with a shadow mask ensuring that exactly 0.25 cm^2 of active area was illuminated.

3.3.2 EQE_{EL} Measurements

3.3.2.1 EQE_{EL} Measurements for Chapter 6

EQE_{EL} measurements on LEDs were performed using two different setups. The majority of measurements were performed using a calibrated photodiode (Thorlabs FDS 1010) directly above the LED in a N_2 glovebox. This measurement assumed a Lambertian emission profile, the view factor between the photodiode and the LED, and an electroluminescence emission spectrum measured separately using a calibrated grating spectrometer (MayaPro 2000) to calculate the total number of photons emitted. This measurement setup is described in further detail in reference[1].

In addition, some measurements were performed in an integrating sphere with the sample placed in an air-free holder mounted to the side of the sphere. The emission spectrum and intensity were simultaneously measured by an OceanOptics QEPro calibrated grating spectrometer. This setup was used to cross-reference values with the photodiode setup and to measure the spectrum as function of bias and time.

Both setups measured current density-voltage characteristics using a 2400 series Keithley source-measure unit.

To account for the dynamic nature of PeLED ageing, care was taken to measure all samples on comparable timescales since fabrication of the device. Because the PeLEDs age rapidly under bias, each pixel was scanned repeatedly until it had reached its peak efficiency. Only the peak efficiency of each pixel was used to compile the box plots in this chapter. This way, differences in efficiency due to difference in ageing time could not bias the results.

3.3.2.2 EQE_{EL} Measurements for Chapter 4

EQE_{EL} measurements on 2 eV solar cells were performed in a nitrogen-filled glovebox using a OceanInsight FOIS-1 integrating sphere connected to an OceanInsight QEPro with a 400 µm diameter optical fibre. The device was controlled with a 2400 series Keithley source-measure unit.

3.3.3 Unipolar Device Measurements

The unipolar devices were measured with the same setup used for measuring EQE_{EL} in Chapter 6. Pixels were scanned from X to -X, where X is 3 V, 5 V or 10 V. The first scan on each pixel was used to compile the 3 V snapshot plotted in the thesis.

3.3.4 EQE_{PV} Measurements

EQE_{PV} was measured on the 2 eV solar cells by Fourier-transform Photocurrent Spectroscopy (FTPS) using a Bruker 80 Fourier-transform infrared spectrometer with a xenon lamp and AM1.5 filter to provide a bias light. The EQE_{PV} was calculated by comparison of the photocurrent with that of a calibrated Si reference cell. For the measurements under halide segregation, a 610 nm LP filter was placed in front of the light beam during the measurements as an attempt to increase the dynamic range accessible in the deep Urbach tail. The LP filter was then removed again during the

light-soaking in between. The light-soaking was carried out at V_{OC} conditions with simultaneous logging of the V_{OC}

3.3.5 PLQY Measurements

3.3.5.1 PLQY Measurements for Chapter 6

PLQY measurements were carried out in an integrating sphere with encapsulated samples, fabricated as described above, following the procedure of de Mello et al.[2] Lasers with wavelength of 450 nm were used for excitation, this wavelength was carefully chosen because it is just below the absorption onset of TFB. Two different laser diodes were used: ThorLabs CPS450 and ThorLabs LP1600MM. In each case the intensity on the sample was 47.1 mW cm^{-2}. The spectrum and intensity of the photoluminescence were measured by an OceanOptics QEPro calibrated grating spectrometer. For each sample, 3 measurements were taken each in a different location on the sample. Care was taken each time to ensure the laser spot hit a location within the encapsulated area of the sample. The average PLQY of the 3 measurements were then calculated per sample and used as 1 data point for the analysis and plots in the paper.

3.3.5.2 PLQY Measurements for Chapter 4

PLQY measurements on 2 eV solar cell absorbers were carried out in an integrating sphere following the de Mello method[2] and using a ThorLabs LP1600MM laser diode with a 450 nm wavelength. The laser passed through a filter wheel adjusted such that the intensity (40.6 mW cm^{-2}) hitting the sample was the equivalent of the number of above-bandgap photons for a 2 eV absorber under 1 Sun equivalent intensity at AM1.5 spectrum.

The samples were stored in the dark in nitrogen up until the measurement and only one sample was taken out of the glovebox at the time, after which it was immediately measured, to avoid oxygen-passivation influencing the results.

3.3.6 Absorbance Measurements

Absorbance measurements of a green perovskite film for LED (Figure 6.1 (a)) and a 2 eV solar absorber perovskite film (Figure 4.1 (a)) spun directly on microscope glass slides were measured on a Cary 300 Bio UV-visible spectrophotometer.

3.3.7 Profilometry Measurements

Profilometry was carried out on a Veeco Dektak 150 profilometer. A razor blade was used to scrape a line in the film and the profile of the line was measured.

3.3.8 Ellipsometry Measurements

Ellipsometry was carried out on a J.A. Woollam RC2 spectroscopic ellipsometer. Samples were measured at 3 to 5 angles between 50 and 75 °. In each case, a clean substrate was measured first and used as foundation for the model of the samples. Fitting was performed in CompleteEASE. The TFB material was fitted by a Cauchy fit in the transparent region which was then extrapolated into the absorbing region by a B-spline. This gave an excellent fitting result. A Cauchy fit in the transparent region was also used to determine the thickness of SnO_2, again with an excellent fit. For TFB-Al_2O_3 layers, several models were tried, including Cauchy fits in the transparent region, planar bilayers (TFB then Al_2O_3), and Bruggeman effective medium approximations (EMAs) with TFB and Al_2O_3. All methods gave very similar results for the thickness. In the end, a Cauchy fit in the transparent region was used to get the data presented in 6.15.

3.3.9 XRR Measurements

X-ray reflectivity (XRR) data was acquired with a Rigaku SmartLab diffractometer. This comprised a 1.8 kW (Cu K_α, 1.5406 Å) source with parallel beam optics with a 10 mm length limiting slit and 2.5 ° Soller slits. The samples were measured from 0

to 4 ° with a step size of 0.01 ° in continuous mode. X-ray scattering was collected with a HyPix-3000 2D hybrid pixel-array detector at a sample-to-detector distance of 300 mm. Data was processed using GenX ver. 3.4.1169 and the film thickness was fitted as a single layer polymer layer on the substrate with density and roughness parameters of the substrate and film allowed to float.

3.3.10 Ex-situ XRD Measurements

1-dimensional X-ray diffraction measurements were performed in a Panalytical X'pert diffractometer using a Cu K_α X-ray source in Bragg-Brentano geometry. The sample specimens were thin-film samples on glass substrates fixed into sample holders by use of plasticine. Care was taken to align the surface of the samples as flush as possible with the rim of the sample holder.

3.3.11 In-situ XRD-PL Measurements

The in-situ XRD-PL measurements were performed in the same Rigaku SmartLab diffractometer described in Section 3.3.9. The perovskite film on a quartz sample was illuminated by an LDH-D-C-470 fibre-coupled laser and the emitted PL was collected with another fibre and measured in an Ocean Optics USB2000 spectrometer. The diffracted X-ray signal was measured with a HyPix-3000 2D hybrid pixel-array detector at a sample-to-detector distance of 300 mm. The measurement setup has been described in detail by Knight et al.[3]

3.3.12 Light-soaking

Light-soaking between XRD measurements of data presented in Figure 5.8 was performed in a home-built light-soaking rig using a Viparspectra V450 LED array lamp with only the "Veg" array activated. The spectrum of the lamp was measured using an OceanOptics QEPro spectrometer and the samples were positioned at a distance

to the lamp where the number of above-bandgap photons for a 2.0 eV absorber was equivalent to that of 1 Sun AM1.5. The intensity as function of distance was measured with a certified reference Si photodiode.

The samples were placed on top of Laird Thermal Systems 66100-501 Thermoelectric Peltier Modules controlled by a TTi QL564P power supply unit. The power supply was set to deliver a current that would cause the temperature on top of the sample (at the perovskite film level) to converge to a value in between 20 and 25 °C under the illumination from the lamp. The convergence was tested prior to the experiment by an overnight measurement with a Type K thermocouple and an RS-9663 multimeter. The temperature was found to converge within an hour.

When the samples under investigation were taken off for XRD measurement, they were measured for 20 minutes each and returned one-by-one to the light-soaking rig such that they would only spend ~30 min outside the rig each. This was repeated up until the 2900 min mark, after which all samples were taken off the rig simultaneously and measured in a batch measurements, before being returned approximately 90 min later.

Samples that were stored in the dark were kept in black, opaque boxes in a drawer in ambient air or nitrogen and immediately returned there after measurement. Lights were turned off in the XRD instrument during measurements, although room lighting would still cause some light exposure. The samples stored in ambient air would have the opaque box slightly opened and the drawer slightly opened to allow equilibration of the atmosphere in the box with the ambient atmosphere, while allowing no direct light and extremely little diffuse light to hit the sample.

3.3.13 XRD Peak Identification

Peak identification in diffractograms was carried out using fitting algorithms in Topas Academic, fitting the diffraction data to crystal structures from the ICSD database with a Pseudo-Voigt peak type.

3.3.14 SEM and EDS Measurements

Scanning electron microscopy was performed on a FEI Quanta 600 FEG microscope using secondary electron mode. For top-down measurements, accelerating voltage was kept as low as possible to reduce penetration depth and enhance surface sensitivity of the low-density polymer surface. EDS was performed in the same SEM, using an x-act detector from Oxford Instruments. EDS was done at 10 keV.

3.3.15 AFM Measurements

Atomic Force Microscopy measurements were carried out using an Asylum MFP3D microscope in AC (tapping) mode in air. Olympus AC240-TS silicon tips were used for topography measurements.

3.3.16 PL Measurements in Inert Atmosphere

The PL data displayed in Figure 5.1 and Figure 5.2 was recorded in a confocal PL microscopy setup using a 450 nm wavelength ThorLabs CPS450 laser diode with a spot size of approximately 2 mm diameter. The signal was measured with a Princeton Instruments Pylon spectrometer with grating 300 g/mm, blaze 500 nm, center 730 nm. A 530 nm LP filter was placed between the sample and the detector to filter out the laser signal and the beam then went through a lens to focus onto the detector.

The measurement in ambient atmosphere (Figure 5.1 (b) and Figure 5.2 (b)) was performed with the sample exposed to the ambient atmosphere of the room. For the inert atmosphere measurement (Figure 5.1 (a) and Figure 5.2 (a)) the sample was placed in a sealed air-free holder designed in-house. The sample was loaded into the holder in a glovebox in inert atmosphere and the sample holder was then sealed off before being taken for measurement. In both cases, care was taken to ensure absolutely minimal oxygen and light exposure prior to measurement.

3.3.17 PL Measurements in Ambient Atmosphere

The PL data displayed in Figures 4.1, 5.4, 5.5, 5.9 and 5.10 was all collected in an integrating sphere in ambient air using a ThorLabs LP1600MM laser diode with a 450 nm wavelength. The laser passed through a filter wheel adjusted such that the intensity hitting the sample was the equivalent of the number of above-bandgap photons for a 2 eV absorber under 1 Sun equivalent intensity at AM1.5 spectrum, except for Figures 5.3 and 5.4 where the intensity was equivalent to 4 Suns. The samples were stored in the dark in nitrogen up until the measurement after which they were immediately measured, to avoid oxygen-passivation influencing the results. With the exception of the samples in Figures 5.3 and 5.4 that were exposed to different atmospheres prior to measurement, as noted in the figures and in the text in the chapters.

For the cycled PL measurements, a python script was written that controlled the shutter and the spectrometer such that the laser was blocked and unblocked, and spectra saved at the desired times.

References

1. J. H. Warby, B. Wenger, A. J. Ramadan, R. D. J. Oliver, H. C. Sansom, A. R. Marshall, and H. J. Snaith, "Revealing Factors Influencing the Operational Stability of Perovskite Light-Emitting Diodes," *ACS Nano*, vol. 14, no. 7, pp. 8855–8865, 2020.

2. J. C. de Mello, H. F. Wittmann, and R. H. Friend, "An improved experimental determination of external photoluminescence quantum efficiency," *Adv. Mater.*, vol. 9, no. 3, pp. 230–232, 1997.

3. A. J. Knight, J. Borchert, R. D. J. Oliver, J. B. Patel, P. G. Radaelli, H. J. Snaith, M. B. Johnston, and L. M. Herz, "Halide Segregation in Mixed-Halide Perovskites: Influence of A-Site Cations," *ACS Energy Lett.*, vol. 6, no. 2, pp. 799–808, 2021.

CHAPTER 4

Loss Estimations in 2 eV Perovskite Solar Cells

4.1 Introduction

In this chapter we investigate and quantify the different causes for loss of photovoltaic efficiency in our Cs-free, formamidinium-based 2 eV perovskite solar cells, with a particular focus on the various reasons for V_{OC}-loss. We combine device-characterization measurements under a solar simulator, including measurements such as JV-scans, steady-state measurements and prolonged maximum power point tracking, with $\mathrm{EQE_{PV}}$ and $\mathrm{EQE_{EL}}$ measurements, as well as optical PLQY measurements on partial device layer stacks, to quantify the magnitude and proportion of nonradiative losses. We then determine the radiative losses due to halide segregation by a combination of $\mathrm{EQE_{PV}}$ measurements under light-soaking and simultaneous V_{OC} tracking.

Of the work presented in this chapter, work is credited as follows: Dr. Zhongcheng Yuan performed the $\mathrm{EQE_{EL}}$ measurements in tandem with the author with Dr. Yuan

serving as the instrument expert and the author designing the measurement protocol, the author performed all the EQE_{EL} data analysis; Dr. Jay Patel performed the EQE_{PV} measurements using FTPS in tandem with the author with Dr. Patel serving as the instrument expert and the author designing the measurement protocol, the author performed all the EQE_{PV} data analysis but with a script provided by Dr. Patel for the processing of the raw data, Dr. Suhas Mahesh provided guidance on the measurement protocol and data analysis; the devices were made with a device architecture recipe supplied by James Drysdale and Benjamin Putland. All other experimental work and data analysis was performed solely by the author, with discussions over the results with Prof. Henry Snaith, Dr. Pietro Caprioglio and Dr. Joel Smith.

4.2 Results

4.2.1 Device Characteristics

We use $FAPb(Br_{0.7}I_{0.3})_3$ as a model system to investigate the effects on V_{OC} from the interfaces and halide segregation, respectively. This material has a bandgap at 2.005 eV determined by the position of the inflection point of the absorption onset calculated from the photovoltaic external quantum efficiency (EQE_{PV}) spectrum and a mixed-phase PL peak at 631 nm (1.96 eV), as shown in Figure 4.1 (a). The material is also prone to halide segregation, as evidenced in Figure 4.1 (b), where we show the change in PL spectrum over 30 s for a sample measured in air under 1 Sun equivalent photon flux.

To test the performance of our material in a photovoltaic device, we fabricate p-i-n devices with an architecture of ITO / Me-4PACz / np-Al_2O_3 / $FAPb(Br_{0.7}I_{0.3})_3$ / PCBM / BCP / Au. Data from JV-scans and max power point (MPP) tracking of our champion device are shown in Figure 4.2 (a) and (b), respectively. In Figure 4.2 (c), we show the steady-state data of the same device held at J_{SC} and V_{OC} (tracked in separate measurements but plotted along same time axis). The champion PCE

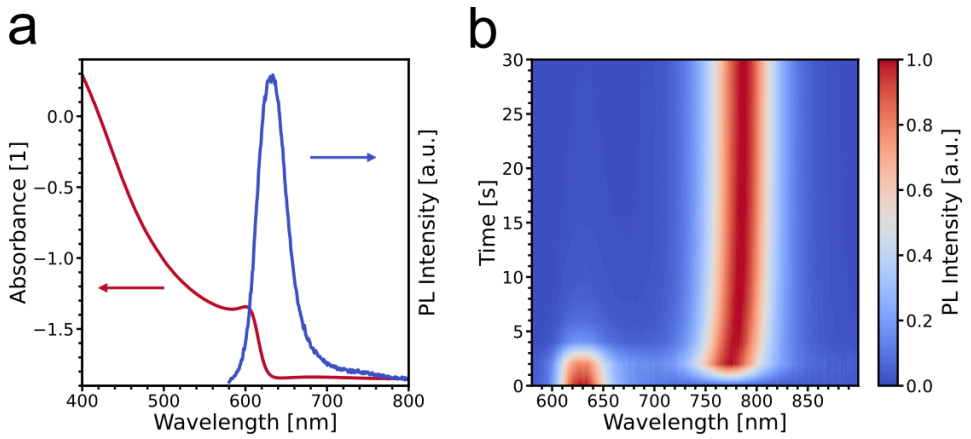

Figure 4.1: Absorbance (red) and photoluminescence (blue) spectra of a $FAPb(Br_{0.7}I_{0.3})_3$ material (a), and contour plot of the photoluminescence spectrum as function of time of a $FAPb(Br_{0.7}I_{0.3})_3$ material during halide segregation under 1 Sun equivalent intensity (b). The contour plot shows the normalized intensity at each time point, where an intensity of 1 indicates the highest intensity of the spectrum in that time point.

in the reverse scan is 12.69 % and in the forward scan it is 11.28 %. The scan speed is 0.39 V s^{-1}. From MPPT the stabilized PCE is determined to be 12.13 %. With a stabilized V_{OC} of 1.373 V, this is the highest V_{OC} reported for a device of similar bandgap to our knowledge. The stabilized J_{SC} is 11.66 mA cm^{-2} and the steady-state fill factor (FF) is 0.758.

In Figure 4.2 (d) we show the steady-state device statistics from a batch of our devices. The values scatter a lot due to pinholes in the perovskite film. (A reproducibility issue varying greatly from batch to batch that we so far have not succeeded to eliminate.) In the shown statistics, 14 out of 27 devices have been removed in the data cleaning. First, by applying a cut-off at a FF of 0.3, thus removing completely shunted devices ($FF \approx 0.25$). Then, by finding the median PCE of the remaining devices and removing all devices below half of the median. Despite this, some of the remaining 13 devices are plagued with poor performance due too low shunt resistance, likely because of the presence of smaller pinholes. Among the plotted devices, the median steady-state PCE, FF, V_{OC} and J_{SC} are 10.41 %, 0.699, 1.339 V and 11.36 mA cm^{-2}, respectively. Figure 4.3 (a) displays the photovoltaic external quantum efficiency (EQE_{PV}) of a representative device.

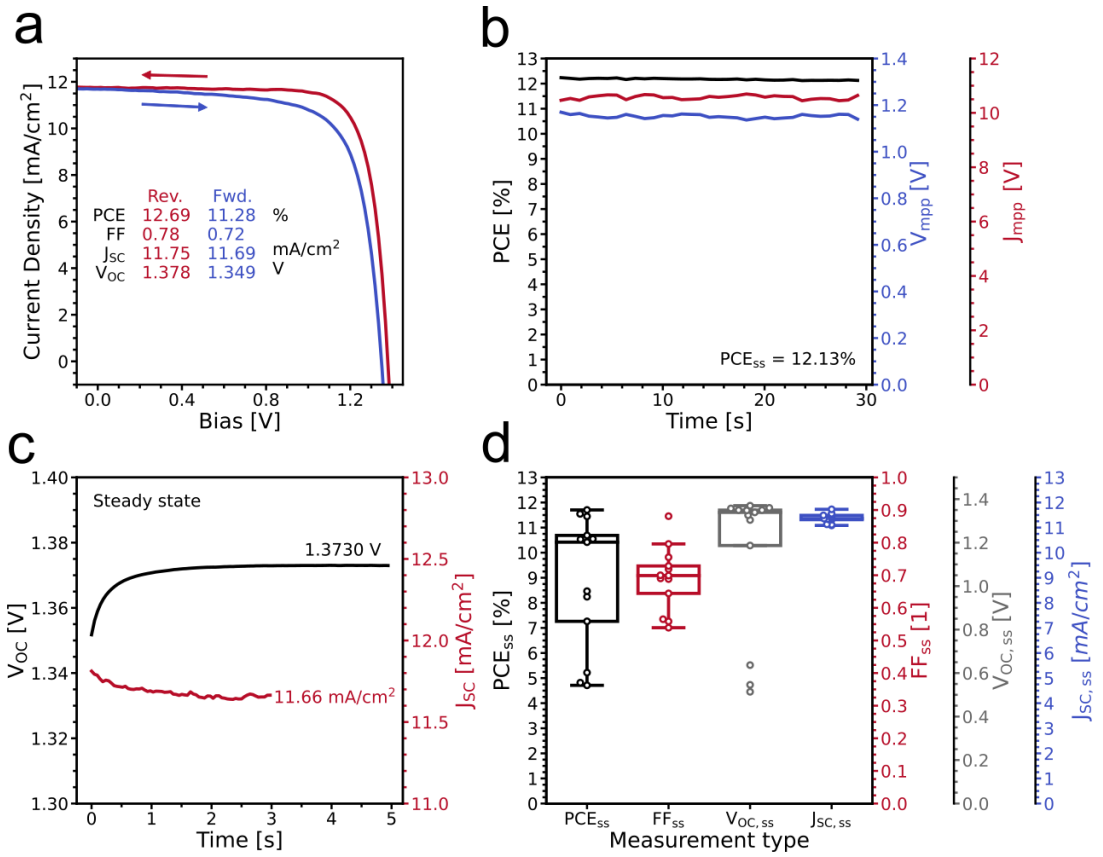

Figure 4.2: JV-curves in reverse and forward scan direction for the champion device (a), max power point tracking (b), and measurements of stabilized V_{OC} and J_{SC} for same device (c). Device statistics from a batch of devices (d). All device data shown in this figure panel comes from devices measured with a mask with an aperture area of 0.25 cm^2.

4.2.2 Loss Estimations: Nonradiative Losses

We note that the V_{OC} values we measure are well below the theoretical maximum at 1.683 V , predicted by detailed balance calculations for an absorber of 2.000 eV bandgap at 298.15 K under AM1.5G.[1] The difference down to the measured steady-state V_{OC} value of our champion is 310 mV. To learn what are the dominating reasons for our losses, we investigate the contribution to the V_{OC} loss from the initial quality of the bulk perovskite, nonradiative losses at the interfaces, and losses due to halide segregation. To start, we relate the photoluminescence quantum yield ($PLQY$) of our samples to the quasi-Fermi level splitting ($QFLS$) through the relation derived in Equation (2.12) and make the approximation $J_{\mathrm{G}} \approx J_{\mathrm{SC}}$:

$$\begin{aligned} QFLS &= QFLS_{\mathrm{rad}} + k_{\mathrm{B}}T \ln\left\{PLQY\right\} \\ &= k_{\mathrm{B}}T \ln\left\{\frac{J_{\mathrm{G}}}{J_{0,\mathrm{rad}}}\right\} + k_{\mathrm{B}}T \ln\left\{PLQY\right\} \\ &\approx k_{\mathrm{B}}T \ln\left\{\frac{J_{\mathrm{SC}}}{J_{0,\mathrm{rad}}}\right\} + k_{\mathrm{B}}T \ln\left\{PLQY\right\}. \end{aligned} \tag{4.1}$$

Where $QFLS_{\mathrm{rad}}$ is the $QFLS$ in the radiative limit (i.e. $PLQY = 100\,\%$), J_{G} is the carrier generation current density, $J_{0,\mathrm{rad}}$ is the dark recombination current in the radiative limit, and J_{SC} is the short-circuit current. In the event of no bending of the $QFLS$ and that both quasi-Fermi levels align with the work functions of the contacts, qV_{OC} will equal the $QFLS$.[2] We assume the temperature to be 300 K and make the assumption that all charges are collected at the contacts, such that $J_{\mathrm{G}} = J_{\mathrm{SC}}$. J_{SC} is estimated by the overlap integral of the AM1.5G spectrum with the EQE_{PV} of a cell, resulting in the integrated J_{SC} shown in Figure 4.3 (a). The equation is:

$$J_{\mathrm{SC}} = q \int EQE_{\mathrm{PV}}(E)\phi_{\mathrm{AM1.5}}(E)dE. \tag{4.2}$$

To estimate $J_{0,\mathrm{rad}}$, we take the overlap integral of the EQE_{PV} with the blackbody spectrum at 300 K:

$$J_{0,\mathrm{rad}} = q \int EQE_{\mathrm{PV}}(E)\phi_{\mathrm{BB}}(E)dE. \tag{4.3}$$

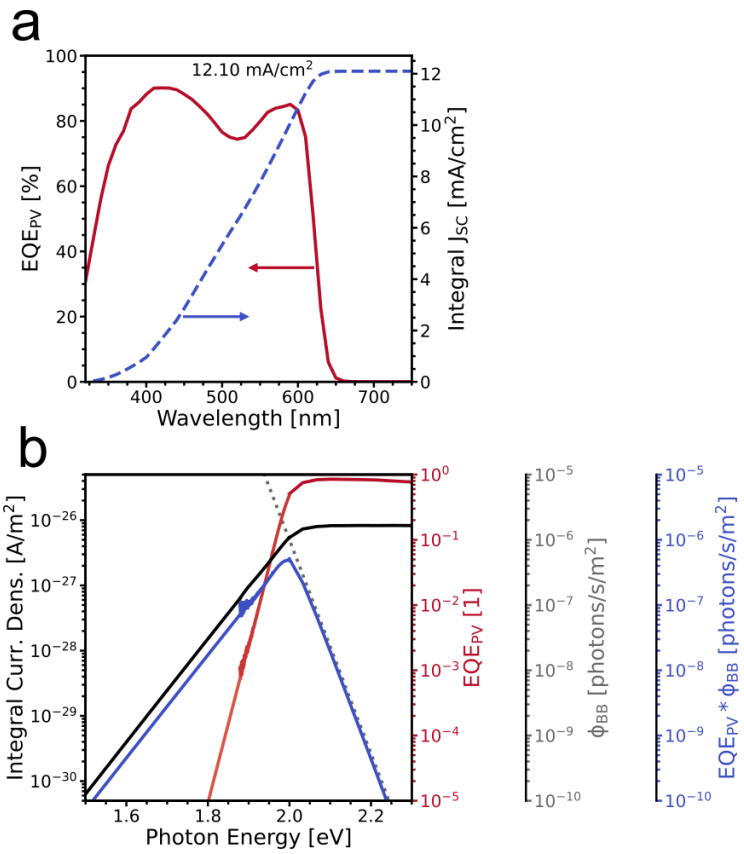

Figure 4.3: EQE_{PV} (red) and integral short-circuit current density (blue) from the integral of EQE_{PV} and the solar spectrum (a). EQE_{PV} with extrapolated Urbach tail (red), blackbody spectrum, ϕ_{BB}, at 300 K (grey), product of EQE_{PV} and ϕ_{BB} (blue), and the integral of $EQE_{\mathrm{PV}} \cdot \phi_{\mathrm{BB}}$ (black) (b).

Due to the rapid increase in ϕ_{BB} towards lower photon energies, this integral is dominated by the integrand in the Urbach tail of the EQE_{PV} spectrum. Because the noise floor of our EQE_{PV} measurements prevents us from getting accurate values for the integrand in the deepest parts of the Urbach tail, we approximate the EQE_{PV} values from 1.88 eV and below by fitting the Urbach tail to an exponential and extrapolating down to 0.1 eV. In Figure 4.3 (b) we show the extrapolation of the EQE_{PV} (red), the blackbody spectrum ϕ_{BB} (grey), the product of $EQE_{\mathrm{PV}} \cdot \phi_{\mathrm{BB}}$

(blue) and the current density from the integration over the product as given in Equation (4.3).

In Figure 4.4 (a) we plot the $PLQY$ values of both isolated perovskite films and perovskite films on our p-contact (ITO/Me-4PACz/np-Al_2O_3). We also measured both perovskite films with the n-contact (PCBM/BCP) and full device stacks, but none of these samples were radiative enough to be visible above our detection limit of 0.01 % $PLQY$. The right y-axis in Figure 4.4 (a) displays the equivalent $QFLS$ to the $PLQY$ value on the left y-axis. We calculate a $QFLS_{\mathrm{rad}}$ of 1.678 eV, only 5 meV below the detailed balance qV_{OC} limit. The measured $PLQY$ values are, however, all below 0.05 %. The average $QFLS$ of the isolated perovskite films is 1.466 eV, 212 meV below the $QFLS_{\mathrm{rad}}$. The samples on the p-contact are another 17 meV below this again, whereas the n-contact quenches the $PLQY$ below the detection limit so the $QFLS$ must be below 1.438 eV for these samples and the full device. To get an indication of how much the n-type interface quenches the $QFLS$, we add two more values to the plot in Figure 4.4 (a): the qV_{OC} from the steady-state value of our champion device (as reported in Figure 4.2 (c)) and the determined EQE_{EL} of the unsegregated majority phase from a similar device (as to be addressed in Section 4.2.3 and Figure 4.5 (a) and (b)). These values are another 76-90 meV below that of the $QFLS$ of the perovskite with film on the p-type contact, suggesting that the nonradiative losses because of the n-type contact are on this order.

4.2.3 Loss Estimations: Halide Segregation

Further, we want to quantify the effect of halide segregation on the V_{OC} loss. For this, we make use of Fourier Transform Photocurrent Spectroscopy (FTPS). With this technique, an interferometer is used to scan the sample photocurrent response (which also acts as detector) in the time domain. Applying a Fourier transform, the data is transformed to the frequency or wavelength domain to give the spectral dependence. The technique is advantageous because measurements can be taken over

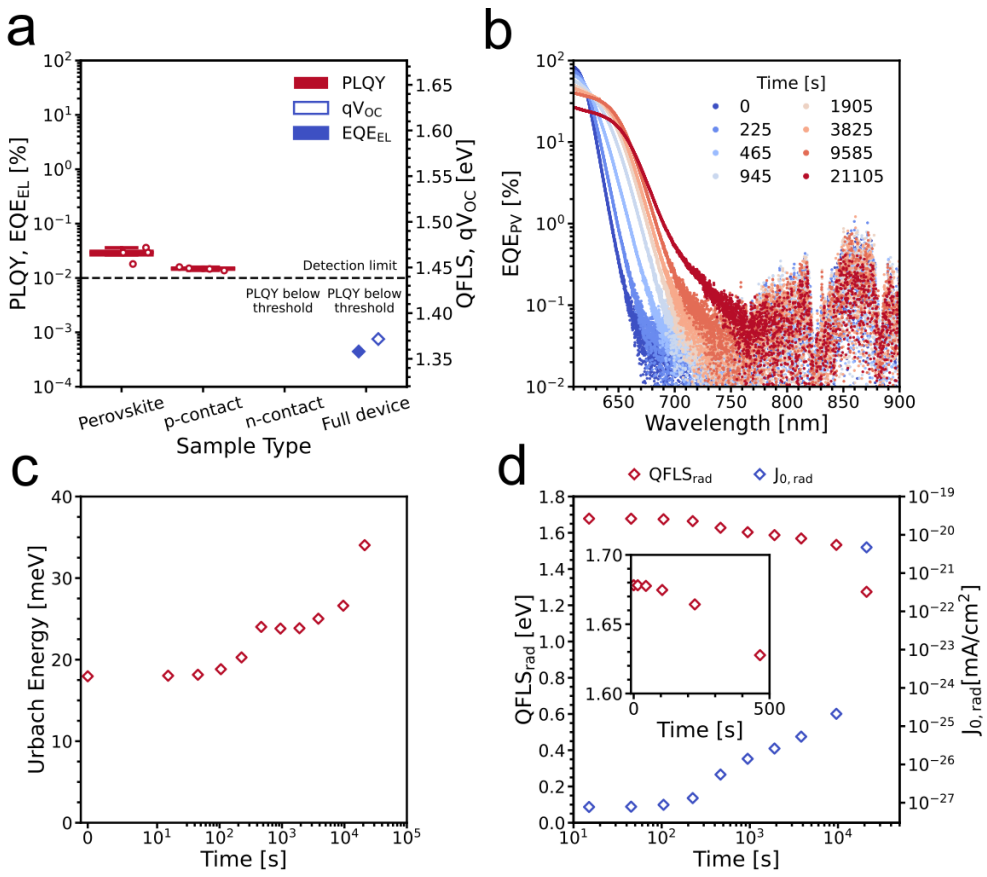

Figure 4.4: (a) In red: Photoluminescence quantum yield (PLQY) measurements of isolated perovskite films, perovskite films with p-contact interface, perovskite films with n-contact interface, and a full device stack, respectively. The second y-axis shows the equivalent calculated quasi-Fermi level splitting. In blue: the measured EQE_{EL} of a device and the champion, steady-state qVoc. (b) EQE_{PV} in the Urbach tail of a device measured with FTPS between light-soaking steps at open circuit at 1.15 Sun equivalent intensity. (c) Urbach energy extracted from the data presented in (b). (d) In blue: $J_{0,\mathrm{rad}}$ calculated using the EQE_{PV} data presented in (b); (d) in red: QFLS in the radiative limit calculated using the data from (b) and (c). The inset shows the first 500 s on a linear x-axis and a narrower y-axis range.

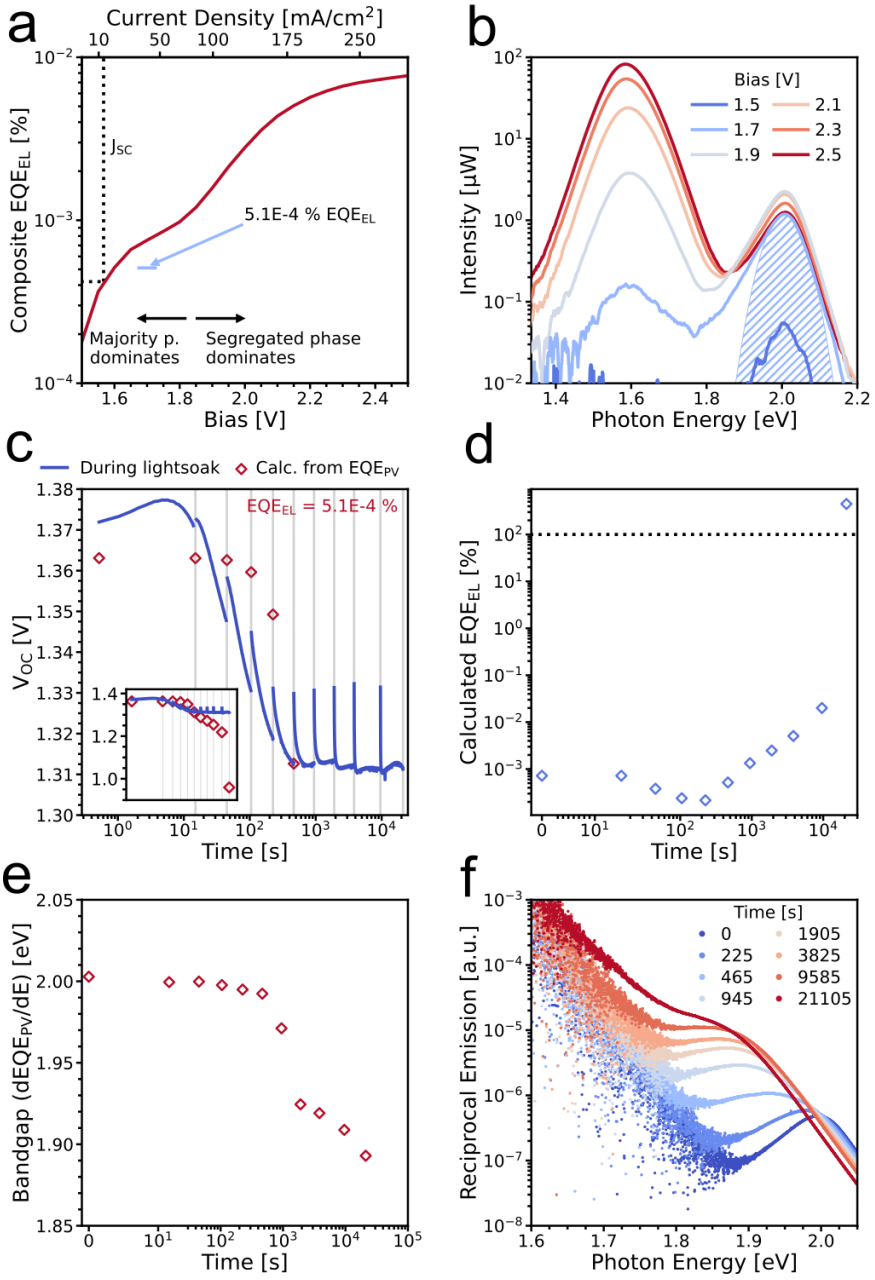

Figure 4.5: (a) EQE_{EL} integrated over the entire spectrum as function bias voltage and current density. The dotted line indicates the EQE_{EL} and current density at J_{SC}. The light blue marker indicates the EQE_{EL} of the majority phase at 1.7 V. (b) Electroluminescence spectrum at some bias values from the JV scan presented in (a). The shaded area represents the gaussian fitting used to extract the EQE_{EL} of the mixed majority phase. (c) Measured V_{OC} (blue) during light-soaking steps at open circuit. Grey lines indicates the position of interruptions in the light-soaking where the EQE_{PV} was measured with FTPS. In red: The calculated V_{OC} based on the EQE_{PV} data. The inset shows the same data on the same x-axis but with a larger y-axis range. The EQE_{EL} used for the V_{OC} calculations is specified. (d) Calculated EQE_{EL} needed for the calculated V_{OC} to follow the measured V_{OC} in (c). The dotted line indicates 100 % EQE_{EL}, the upper limit. (e) The inflection point bandgaps from $dEQE_{\mathrm{PV}}/dE$ of the EQE_{PV} data from the light-soaking measurements. (f) Reciprocal emission calculated from the EQE_{PV} data and the inverse of the blackbody spectrum, ϕ_{BB}, at 300 K.

short exposure times and still yield high sensitivity over a wide dynamic range. Using an appropriately chosen longpass (LP) filter to prevent saturation from the highest photocurrents, high resolution in the sub-bandgap domain can be achieved. We take a representative device and perform EQE_{PV} measurements using FTPS at logarithmic intervals, while light soaking at V_{OC} at 1.15 Suns in between measurements. The EQE_{PV} measurements were done with a LP filter at 610 nm in an attempt to improve dynamic range and probe deep into the Urbach tail. Eight of the EQE_{PV} scans are shown in Figure 4.4 (b). With increasing time, we see a gradual increase in the slope of the absorption onset, a red-shift of the onset, as well as a drop in the above-gap EQE_{PV}.

By making an exponential fit to the steepest part of Urbach tail, we estimate the Urbach energy as function of time. In Figure 4.4 (c), the evolution of the Urbach energy is plotted against a logarithmic time axis. The Urbach energy starts at 18 meV and rapidly increases to 24 meV over the first 500 s, where it then plateaus for another 500 to 1000 s before it starts rising again. After 2×10^{-3} s of light soaking, the Urbach energy measures 34 meV.

Analysing the FTPS data further, we calculate an estimation of $QFLS_{\mathrm{rad}}$ as function of time using Equation (4.1). Because we do not have valid EQE_{PV} data above the bandgap as function of time (due to the LP filter), we make the approximation that the EQE_{PV} in this region of the spectrum stays constant – although, it can be seen from Figure 4.4 (b) that this is not entirely the case. Regardless, the resulting change to the J_{SC} is expected to be less than an order of magnitude. The generation rate, and thus our proxy J_{SC}, will also be affected by the change of the absorption profile below the bandgap. However, this part of the spectrum contributes less than 10 % of the J_{SC} value and the changes in this region of the absorption profile that we observe only affect the third digit of the J_{SC} value, so we keep the J_{SC} value constant in the $QFLS_{\mathrm{rad}}(t)$ calculations. $J_{0,\mathrm{rad}}$, on the other hand, is strongly dependent on the sub-bandgap absorption profile and we find that this quantity varies over nearly 7 orders of magnitude based on our calculations (blue diamonds in Figure 4.4 (d)).

The $QFLS_{\mathrm{rad}}$ calculations (red diamonds in Figure 4.4 (d) and the inset) are thus dominated by the change in $J_{0,\mathrm{rad}}$. After 500 s, the $QFLS_{\mathrm{rad}}$ calculated has fallen 50 meV to 1.628 eV. After 160 min (9600 s), the drop from the initial value is 145 meV and after 350 min (21000 s) it is 404 meV.

Following Equation (2.18) and Equation (2.19), we can write:

$$V_{\mathrm{OC}} \approx k_{\mathrm{B}}T \ln\left\{\frac{J_{\mathrm{SC}}}{J_0}\right\} = k_{\mathrm{B}}T \ln\left\{EQE_{\mathrm{EL,majority}}\frac{J_{\mathrm{SC}}}{J_{0,\mathrm{rad}}}\right\}, \tag{4.4}$$

if we have the EQE_{EL} of the device, we can use the estimated $J_{0,\mathrm{rad}}$ to calculate $J_0 = J_{0,\mathrm{rad}}/EQE_{\mathrm{EL}}$ and the V_{OC}. In Figure 4.5 (a) we plot the EQE_{EL} as function of bias in a voltage sweep from 0 to 2.5 V on one of our representative devices, while in (b) we plot a selection of the electroluminescence spectra from the same measurement. The device starts with no visible halide segregation but then halide segregation quickly becomes visible as a separate peak. To try to estimate the EQE_{EL} of the unsegregated majority phase, we fit a gaussian to one of the spectra before the halide-segregated phase becomes large enough that a significant portion of the carriers funnel into this lower-bandgap phase. The fit is shown in the shaded region of Figure 4.5 (b) and covers a photon flux equivalent to an EQE_{EL} of 5.1×10^{-4} %, as also indicated in Figure 4.5 (a). We note that the current density at the bias where the fit was made is 3 times higher than our typical J_{SC} current density, however, reading off the data in Figure 4.5 (a) we find that the EQE_{EL} where the current is approximately J_{SC} (between 1.55 and 1.60 V bias in this case) is approximately 4×10^{-4} %, and there is likely to be some variation between samples, so the error is likely to be small compared to the observed changes in $J_{0,\mathrm{rad}}$.

We tracked the V_{OC} of the device during the light-soaking stages between the EQE_{PV} measurements, the V_{OC} values are shown as function of time as the blue lines in Figure 4.5 (c). At logarithmic intervals, the device is taken off the open-circuit condition and the FTPS measurement is performed at short-circuit conditions to extract the EQE_{PV}, this is indicated with grey vertical lines in the plot. The V_{OC} is

also estimated using Equation (4.4) and this is plotted as red diamonds over the grey vertical lines. In the inset, the data is plotted on the same, logarithmic time axis, but with a larger y-axis window to show all the V_{OC} estimations. Inspecting the figure, it is clear that the V_{OC} estimations initially underestimate the real V_{OC} of the device by almost 10 meV. The real value starts at 1.372 V and rises to a peak at 1.377 V within 10 s before starting to fall, whereas the estimation starts at 1.363 V. Furthermore, when the tracked V_{OC} drops off rapidly between 10 and 500 s into the experiment, the estimations lag behind in the initial drop phase. The tracker data then plateaus at 1.312 to 1.313 V and the device V_{OC} remains at this level for the following 5.5 h (350 min, 21000 s). The V_{OC} estimation, on the other hand, keeps dropping like the $QFLS_{\mathrm{rad}}$ and $J_{0,\mathrm{rad}}$ estimations in Figure 4.4 (d) and reaches 0.959 V after 350 min.

Because the V_{OC} estimation in Figure 4.5 (c) does not follow the measured V_{OC} very well, we calculate required EQE_{EL} in Equation (4.4) to make the V_{OC} estimations follow the measured V_{OC}. (While still keeping the J_{SC} constant and using the same $J_{0,\mathrm{rad}}(t)$ values as before.) The EQE_{EL} values are plotted in Figure 4.5 (d). The EQE_{EL} starts out slightly higher than our original estimation, at 7.2×10^{-4} % rather than 5.1×10^{-4} %, then drops to a low at 2.2×10^{-4} % after 225 s, picks up to 5.2×10^{-4} % after 500 s and then steadily climbs through the 10^{-3} s and reaches 2.0×10^{-2} % after 9500 s. After 21000 s the value is nonreal at over 400 %.

Because the absorption onset in Figure 4.4 (b) seems to shift a lot, we determine the new inflection points of the absorption profile by finding the maximum in $dEQE_{\mathrm{PV}}/dE$ and in Figure 4.5 (e) we plot this as bandgap as function of time. (The $dEQE_{\mathrm{PV}}/dE$ method is the same method we used to determine the bandgap of our films in the first place.) We can see the apparent bandgap takes on a small, continuous drop in the beginning, from 2.002 to 1.992 eV in the first 500 s, it then drops to 1.92 eV by the 2000 s mark before it continues dropping to 1.89 eV after 21000 s.

Since our $QFLS_{\mathrm{rad}}$ and our V_{OC} calculations depend on the reciprocity theorems, we apply Rau's first reciprocity theorem, Equation (2.17), and calculate and plot the reciprocal emission in Figure 4.5 (f) through the relation $\phi_{\mathrm{emitted}}(E) \propto$

$EQE_{\mathrm{PV}}(E)\phi_{\mathrm{BB}}(E)$. If the reciprocity condition is fulfilled, the resulting emission spectra should look similar to the emission spectra we see from PL or EL. Inspecting Figure 4.5 (f), it is clear that the noise floor of our EQE_{PV} measurements is unfortunately too high to be able to observe the very red-shifted, halide-segregated peak we observe in e.g. Figure 4.5 (b). The initial reciprocal spectrum has an emission peak situated at the expected position close to 2.00 eV. Over the course of the experiment, this peak seems to be gradually red-shifting.

4.2.4 Max Power Point Tracking

To get an insight into how operation at MPP, where most excited charges are extracted, might differ from light soaking at V_{OC}, where all excited charges must recombine, we performed a 2 h MPP tracking in the solar simulator under 1 Sun on a device. JV measurements are shown in Figure 4.6 (a) and the MPP tracking in (b). For unknown reasons, the device shows a remarkably low V_{mpp} at the start of the MPP tracking (possibly due to ion distribution). The V_{mpp} then quickly improves from approximately 0.8 V to 1.1 V in the first 500 s of the measurement. The V_{mpp} then slowly drops 0.5 to 1.0 V between 500 and 2000 s, before recovering that loss again by 4500 s, after which it stabilizes around 1.13 V for the remainder of the measurement. The PCE trajectory follows the V_{mpp} during the sharp rise in the beginning and from thereon is determined mainly by the J_{mpp}. The J_{mpp} starts around 9 mA cm^{-2} but then takes a sharp drop to a minima around 6 mA cm^{-2} after 1500 s. In the next 2000 s there is a slow increase over about 0.5 mA cm^{-2} before the J_{mpp} goes into a continuous linear decline from approximately 4000 s and until the end, reaching below 4.5 mA cm^{-2} at the end of the measurement. Comparing the pristine JV curves with the JV curves after the MPP tracking, we can see the curves after the tracking has a near-pristine V_{OC}, but an almost halved J_{SC} and a large hysteresis.

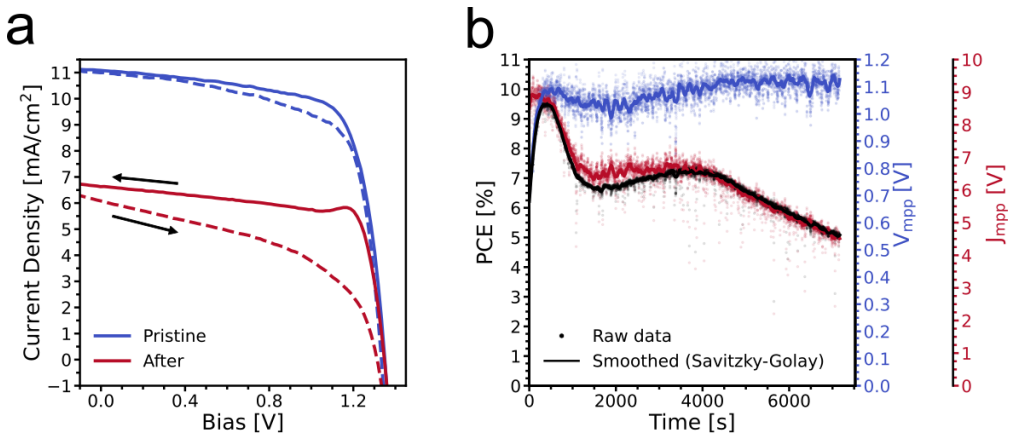

Figure 4.6: (a) JV-curves in reverse and forward scan direction of a device that was subjected to 108 min of max power point (mpp) tracking. (b) The max power point tracking data: The line plots show the smoothed PCE, V_{mpp} and J_{mpp} data, whereas the raw data is displayed as scatter plot behind. The device was masked with an aperture of 0.25 cm^2.

4.3 Discussion

4.3.1 Losses

Table 4.1: Comparison of device parameters in the detailed balance limit with the champion device.

	D.b. limit (2.00 eV[1])	Champion device (steady-state)
PCE [%] ($\%_{\mathrm{DB}}$)	22.62	12.13 (53.63)
J_{SC} [mA cm^{-2}] ($\%_{\mathrm{DB}}$)	14.59	11.66 (79.92)
V_{OC} [V] ($\%_{\mathrm{DB}}$)	1.683	1.373 (81.58)
FF [1] ($\%_{\mathrm{DB}}$)	0.922	0.758 (82.21)

We start our discussion by considering the gap between our best performing device and the theoretical limits given by detailed balance calculations. The respective values are listed in Table 4.1. The overall performance, the PCE, is only just above half of the theoretical potential of 22.62 %. The reason for this loss is quite equally distributed between the J_{SC}, V_{OC} and FF, all being close to 80 % of theoretical maximum, with J_{SC} the lowest at 79.92 % and FF the highest at 82.21 % of maximum.

Further, we look closer at the estimated contributions to the total V_{OC} loss. The contribution of each loss type has been summarized in Table 4.2. By taking the

difference between the V_{OC} in the detailed balance limit, $V_{\mathrm{OC,DB}}$, and the calculated $QFLS_{\mathrm{rad}}$ of the unsegregated absorber, we find unexplained radiative losses of 5 mV. This is, however, a very small fraction of the overall losses and could possibly be within the statistical variation of our data. Considering the PLQY values of the isolated perovskite films, we estimate the nonradiative losses in the bulk to be on the order of 212 mV – an entire 57.5 % of the overall V_{OC} loss. Further, we find that the interface with the p-contact adds another 17 mV on this and the n-contact interface adds another 76 mV. The latter value has been estimated by subtracting the 17 meV from the p-contact from the 93 meV difference between the $QFLS$ of the isolated perovskite film and the $qV_{\mathrm{OC,ss}}$ of the champion device. (As a side-note: The $V_{\mathrm{OC,ss}}$ of the champion device is only 1 mV different to the initial, unsegregated V_{OC} in Figure 4.5 (c).) The n-contact then contributes 20 % of the total V_{OC} losses, the second most important contribution. Lastly, the radiative losses due to halide segregation have been estimated from the measured V_{OC} during the light-soaking stages (blue lines in Figure 4.5 (c)), where the difference between the initial V_{OC} and the V_{OC} at the plateau is 59 mV – 16 % of the total V_{OC} loss and very close to the contribution from the n-contact. In total, we find that these losses sum up to 369 mV from the detailed balance limit – pretty much exactly the same as that of the device in Figure 4.5 (c) after segregation, but roughly 60 mV higher loss than that of the $V_{\mathrm{OC,ss}}$ of the champion. The estimations should therefore provide a fairly representative picture of the loss magnitude of one of our average devices.

Table 4.2: V_{OC} loss types in our 2 eV devices.

Loss type	Voltage [mV]	% of losses
Unexplained radiative losses	5	1.4
Nonradiative losses in bulk	212	57.5
Nonradiative losses due to p-type interface	17	4.6
Nonradiative losses due to n-type interface	76	20.6
Radiative losses due to halide segregation	59	16.0
Sum	369	

4.3.2 A Caveat on Reciprocity

In Figure 4.4 and Figure 4.5 we have tried to estimate the $QFLS_{\mathrm{rad}}$ and V_{OC} during halide segregation, akin to the procedure followed by Mahesh et al.[3] Given that we have the "solution manual" for the V_{OC} value in the realtime measured V_{OC} in Figure 4.5 (c) (blue), a discussion about the shortcomings of these estimations in our samples is warranted. The fact that the estimated V_{OC} (red diamonds drops far below the real V_{OC} (blue line) V_{OC} in Figure 4.5 (c) and that the estimated $QFLS_{\mathrm{rad}}$ after 21000 s reaches 1.27 eV – a value below the realtime qV_{OC} – is evidence that the models fall apart in some, if not all, of the experiment.

Considering Figure 4.5 (c), the initial negative discrepancy between the estimated value and the real V_{OC} value could possibly be attributed to smaller inaccuracies in the determination of EQE_{EL} and J_{SC}. The fact that the estimated V_{OC} does not detect the drop in V_{OC} immediately, could potentially be because the noise threshold in the EQE_{PV} measurements is too high to observe changes in the absorption profile at long wavelengths that could arise with halide segregation and affect the real $J_{0,\mathrm{rad}}$ and thus the real V_{OC}. So far, it thus seems possible that the estimations are valid but not accurate during the first 500 s. In the region of the experiment where the real V_{OC} has plateaued, applying another method implemented by Mahesh et al.[3] where the EQE_{EL} of the minority phase is allowed to differ from that of the majority phase in the model – and thus lead to a V_{OC} plateau at higher values – could rectify the estimation mismatch to a certain extent. However, as seen in Figure 4.5 (d), even this becomes insufficient to explain the mismatch as the radiative efficiency needed well exceeds 100%.

This therefore presses the issue of why the model breaks down. One reason could be that the requirement of optical reciprocity is not fulfilled. The fact that the calculated reciprocal emission shown in Figure 4.5 (f) does not seem to follow the same trend as, e.g. in Figure 4.5 (b), is an indication that this might be the case. However, the data is too limited to make this conclusion for two reasons: (i) The

halide segregation in Figure 4.5 (b) is not on the same timescale nor allowed to go to completion. It is possible that the tails of a large luminescence peak at low energies (long wavelengths) would overlap with the majority phase peak at 2.0 eV and cause this to exhibit an apparent red-shift similar to that seen in Figure 4.5 (f). (ii) Because of the high noise threshold in Figure 4.4 (b) we cannot discern any halide-segregated PL in the reciprocal emission calculated in in Figure 4.5 (f) and this makes it particularly difficult to make conclusions about the early stages of the experiment.

It is worth noting that the real V_{OC} reaches the plateau after 500 s (in Figure 4.5 (c)) and that during the same timescale, the change in estimated Urbach energy (Figure 4.4 (c)), $J_{0,\mathrm{rad}}$ (Figure 4.4 (d)), and bandgap (Figure 4.5 (e)) is relatively small, whereas in the remaining timeframe of the experiment, the real V_{OC} stays constant while the estimations of these parameters change significantly. This poses the question if maybe ordinary, reversible halide segregation completes in the first 500 s of the experiment, and what we observe after this are, rather, degradation effects. If this is the case, the question of validity of optical reciprocity would have to be treated separately for the two regimes.

4.3.3 Effect of Photoinduced Processes

We have thus far concluded that halide segregation has a negative effect on the V_{OC} on the order of 60 mV, but that the V_{OC} stays otherwise unaffected by any photoinduced processes occurring in the device (Figure 4.5 (c)). However, from the large changes seen in the absorption profile in Figure 4.4 (b) – also around the bandgap – and the large reduction in J_{mpp} and J_{SC} observed in Figure 4.6, it is clear that the most negatives effect are on the current density and not the voltage of the device.

It is not entirely clear from Figure 4.6 how much of the negative effect on J_{SC} is from conventional halide segregation and how much are from other degradation processes. Since this is at J_{mpp}, a lot fewer free carriers are present in the film at any given time compared to light-soaking at V_{OC}, and the halide segregation is therefore

expected to proceed at a slower rate. This makes direct comparison of timescales between the observations in both Figure 4.4 and Figure 4.5, and that of Figure 4.6 difficult. However, it is tempting to correlate the large drop in J_{mpp} over the first 1000 to 1500 s in Figure 4.6 (b) to the assumed halide segregation over the apparent halide-segregation timescale of 500 s in the previous observations. In this case, this would not be the only negative effect on J_{SC} during the MPP tracking, as also the unidentified degradation going on seems to mainly affect the J_{SC}, if this is what is occurring in the last 4000 s of the MPP tracking.

Datta et al.[4] performed PL measurements on full devices with regular JV-sweeps to correlate to device performance and found a strong reduction in J_{SC} that correlated with halide-segregated PL onset. They found the halide-segregation to occur much more slowly in a device than in isolated films, which they ascribe to the carrier quenching from their PCBM layer. Motti et al.[5] also found that halide-segregation could limit the diffusion length of free carriers because of the increased radiative recombination losses. In our case the perovskite film is only 200 nm thick, so the demands on diffusion length are not particularly high. Still, these findings resonate well with what we observe in this work.

4.4 Summary and Outlook

To summarize, we have investigated the different losses contributing to the suboptimal performance of our current 2 eV FAPb($Br_{0.7}I_{0.3}$)$_3$ perovskite solar cells. For our best performing devices, improvements need to be targeted towards all the 3 main parameters: FF, J_{SC} and V_{OC}, as they are all roughly 20 % below the detailed balance limit. We have identified that the clearly most dominant source of V_{OC} loss is nonradiative losses in the bulk perovskite itself, with quenching at the PCBM interface and halide segregation-induced losses second and third. Halide segregation itself appears to be harming J_{SC} much more than V_{OC}, and a critical hurdle towards long-term stability will be the limitation of J_{SC} losses under illumination.

We have tried to apply models based on optical reciprocity to estimate important parameters such as $J_{0,\mathrm{rad}}$, $QFLS_{\mathrm{rad}}$ and $V_{\mathrm{OC,rad}}$ during halide segregation. Comparison with the realtime V_{OC} show that our models do not make a decent estimation during parts of the halide segregation evolution but not all. It is not clear from our data if the increasing failure to estimate the V_{OC} and the associated values is due to the reciprocity relation not being valid at any point of the measurements or if it breaks down in the later stages due to e.g. irreversible degradation processes. An important future work will therefore be to acquire quality data with better atmosphere control, a larger dynamic range in EQE_{PV}, as well as EQE_{PV} in the above-gap region as function of time. This should be combined with quality EL data such as EQE_{EL} and EL spectrum as function of time at current densities similar to J_{SC} or J_{mpp}. In order to acquire this data, improvements will need to be made on the device fabrication. A lot of time was lost in the later stages of this project due to reproducibility issues in the device fabrication, leaving few samples to carry out important characterization measurements. It is not clear whether these reproducibility issues occurred over time due to changes in the fabrication conditions or were inherent to the developed process. Regardless, it serves as a good example of the importance of the development of sound and reproducible perovskite and device fabrication routes.

References

1. S. Rühle, "Tabulated values of the Shockley–Queisser limit for single junction solar cells," *Solar Energy*, vol. 130, pp. 139–147, 2016.
2. P. Caprioglio, M. Stolterfoht, C. M. Wolff, T. Unold, B. Rech, S. Albrecht, and D. Neher, "On the Relation between the Open-Circuit Voltage and Quasi-Fermi Level Splitting in Efficient Perovskite Solar Cells," *Advanced Energy Materials*, vol. 9, no. 33, p. 1901631, 2019.
3. S. Mahesh, J. M. Ball, R. D. J. Oliver, D. P. McMeekin, P. K. Nayak, M. B. Johnston, and H. J. Snaith, "Revealing the origin of voltage loss in mixed-halide perovskite solar cells," *Energy Environ. Sci.*, vol. 13, no. 1, pp. 258–267, 2020.
4. K. Datta, B. T. van Gorkom, Z. Chen, M. J. Dyson, T. P. A. van der Pol, S. C. J. Meskers, S. Tao, P. A. Bobbert, M. M. Wienk, and R. A. J. Janssen, "Effect of Light-Induced Halide Segregation on the Performance of Mixed-Halide Perovskite Solar Cells," *ACS Appl. Energy Mater.*, vol. 4, no. 7, pp. 6650–6658, 2021.
5. S. G. Motti, J. B. Patel, R. D. J. Oliver, H. J. Snaith, M. B. Johnston, and L. M. Herz, "Phase segregation in mixed-halide perovskites affects charge-carrier dynamics while preserving mobility," *Nat Commun*, vol. 12, no. 1, p. 6955, 2021.

CHAPTER 5

Halide Segregation and Degradation in 2 eV Perovskite Films

5.1 Introduction

In this chapter we investigate the evolution of photoluminescence during halide segregation in Cs-free, formamidinium-based 2 eV solar absorber thin-films. We devote particular interest to atmosphere-dependent developments in the PL spectrum during prolonged exposures (0.3 to 5 h) and shorter, cycled exposures over longer time scales (15 s light, 30 min dark, for $>$12 h). We find that exposure to atmospheric species, such as oxygen and humidty, promotes the domination of the PL spectrum by phases with PL peaks that are blue-shifted relative to the more frequently described red-shifted PL associated with halide segregation and that the reversion of these phases occur on different timescales. Using a combination of PL and XRD techniques, we attempt to identify the causes for the observed changes in the PL spectra.

Of the work presented in this chapter, work is credited as follows: Prof. Robert Taylor set up the instrument and facilitated the inert-atmosphere measurements and the associated reference in-air measurement, while the author performed the measurements; Vincent J.-Y. Lim performed the in-situ XRD-PL measurements in tandem with the author with Lim serving as the instrument expert and did the data processing and a preliminary data analysis, whereas the author did the final data analysis; the Python script used to control hardware in the cycled PL measurements was written by the author using parts from a different script written by Florine Rombach and Dr. Grey Christoforo; XRD peak identification was performed by the author in discussion with Dr. Harry Sansom and Dr. Joel Smith. All other experimental work and data analysis was performed solely by the author.

5.2 Results

5.2.1 Photoluminescence Observations in Neat-FA Perovskite Films

To learn more about the halide segregation tendencies in our material, we undertake various PL measurements on isolated films. In the following, we refer to samples as "pristine" when having a history of being stored in the dark in inert atmosphere, with no exposure to air. We explore the effects on the halide segregation from different storage and measurement atmospheres. In all of the following experiments, the samples were stored in the dark prior to measurement to ensure no initial halide segregation.

In Figure 5.1, the first 500 s of PL measurements on two pristine samples measured under 1 Sun equivalent intensity in nitrogen (a) and air (b), respectively, is displayed. The normalized contour plots show the evolution of the PL spectrum over time, while the intensity graphs display the evolution of the peak and integral intensity over the course of the same timeframe. (Note that the intensity graph is normalized to the highest peak or integral intensity of the entire experiment, whereof this plot

only displays the first 500 s.) In both atmospheres, we observe a relatively broad initial mixed-phase peak followed by the onset of a halide-segregated peak at 770 nm, which quickly red-shifts to 797 nm where it stabilizes. Kinetically, we note that the segregation appears quicker in the sample measured in air, where the mixed-phase peak is only dominant for less than 10 s, compared to roughly 30 s for the sample in nitrogen.

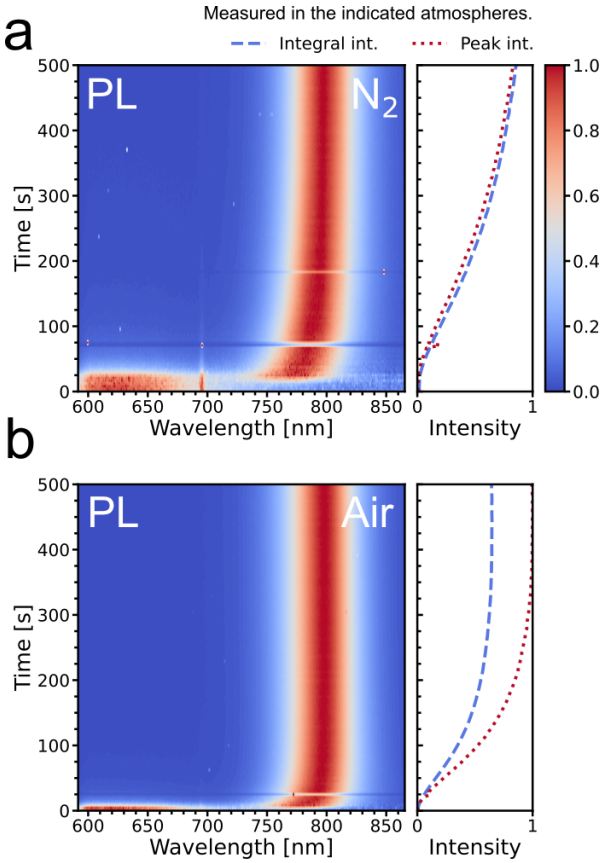

Figure 5.1: First 500 s of photoluminescence measurements at 1 Sun equivalent intensity with different measurement-atmosphere, as indicated in the plots: (a) in nitrogen; (b) in air. Samples were pristine prior to measurement. The contour plots show the normalized intensity at each time point, where an intensity of 1 indicates the highest intensity of the spectrum in that time point. The intensity graph shows the peak and integral intensity as function of time, with the intensity normalized to the highest peak or integral intensity over the course of the entire timescale of the experiment. The peak at 695 nm in (a) is a background fluorescence from the inert-atmosphere sample holder.

Moving past the first 500 s and looking at the entire timescale, Figure 5.2, we see the sample measured in air (b) reaches a maximum intensity around 500 s and then rapidly decays. The sample in nitrogen (a) similarly reaches a maximum early, but

only after 1300 s. The decay is also slower. The peak in (a) then blue-shifts slightly to 790 nm until it after 5000 s starts red-shifting slightly again towards 800 nm. The intensity remains low. The sample in air (b) displays a very different phenomenon. At 2000 s, after the rapid decay, the peak blue-shifts to 780 nm. Between 3000 and 5000 s the result is unclear because of data loss in this region. (Due to background lighting in the room hitting the detector.) After roughly 5500 s (white arrow), the peak position jumps to 750 nm due to the growth of a different, bluer-luminescent, more broad-peaked phase. In the remaining timeframe of the experiment, this broad luminescence red-shifts to 775 nm, where it stabilizes, while the intensity continuously increases until the integral intensity is higher than that from the initial halide-segregated luminescence after 500 s.

To further differentiate which aspect of the air exposure that causes the observed differences in halide segregation evolution, we trial different storage conditions prior to measurement. After fabrication, we let samples soak (in the dark) overnight in dry air atmosphere (desiccator cabinet; no humidity values available), ambient air (no humidity values available), and nitrogen for reference. The following PL measurements were carried out in an integrating sphere with air atmosphere, so to reduce the effect of the measurement atmosphere on the results, the measurements were accelerated by using an incident intensity of 4 Suns equivalent. The results are displayed in Figure 5.3 (a-c). First, we compare the pristine sample stored in nitrogen (a), with the measurements shown in Figure 5.2 (a-b). The progression is largely similar to that of Figure 5.2 (a), except there is no blue-shift occurring at any time in Figure 5.3 (a), rather, there is a continuous red-shift. At the peak intensity, the peak is at roughly 775 nm, whereas at the 1200 s mark, the peak is closer to 790 nm and the intensity is at it's lowest since the beginning. We note that we have performed many measurements in this rig and the wavelengths we observe both the mixed-phase and the most halide-segregated peaks at are usually consistent. We therefore attribute the fact that measurements in Figure 5.1 and Figure 5.2 tend to show wavelengths closer

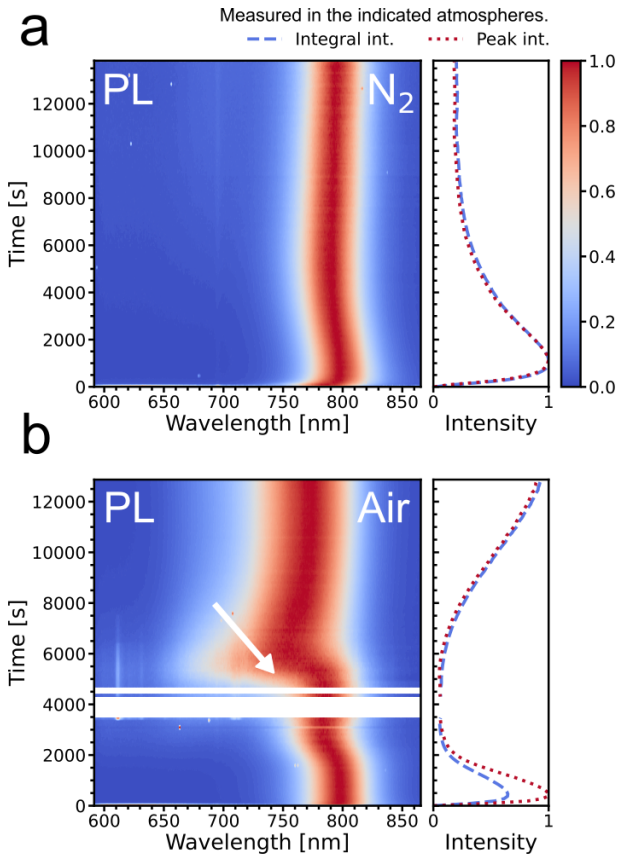

Figure 5.2: Photoluminescence measurements at 1 Sun equivalent intensity with different measurement-atmosphere, as indicated in the plots: (a) in nitrogen; (b) in air. Samples were pristine prior to measurement. The contour plots show the normalized intensity at each time point, where an intensity of 1 indicates the highest intensity of the spectrum in that time point. The intensity graph shows the peak and integral intensity as function of time, with the intensity normalized to the highest peak or integral intensity over the course of the entire timescale of the experiment. The peak at 695 nm in (a) is a background fluorescence from the inert-atmosphere sample holder. White regions in (b) are times where the data was polluted due to background room light hitting the detector.

to 800 nm to a lack of wavelength-dependent intensity calibration of the setup used in those measurements.

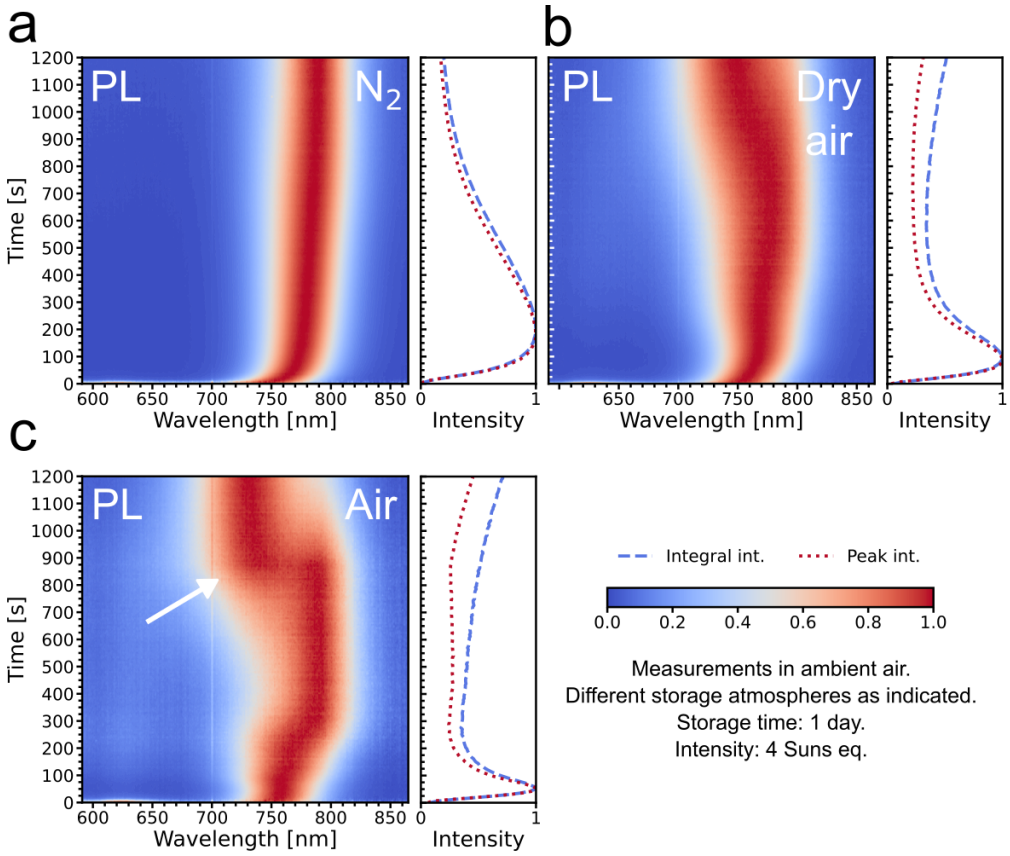

Figure 5.3: Photoluminescence measurements in air at 4 Suns equivalent intensity with different storage atmospheres (in the dark) for 1 night prior to measurement, as indicated in the plots: (a) in nitrogen; (b) in dry air; (c) in ambient air. The contour plots show the normalized intensity at each time point, where an intensity of 1 indicates the highest intensity of the spectrum in that time point. The intensity graph shows the peak and integral intensity as function of time, with the intensity normalized to the highest peak or integral intensity over the course of the entire timescale of the experiment.

In Figure 5.3 (c), the sample soaked in ambient air prior to measurement, the evolution is different. There is a very fast growth of a halide-segregated phase peaking before the first 100 s, with a peak position at 760 nm. This peak then redshifts to 790 nm while it decays. The integral intensity does, however, not decay as much as the peak intensity. This is because of a peak broadening and the gradual growth of a separate phase with a peak at 735 nm, which becomes the dominant PL source after 850 s (white arrow). The growth of this peak at 735 nm – at intermediate wavelengths

to the mixed phase PL and the initial segregated PL – is reminiscent of the dominant peak in Figure 5.2 (b) from 5500 s onwards. Considering Figure 5.3 (b), the sample soaked in dry air prior to measurement, the results are largely in between that of (a) and (c). The maximum intensity is reached sooner than (a) and later than (c), whereas the spectrum grows increasingly broadened, possibly due to the co-existence of multiple luminescing phases.

Taking it a step further, we do the same measurements, but this time on samples that soaked for 5 full days (again in the dark) in the respective atmospheres between fabrication and measurement, Figure 5.4 (a-c). Immediately apparent in Figure 5.4 (a) is that this sample looks practically identical to that of Figure 5.3 (a), thus 5 days in nitrogen in the dark has not made much difference. Figure 5.4 (b), the sample in the dry, displays early halide segregation at the previously observed wavelength around 775 nm, but then very early develops a broadening due to the growth a peak at 745 nm, which becomes dominant after 650 s. In this case, this intermediate phase PL peak arises before the more red-shifted peak has had time to decay, as apparent from the intensity graph. The starkest difference to the previously shown halide segregation evolutions comes from Figure 5.4 (c). After 5 days in ambient air in the dark, this sample no longer displays an early halide segregation in the very red-shifted part of the spectrum. Rather, a delayed-onset halide segregation at the intermediate wavelengths is visible that does not become dominant until 50 s into the measurement (white arrow). The peak wavelength is roughly 730 nm to begin with, while over the course of the measurement the intensity increases, the peak broadens and the peak wavelength redshifts gradually until it is around 750 nm after 1200 s.

To investigate the reversibility of these intermediate phases, we perform cycled photoluminescence measurements in ambient air with 15 s light-exposure and 30 min in the dark for recovery over a minimum of 28 cycles (~14 hours). We do this on both a pristine sample and a sample stored 5 days in the dark in ambient air. In Figure 5.5 (a-b), we show the integral intensity over different wavelength bands as function of cumulated light exposure. Each line corresponds to a cycle. The blue

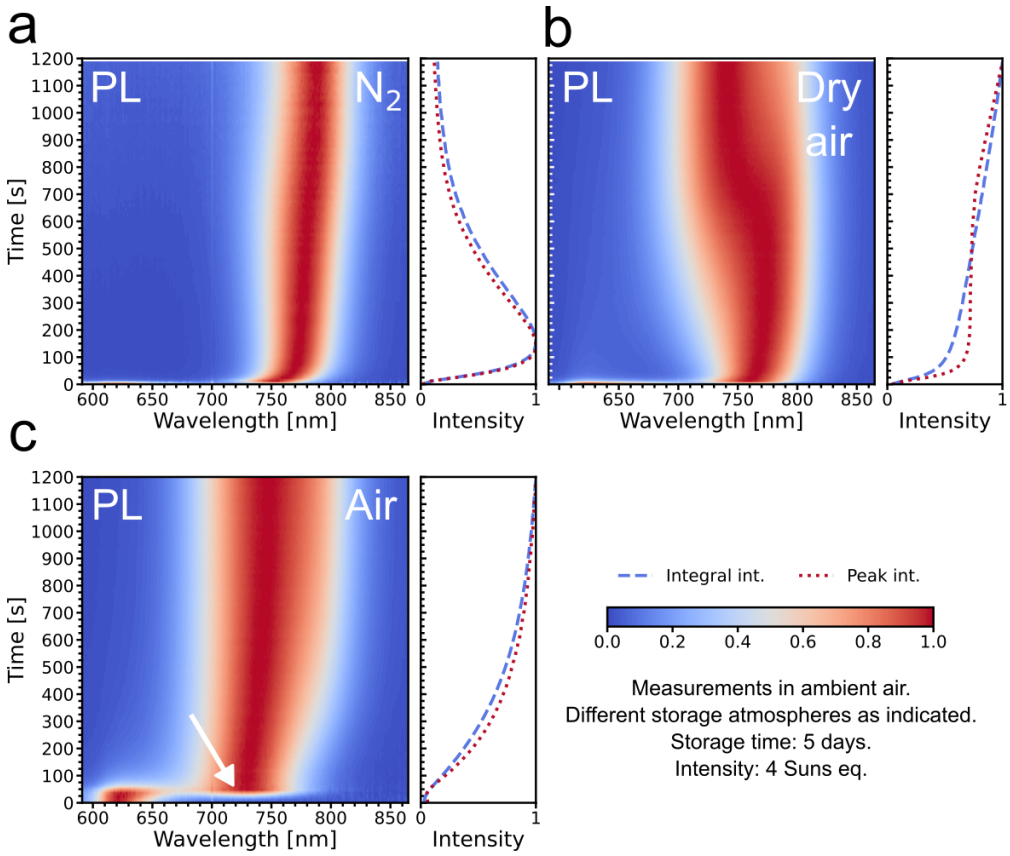

Figure 5.4: Photoluminescence measurements in air at 4 Suns equivalent intensity with different storage atmospheres (in the dark) for 5 days prior to measurement, as indicated in the plots: (a) in nitrogen; (b) in dry air; (c) in ambient air. The contour plots show the normalized intensity at each time point, where an intensity of 1 indicates the highest intensity of the spectrum in that time point. The intensity graph shows the peak and integral intensity as function of time, with the intensity normalized to the highest peak or integral intensity over the course of the entire timescale of the experiment.

band (580-660 nm, (i)) probes primarily the unsegregated majority phase, the grey and red bands (700-750 nm, (ii), and 750-800 nm, (iii)) are designed to probe the intermediate-wavelength and fully-segregated phases, respectively. However, because of the width of these peaks at full intensity, there will be some cross-talk across the integration bands.

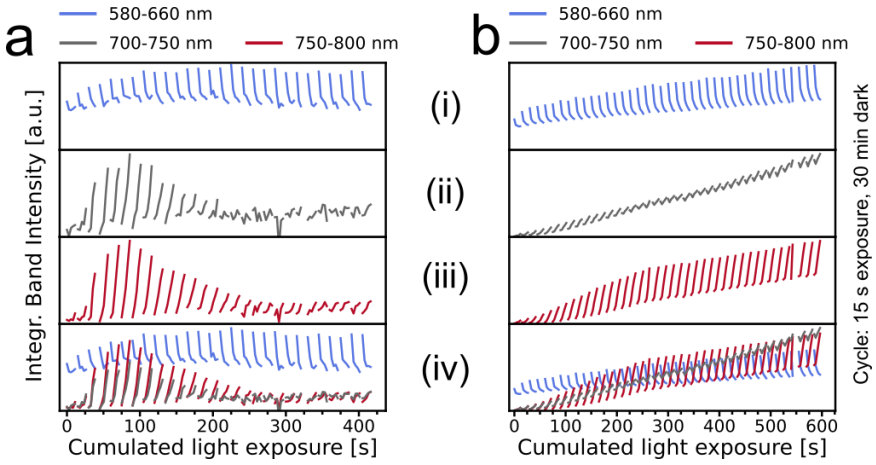

Figure 5.5: Cycled halide segregation of neat FA samples: The lines in each canvas (i)-(iv) represent the integral photoluminescence intensity as function of time as integrated over different wavelength bands (see legend). Each line represents the PL during one cycle. The samples were cycled with durations of 15 s incident light and 30 min in the dark. The x-axis displays the cumulated time under incident light. The canvasses (i)-(iii) display individual bands. In canvas (iv), the bands are overlapped for comparison of relative intensity. The sample in (a) is pristine, while the sample in (b) was measured after 5 days stored in the dark in ambient air.

Figure 5.5 (a) (i) displays the majority phase PL of the pristine film. We can see that the PL intensity drops in the beginning of each cycle to a baseline-like level. Over time, there is some brightening of the starting-PL, however, the baseline that the intensity decays to stays the same. In (ii) and (iii), we see a large brightening with each cycle in the beginning, but the halides seem to be segregating completely during each dark phase. The brightening then decays completely again until the luminescence of the halide-segregated phase(s) is almost non-existent and is close to the noise floor. Looking at (iv), it seems the intensity observed in the intermediate band, (ii), is likely cross-talk from the fully-segregated PL at close to 800 nm. It is noteworthy that the halide-segregated PL sees a large brightening and de-brightening whereas the majority phase sees only a brightening.

We now observe the sample stored for 5 days in ambient air prior to measurement, Figure 5.5 (b). The majority phase PL, (i), looks largely similar, except the baseline that it decays towards on each cycle now seems to undergo a continuous, slight increase. Judging from the other bands, this increase could be due to cross-talk from segregated-phase PL. Considering panel (iii), the longest-wavelength band has two distinct phases: in the first 2/5 of the experiment, the intracycle intensity-rise increases for each cycle, while at the same time the reversion in the dark does not seem to complete entirely and the baseline increases. From approximately 250 s of cumulated light exposure, the intracycle intensity-rise stays constant and the baseline-increase now takes a less steep slope for the remainder of the experiment. The intermediate-PL band, (ii), shows a slightly different trend. The intracycle intensity-change is very little and often shows a drop-then-rise which bears witness of cross-talk from both the majority-phase PL decay and the long-wavelength PL rise. However, the baseline intensity rises linearly for the duration of the measurement, suggesting that there may be luminescent phases in this wavelength-region that do not nearly decay properly during the 30 min in the dark between each cycle. Looking at Figure 5.5 (b) (iv), at the 600 s mark, this integration band shows the highest intensity.

It is clear that the exposure to oxygen and humidity both impacts the evolution of the halide segregation, as manifested by the changes seen in the PL above. To further our understanding of what might be occurring in the material during this time, we perform in-situ X-ray diffraction (XRD) measurements on the $\{200\}$ perovskite peak while illuminating the samples at a 1.3 Suns intensity. In this case, measurements are performed in air, with samples that had soaked in the dark in nitrogen and ambient air, respectively, for 5 days. We show the first 1000 s in Figure 5.6 and the full measurements in Figure 5.7. Again, comparing the PL in Figure 5.6 (a) and (b), we see that the sample soaked in ambient air has a delay before any halide-segregated phase becomes dominant, and that once the halide-segregated PL becomes dominant it is with a peak position that is much bluer than what is the case for the pristine sample stored in nitrogen. There does, however, appear to be a presence of the more

red-shifted PL early on (visible in white gradient around 750 nm between 50 and 150 s, Figure 5.6 (b)), but this quickly gets overpowered. The halide segregation in the pristine sample reaches an early maximum at 100 s before it decays down to the level of the mixed-phase PL again after 1000 s (Figure 5.6 (a)). In both samples, the {200} XRD peak starts relatively sharp with a peak position close to 29.3° 2θ.

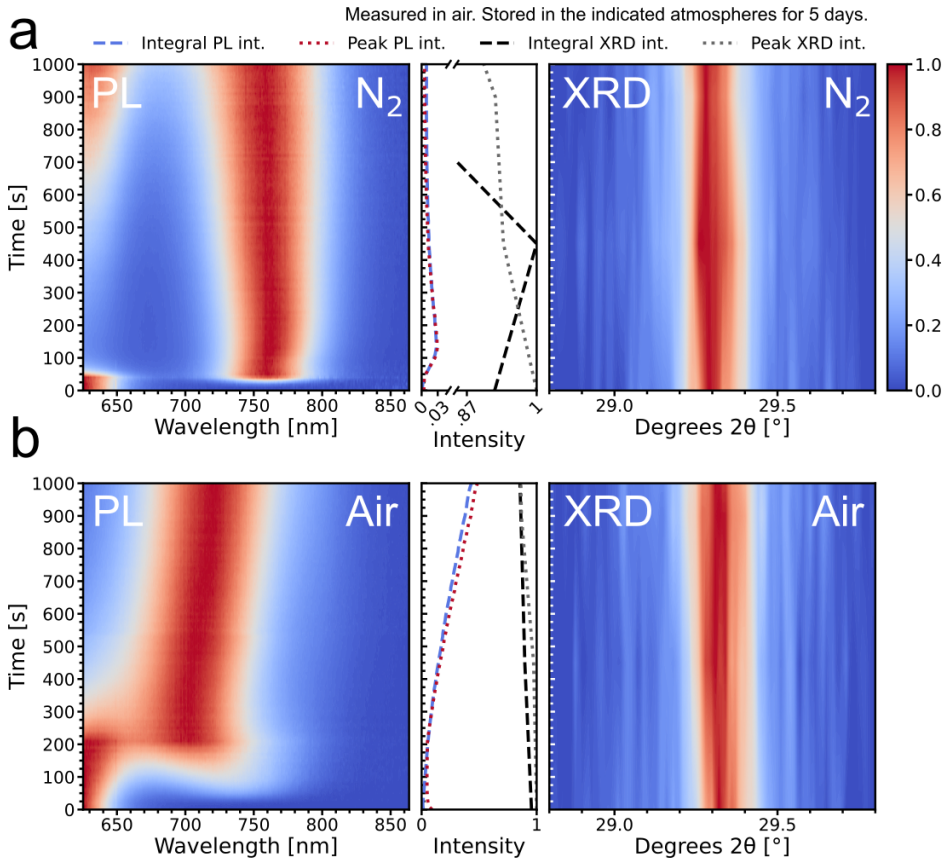

Figure 5.6: First 1000 s of in-situ X-ray diffraction and photoluminescence measurements in air at 1.3 Suns equivalent intensity with different storage atmospheres (in the dark) for 5 days prior to measurement, as indicated in the plots: (a) in nitrogen; (b) in ambient air. The contour plots show the normalized intensity at each time point, where an intensity of 1 indicates the highest intensity of the spectrum in that time point. The intensity graph shows the peak and integral intensity (of both PL and XRD) as function of time, with the intensity normalized to the highest peak or integral intensity over the course of the entire timescale of the experiment.

Considering the full measurements, we see in Figure 5.7 (a) that after around 1000 to 2000 s measurement in air, the pristine sample also develops an intermediate phase PL peak which red-shifts to 770 nm during the measurement and reaches an intensity that dwarves the intensity of the first maximum (which is only visible in Figure 5.6

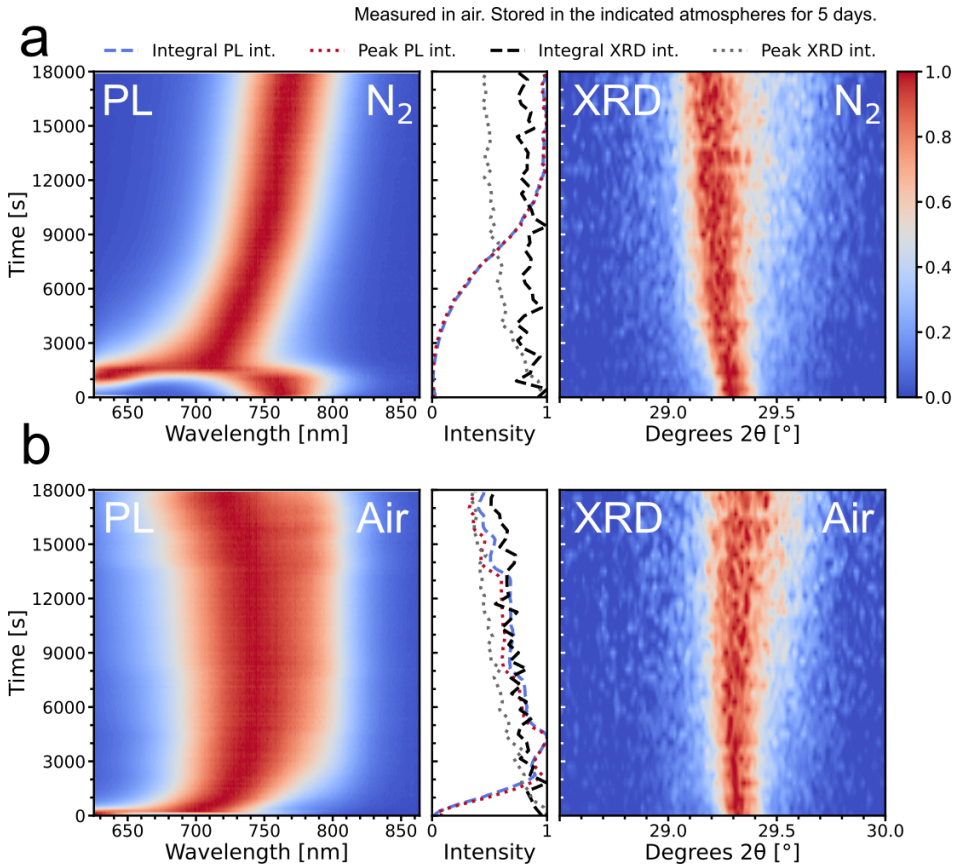

Figure 5.7: In-situ X-ray diffraction and photoluminescence measurements in air at 1.3 Suns equivalent intensity with different storage atmospheres (in the dark) for 5 days prior to measurement, as indicated in the plots: (a) in nitrogen; (b) in ambient air. The contour plots show the normalized intensity at each time point, where an intensity of 1 indicates the highest intensity of the spectrum in that time point. The intensity graph shows the peak and integral intensity (of both PL and XRD) as function of time, with the intensity normalized to the highest peak or integral intensity over the course of the entire timescale of the experiment.

(a)). In Figure 5.7 (b), the intermediate phase PL redshifts and stabilizes its peak position around 745 nm with a very broad spectrum. The peak position stays stable for over 10000 s before there is a blue-shift in the last 4000 s of the measurement. The {200} XRD peaks evolves somewhat differently between the two samples. In Figure 5.7 (a), the peak position shifts towards lower angles, ending around 29.2 ° . At the same time, there is a visible broadening, manifested both by the appearance of a larger region of white at higher angles in the contour plot (notably the broadening is not symmetric around the peak) and by a larger reduction in peak XRD intensity than integral XRD intensity in the intensity graph. Also Figure 5.7 (b) displays a reduction of integral and peak XRD intensity, indicative of a reduction of crystallinity. The reduction in integral intensity is larger in (b), nearly 50 %, than in (a), which is closer to 25 % over the course of the measurement (but with a large uncertainty due to noise in the measurement). The sample that was stored in air (b) does not exhibit a clear shift in peak position during the measurement. There appears to be a slight shift to lower angles in the first half of the measurement followed by a slight shift back in the last half. The peak is very broadened over the course of the measurement and the broadening appears more symmetric in this case, but also here with a slightly stronger tail at higher angles.

5.2.2 X-ray Diffraction Observations in Neat-FA Perovskite Films

To explore the changes in the crystalline nature of the films over a longer timescale, we light-soak a film at 1 Sun equivalent intensity in ambient air at room temperature for 3 weeks and measure the XRD at logarithmic intervals. In Figure 5.8 (a) we show the contour plot of the normalized diffractogram around the cubic perovskite {200} peak. In the beginning, the {200} peak is centred at approximately 29.5° 2θ. Over the first 50 min the peak centre seems to shift slightly towards 29.3° before it broadens strongly between the 50 and 200 min mark. The broadening continues up

until the measurement at 1260 min (21 h), after which the signal narrows again into a discrete peak at close to 29.8° in the 2800 min measurement (46 h). It should be noted that during the broadened phase, the peak centre meanders from 29.3°, down to almost 29.0°, and up to 29.6°, before reaching the discrete peak at 29.8°. Over the remaining time up to the final measurement after 28500 min (475 h), the peak remains relatively stable in both position, intensity and width, except perhaps for a very slight shift towards higher angles. The integral XRD intensity falls more or less continuously throughout the experiment. We fit the full diffractogram with a Pawley fit using Topas Academic. In this method, constraints based on the symmetry and size of the unit cell is used to fit the peaks at the expected 2θ values. This results in a lattice parameter of the cubic perovskite phase that is 6.095 Å at the beginning of the experiment. At the end, the lattice parameter comes out as 5.994 Å. We remark that the lattice parameter of $FAPbBr_3$ is reported in literature to be 5.992 Å.[1]

In Figure 5.8 (b) we show photos of the film at most timepoints. The film remains red for the first 1260 min, despite the wide broadening happening during this time. When the $FAPbBr_3$-like diffraction peak has arisen after 2800 min, the sample has turned mostly orange-yellow. Over the remaining time of the experiment the film gradually turns more yellow, and eventually yellow with a green tint.

We plot full diffractograms from 0, 3.3 and 210 h (0, 200 and 12600 min) in Figure 5.8 (c). We have identified all peaks to either belong to the cubic perovskite phase (not indicated) or the phases indicated by a diamond, circle or triangle in the figure. The cubic perovskite peaks can be seen to broaden (grey, 3.3 h) and then arise sharp again at higher angles (red, 210 h). The PbI_2 observed in the beginning disappears over the course of the measurement, while a new phase, Pb(OH)Br appears. In Figure 5.8 (d) we plot the normalized integral XRD intensity of the {100} peak from the same sample (red) and from two similar samples stored under different conditions: in the dark in ambient air (blue) and in the dark in nitrogen (grey). As expected, the intensity of the {100} peak in the sun drops off similarly to what is observed for the {200} peak in (a). The most notable aspect is a large drop in intensity between 21 and

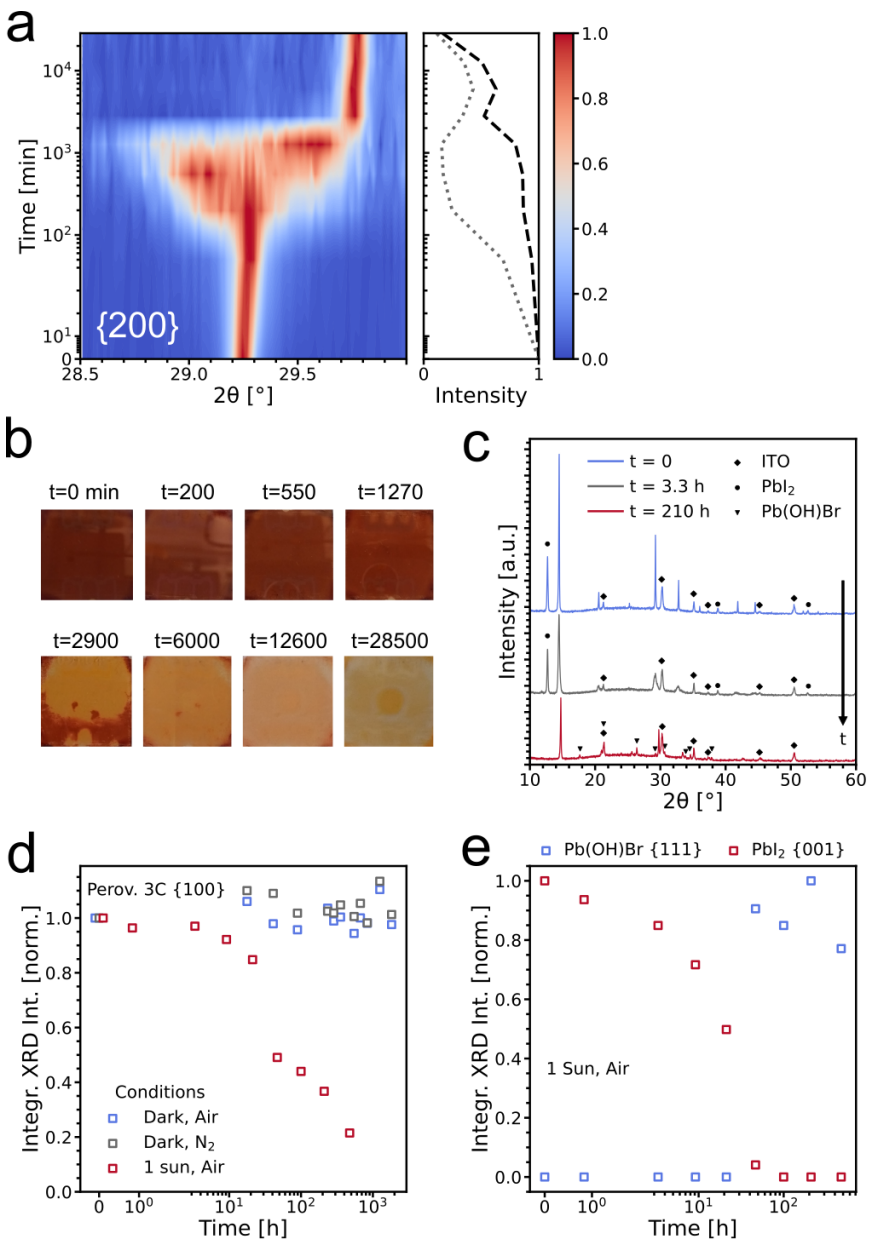

Figure 5.8: (a) X-ray diffraction intensity as function of time for a film light-soaked in air at room temperature under 1 Sun equivalent intensity. The contour plots show the normalized intensity at each time point, where an intensity of 1 indicates the highest intensity of the diffractogram in that time point. The intensity graph shows the peak and integral intensity as function of time, with the intensity normalized to the highest peak or integral intensity over the course of the entire timescale of the experiment. (b) Photographs of the same sample at different times (in minutes) throughout the experiment. (c) X-ray diffractograms at 3 different times for the same sample. Peaks identified as belonging to the ITO substrate, PbI_2 and Pb(OH)Br are identified with symbols. All other recognizable peaks have been identified to belong the 3C perovskite phase. (d) Integral XRD intensity of the 3C perovskite {100} peak in 3 films aged in different conditions. The red sample is the same as in (a-c). The blue sample was aged at room temperature in the dark in ambient air, and the grey sample was aged at room temperature in the dark in a nitrogen-filled glovebox. The intensities have been normalized to the starting value. (e) Integral XRD intensity of the two most dominant peaks of two impurity phases in the same sample as (a-c). The PbI_2 intensity has been normalized to the starting value. The Pb(OH)Br intensity has been normalized to its maximum value.

46 h (1260 and 2800 min). The samples kept in the dark, on the other hand, remain approximately constant for the 76 days the experiment was kept running. We also plot the normalized intensities of the strongest PbI_2 and Pb(OH)Br peaks in Figure 5.8 (e). PbI_2 is almost disappeared after 2800 min and completely disappeared for the rest of the experiment, whereas Pb(OH)Br oppositely is appearing after 2800 min and then remains roughly constant.

5.2.3 Photoluminescence Observations in FACs Perovskite Films

To see if similar behaviour to what we have observed in our $FAPb(Br_{0.7}I_{0.3})_3$ material is visible in a more typical FA-Cs cation mix, we perform a couple of experiments on $FA_{0.83}Cs_{0.17}Pb(Br_{0.7}I_{0.3})_3$ (henceforth referred to as "FACs"). In Figure 5.9 we display the contour plot of a pristine FACs film measured in ambient air under 1 Sun intensity. Similar to the neat-FA material, we see an initial rise in brightness at the onset of halide segregation, followed by a PL decay and then a long, continuous brightening. The wavelength, however, stays constant with a peak at approximately 770 nm. We note that the majority phase is less bright in these films than in their neat-FA counterparts, and we see absolutely no PL in the beginning of this measurement. We also perform the cycled photoluminescence measurements on FACs films. Like for the neat-FA version, we perform these on both a pristine film and a film stored 5 days in ambient air in the dark, Figure 5.10 (a-b). In (a), the pristine film is extremely dim throughout the experiment, with the integrated band intensity hovering around the noise floor for all bands. The sample stored in ambient air, (b), is much brighter. The majority phase band (blue, (i)) is visible from the beginning but increases its baseline brightness throughout, first relatively steeply and then at a lower slope. The fully halide-segregated luminescence (band (iii), red) is not visible in the beginning but becomes gradually brighter throughout. The reversibility of this band in the dark seems to be complete for pretty much every cycle. The grey intermediate-wavelength

band, (ii), follows a very similar pattern to (iii), except from after 450 s this band shows an incomplete reversion in the dark. This suggests that also FACs can exhibit similar intermediate-wavelength halide-segregated PL phases.

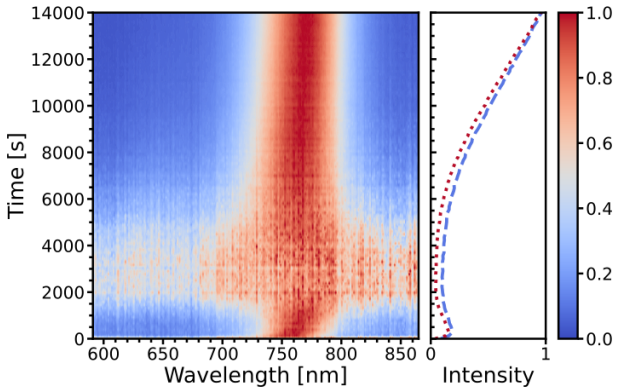

Figure 5.9: Photoluminescence measurements of a $FA_{0.83}Cs_{0.17}Pb(Br_{0.7}I_{0.3})_3$ film at 1 Sun equivalent intensity in ambient air. The sample was pristine prior to measurement. The contour plots show the normalized intensity at each time point, where an intensity of 1 indicates the highest intensity of the spectrum in that time point. The intensity graph shows the peak and integral intensity as function of time, with the intensity normalized to the highest peak or integral intensity over the course of the entire timescale of the experiment.

5.3 Discussion

5.3.1 Trends in Photoluminescence Brightness

Considering all the PL investigations on perovskite films presented in Figures 5.1 to 5.7, three typical stages of the PL intensity evolution are clear: First, an initial quick rise in brightness associated with the growth of the first halide segregated phase, with typically all the PL coming from very red-shifted domains. Second, a (slower) decay of the PL. Third, a long, continuous brightening typically extending longer than the duration of our measurements, and in samples pre-stored in dry or ambient air often occurring so early that the decay-phase is overshadowed.

Figure 5.5 (a) (i) shows an increase in the brightness of the halide-segregated phase over the first 100 s of cumulated light exposure (first 120 min of air-exposure, due to the 30 min dark-time between light exposures). This is likely due to oxygen-passivation.

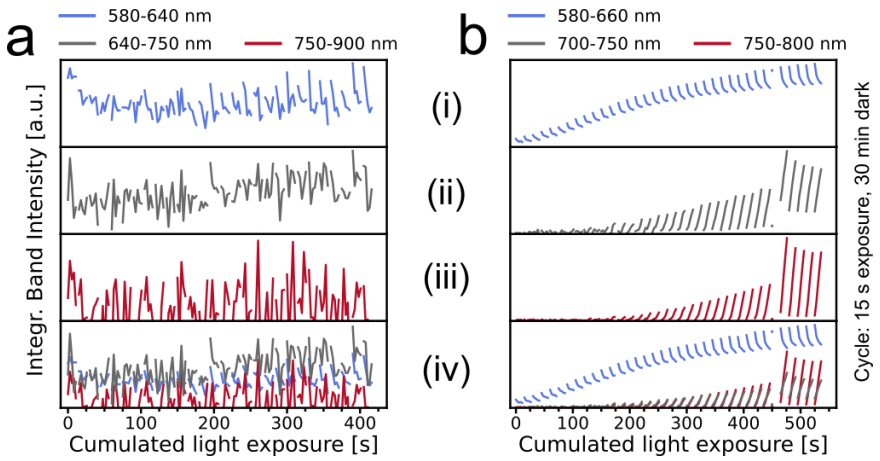

Figure 5.10: Cycled halide segregation of $FA_{0.83}Cs_{0.17}Pb(Br_{0.7}I_{0.3})_3$ samples: The lines in each canvas (i)-(iv) represent the integral photoluminescence intensity as function of time as integrated over different wavelength bands (see legend). Each line represents the PL during one cycle. The samples were cycled with durations of 15 s incident light and 30 min in the dark. The x-axis displays the cumulated time under incident light. The canvasses (i)-(iii) display individual bands. In canvas (iv), the bands are overlapped for comparison of relative intensity. The sample in (a) is pristine, while the sample in (b) was measured after 5 days stored in the dark in ambient air.

It has been shown that superoxide (O_2^-) species can occupy iodide vacancies and lead to a passivation of the defect state associated with the vacancy, in addition to p-doping of the perovskite, which can facilitate an increased radiative efficiency.[2] It has also been shown that oxygen can diffuse into and fully saturate a $MAPbI_3$ film in 5 to 10 min.[3]

The following decay is evidence there must be competing processes ongoing. One such process could be the photoluminescence intensity decrease described by Motti et al.,[4] where neutral, interstitial iodides may form I_2 and preferentially stabilize at uncoordinated Pb sites at grain boundaries or surfaces. It should be noted that the decay we see seems to occur earlier when the sample is pre-soaked with oxygen (dry-air), and even sooner when humidity is also present, Figure 5.3 (a-c), but it is not clear how this would contribute to accelerate this process. Another thing to note is that for the initial (majority phase) PL we often see higher intensities for samples that have been exposed to oxygen prior to measurement compared to pristine samples, whereas the intensity maximum of the first halide-segregated peak is often more intense in the samples that were pristine compared to samples that were pre-oxygen-soaked. This

suggests that some oxygen is good for radiativity but also that it may fuel negative processes which could be working over longer timescales.

The role of oxygen and humidity is complicated more by the fact that it seems directly related to the third stage: the long, continuous brightening. This stage is also characterized by a lot of peak broadening and strong luminescence from shorter wavelengths than the typical initial red-shifted halide segregation PL. This suggests that more domains (of differing halide ratios and/or quantum confinements) are present during this stage, which could mean that a larger volume of the film may consist of phases with increased radiative efficiency. It is in itself interesting that with the presence of such a variety of phases, most carriers no longer seem to funnel down to the most iodide-rich domains (if still present) – this we will further discuss later in this section.

5.3.2 Crystalline Changes

From Figure 5.8 we know that when exposed to light and ambient air in the long-term, our films exhibit a wide broadening of the perovskite XRD signal that would be consistent with the presence of a wide phase distribution of differing halide ratios. Further, this broadening ceases and a $FAPbBr_3$-like peak appears at the same time as evidence of crystalline PbI_2 disappears and peaks associated with Pb(OH)Br appears. This strongly suggest that our films undergo a loss of iodide and become iodide-depleted. The iodide in PbI_2 may be depleting by similar mechanisms to the depletion of iodide in the perovskite, or may be serving as an iodide-buffer that provides iodide to the perovskite in an equilibrium reaction until there is no more PbI_2 left to backfill the perovskite. In either case, Pb(OH)Br with its 1:1 Pb:Br ratio is a Pb-rich phase compared to $FAPbBr_3$ and may be serving to bind up some of the excess Pb^{2+} after the halide-loss from the perovskite phase and the PbI_2. Aristidou et al. found that superoxides could facilitate the photoinduced degradation of $MAPbI_3$ perovskite films into I_2 and other species through the reaction:

$$4\,CH_3NH_3PbI_3^* + O^{2-} \longrightarrow 4\,PbI_2 + 2\,I_2 + 2\,H_2O + 4\,CH_3NH_2, \qquad (5.1)$$

where $4\,CH_3NH_3PbI_3^*$ is photoexcited $MAPbI_3$. Our neat-FA material could potentially be undergoing the same process.

5.3.3 Intermediate-wavelength PL Phases

We have seen that under illumination in the presence of ambient air, the PL spectrum is eventually not dominated by a very red-shifted, halide-segregated PL, but rather luminescing phases with wavelength intermediate to that of the majority phase and the most red-shifted PL observed. These intermediate-wavelength phases appear to be present earlier when the sample has soaked in ambient atmosphere in the dark prior to measurements. The observations from XRD suggest that the luminescence at shorter wavelengths at least partially may be attributed to a depletion of iodide and thus a higher bromide-to-iodide ratio.

A higher bromide-to-iodide ratio does, however, not explain why the luminescence occurs from such a wide distribution of wavelengths or why the intensity increases so much during this stage. The broad luminescence implies that excited charge carriers are not able to funnel into the lowest-bandgap phases before they recombine, or that this is not energetically beneficial. This then suggests that there may be barriers to carrier transport between luminescent phases. Such barriers could be, for example, the interspersed formation of other phases with reduced carrier transport properties. This could, for example, be Pb(OH)Br formation along grain boundaries. Pb(OH)Br is not suspected to be the source of any of the observed PL itself. In the literature it is reported with a calculated bandgap of 3.1 eV ($\approx$400 nm),[5] and in terms of optical activity it has been described as not detectable for Pb(OH)Br nanowires[6] or with a PL at 489 nm for Pb(OH)Br microdisks.[7] However, Liu et al. reports Pb(OH)Br to provide efficient and stable passivation of $MAPbBr_3$ quantum dots, improving both PLQY and long-term stability.[5]

One of the contributors to the stage 3 continuous intensity increase could therefore be passivation of defect states by Pb(OH)Br, increasing the radiative yield of the remaining perovskite phases. Another contributor to the increased PL may be the luminescence enhancement described by Motti et al.[4], where interstitial iodide may recombine with iodide vacancies and lead to increased radiative efficiency, which is only expected to be seen when only short-range ion migration is possible, i.e. it requires some kind of confinement effects to be taking place, such as the intergranular Pb(OH)Br growth described in the previous paragraph. As a caveat to all of this: we do not observe crystalline Pb(OH)Br until after 2 full days of light-soaking, so this discussion presumes that some formation of amorphous Pb(OH)Br or trace amounts of crystalline Pb(OH)Br occurs before this timepoint and is sufficient to cause the observed effects on PL.

5.3.4 Processes in the Presence of Cs or Absence of Air

Our combined data in Figure 5.9 and Figure 5.10 suggest that these processes are also present in FACs samples, but with a strong suppression of the kinetics. Stabilization of, or suppressed, halide-segregation kinetics in multi-cation samples has been observed by other researchers.[8] It is not possible from the timescale of our data in Figure 5.2 to conclude whether the complete absence of oxygen and humidity prevents the described processes or just strongly suppresses the kinetics. Much longer experiments would be needed to confirm this.

5.4 Summary and Outlook

We have observed that our 2 eV $FAPb(Br_{0.7}I_{0.3})_3$ materials not only exhibit a very red-shifted, halide-segregated PL peak, but over time also develops broad PL from wavelengths intermediate to that of the unsegregated majority phase and the typical halide-segregated phase. These intermediate-wavelength PL phases become dominant over time and grow very bright. The presence of oxygen accelerates the developments

considerably, and the presence of oxygen and humidity even more. The presence of oxygen and/or humidity may or may not be essential to facilitate these phases. We have also observed that the films over time in ambient air suffer photoinduced degradation leading to iodide loss and the formation of a nearly iodide-free perovskite phase. Simultaneously, we observe formation of Pb(OH)Br. We hypothesize that the Pb(OH)Br could be forming as an excess-Pb sink after the iodide-loss and may be preferentially forming along grain boundaries where it could serve to passivate the perovskite material and possibly be a reason for the increased luminescence intensity seen from intermediate-wavelength PL phases. The depletion of iodide is also assumed to be one of the reasons for the presence of intermediate-wavelength PL phases.

To obtain a higher degree of certainty in the mechanisms governing these observations, additional experiments are required. Experiments carried out in flushed nitrogen atmosphere over very prolonged times would be beneficial to determine if intermediate-wavelengths also can occur without oxygen or humidity. Similarly, experiments in flushed oxygen atmosphere with no humidity could illuminate the role of humidity. E.g. Pb(OH)Br would be less expected to form in such an environment. Combining XRD measurements with PL and SEM investigations of light-soaked films as function of time would also shed light on the role of Pb(OH)Br and degradation processes in the optoelectronic qualities of the film.

References

1. F. C. Hanusch, E. Wiesenmayer, E. Mankel, A. Binek, P. Angloher, C. Fraunhofer, N. Giesbrecht, J. M. Feckl, W. Jaegermann, D. Johrendt, T. Bein, and P. Docampo, "Efficient Planar Heterojunction Perovskite Solar Cells Based on Formamidinium Lead Bromide," *J. Phys. Chem. Lett.*, vol. 5, no. 16, pp. 2791–2795, 2014.

2. A. Szemjonov, K. Galkowski, M. Anaya, Z. Andaji-Garmaroudi, T. K. Baikie, S. Mackowski, I. D. Baikie, S. D. Stranks, and M. S. Islam, "Impact of Oxygen on the Electronic Structure of Triple-Cation Halide Perovskites," *ACS Materials Lett.*, vol. 1, no. 5, pp. 506–510, 2019.

3. N. Aristidou, C. Eames, I. Sanchez-Molina, X. Bu, J. Kosco, M. S. Islam, and S. A. Haque, "Fast oxygen diffusion and iodide defects mediate oxygen-induced degradation of perovskite solar cells," *Nat Commun*, vol. 8, no. 1, p. 15218, 2017.

4. S. G. Motti, D. Meggiolaro, A. J. Barker, E. Mosconi, C. A. R. Perini, J. M. Ball, M. Gandini, M. Kim, F. De Angelis, and A. Petrozza, "Controlling competing photochemical reactions stabilizes perovskite solar cells," *Nat. Photonics*, vol. 13, no. 8, pp. 532–539, 2019.

5. K.-K. Liu, Q. Liu, D.-W. Yang, Y.-C. Liang, L.-Z. Sui, J.-Y. Wei, G.-W. Xue, W.-B. Zhao, X.-Y. Wu, L. Dong, and C.-X. Shan, "Water-induced MAPbBr3@PbBr(OH) with enhanced luminescence and stability," *Light Sci Appl*, vol. 9, no. 1, p. 44, 2020.

6. W. Wang, Y. Yu, S. Attique, J. Hou, F. Jun, Y. Xie, L. Mao, X. Yu, X. Zhang, S. Wang, C. Wu, B. Cao, and S. Yang, "Sustainable fabrication of ultralong Pb(OH)Br nanowires and their conversion to luminescent CH3NH3PbBr3 nanowires," *Green Chem.*, vol. 23, no. 20, pp. 7956–7962, 2021.

7. G. Wan, G. Wang, Y. Feng, and W. Yu, "Synthesis and optical properties of elliptic Pb(OH)Br microdiskettes," *Materials Research Bulletin*, vol. 46, no. 4, pp. 487–491, 2011.

8. K. Datta, B. T. van Gorkom, Z. Chen, M. J. Dyson, T. P. A. van der Pol, S. C. J. Meskers, S. Tao, P. A. Bobbert, M. M. Wienk, and R. A. J. Janssen, "Effect of Light-Induced Halide Segregation on the Performance of Mixed-Halide Perovskite Solar Cells," *ACS Appl. Energy Mater.*, vol. 4, no. 7, pp. 6650–6658, 2021.

CHAPTER 6

Reducing Nonradiative Losses in Perovskite LEDs Through Atomic Layer Deposition of Al_2O_3 on the Hole-injection Contact

6.1 Introduction

In this chapter we work on optimization of the p-contact in p-i-n, green, halide perovskite LEDs and succesfully employ an organic-inorganic composite p-contact layer by using atomic layer deposition to intergrow Al_2O_3 with the organic hole-selective polymer TFB. This way, we achieve an improved EQE_{EL} from our LEDs which we reason stem from an inhibition of nonradiative recombination pathways where perovskite–ITO contact would allow injected electrons to escape the emitter without radiatively recombining with the injected holes.

The work in this chapter is adapted from the publication: Emil G. Dyrvik, Jonathan H. Warby, Melissa M. McCarthy, Alexandra J. Ramadan, Karl-Augustin Zaininger,

Andreas E. Lauritzen, Suhas Mahesh, Robert A. Taylor, and Henry J. Snaith, "Reducing Nonradiative Losses in Perovskite LEDs through Atomic Layer Deposition of Al2O3 on the Hole-Injection Contact" *ACS Nano,* vol. 17, pp. 3289-3300, Feb. 2023, DOI: 10.1021/acsnano.2c04786

Of the work presented in this chapter, work is credited as follows: Dr. Andreas E. Lauritzen performed the XRR measurements and analysis; Dr. Alexandra J. Ramadan performed the AFM measurements and analysis; the author performed the majority of the ellipsometry measurements and analysis, with some contributions from Dr. Suhas Mahesh; the author and Dr. Karl-Augustin Zaininger performed the ALD-step of the sample fabrication; Dr. Melissa M. McCarthy and Dr. Karl-Augustin Zaininger were responsible for the good functional state of the ALD instrument; the idea was conceived by the author and Dr. Jonathan H. Warby; the project was supervised by Dr. Warby, Prof. Robert A. Taylor, and Prof. Henry J. Snaith; all authors contributed to the discussion and writing of the manuscript; all other experimental work and data analysis was performed by the author.

6.2 Background

Halide perovskite semiconductors have attracted enormous interest from the scientific community and industry over the last decade. A large variety of applications for this group of materials are being explored, including photovoltaic cells,[1] radiation detectors,[2] light-emitting diodes (LEDs),[3] lasers[4] and photodetectors.[5] Halide perovskites are interesting for LED applications, since they have highly efficient, tunable emission, with narrow emission spectrum, and could feasibly out-perform organic LEDs (OLEDs) in terms of absolute efficiency, due to the process of photon-recycling.[6–9] Since the report of the first room-temperature halide perovskite light-emitting diode (PeLED) in 2014,[3] both publication numbers and efficiencies have soared. External quantum efficiencies of electroluminescence (EQE_{EL}) above 20 % have been reported by multiple groups since 2018.[10–13] The rapid rise in efficiencies has been achieved

through numerous improvements in design and fabrication, such as carrier confinement in the emitter,[14–16] defect passivation strategies,[17–19] improved carrier injection and transport,[20–22] and thermal management strategies.[20,23]

PeLED devices are typically designed in both positive-intrinsic-negative (p-i-n) or negative-intrinsic-positive (n-i-p) heterostructure architectures with the emissive perovskite layer sandwiched between a hole transport layer (HTL) and an electron transport layer (ETL). An important property of the charge transport layer (CTL), and the contact that it forms in the device, is its "selectivity" for one carrier type, which can be defined as $S_{\mathrm{e}} = \rho_{\mathrm{c,h}}/(\rho_{\mathrm{c,h}} + \rho_{\mathrm{c,e}}) = 1 - S_{\mathrm{h}}$, where S_{e} is the electron selectivity of the contact, S_{h} is the hole selectivity, and $\rho_{\mathrm{c,h}}$ and $\rho_{\mathrm{c,e}}$ are the resistivities to hole and electron conduction through the contacts, respectively.[24] It follows that a good CTL should be highly conductive for the majority carrier while highly resistive for the minority carrier.

Organic HTLs in p-i-n device structures are typically deposited on transparent conducting oxides (TCOs) by spin-coating. Ideally, the CTL should provide full coverage of the TCO surface to reduce nonradiative recombination at the TCO–perovskite interface that would also cause a lack of selectivity of the contact due to a leakage of oppositely charged carriers from the emissive layer. Furthermore, the CTLs should be as thin as possible to reduce series resistance, which can cause loss due to Joule heating. In addition, the thicknesses of the HTL and ETL require optimization such that the hole and electron currents to the perovskite emitter match each other, facilitating efficient bimolecular recombination.[9] The optical outcoupling efficiency (OOE) of the emitted light also depends on the refractive indices (n), extinction coefficients (k) and thicknesses of the constituent layers of the device. A device with a high internal electroluminescent quantum efficiency can have a relatively poor EQE_{EL} if the device stack (i.e., the perovskite and CTL thicknesses) is not optimized for a high outcoupling efficiency. It is clear to see that it is a significant challenge to balance all of these considerations to make high efficiency devices.

Chapter 6. Reducing Nonradiative Losses in Perovskite LEDs Through Atomic Layer Deposition of Al_2O_3 on the Hole-injection Contact

Atomic Layer Deposition (ALD) is a layer-by-layer deposition technique which is surface controlled allowing monolayer control of film growth.[25–27] The ALD process consists of sequential, self-limiting surface reactions as alternating precursors and co-reactants are introduced, separated by a purge of an inert gas. An ALD cycle may then be repeated to increase the number of layers and thus thickness of the thin film deposited. Adequate reactive sites are required on the substrate surface for the precursor to react with, ensuring the self-limiting nature. If no reactive sites are available, no further deposition can take place. The uniformity and unparalleled conformality provided by this technique have led to its favored use in the scaling down of microelectronics.[25,28–30] The low-temperature deposition and mild technique has also led to its application in perovskite solar cells[31–36] as well as deposition on temperature-sensitive polymers.[37–42]

Area-selective ALD (AS-ALD) takes advantage of the strong dependence of ALD on surface chemistry, where the commencement of growth is conditional to the substrate surface.[43,44] Here, deposition is limited to specific substrate areas, enabling predefined patterns to be established for bottom-up processing.[45–52] Unreactive polymers[53–57] as well as self-assembled monolayers (SAMs)[58–60] have been used to allow surface modification and to mask selective reactive areas to prevent ALD growth. These materials act as a physical barrier preventing the ALD precursor from reacting with substrate surface reactive groups. For unreactive polymers in this system, adequate ALD purges are required to inhibit the gaseous precursor from diffusing into the porous material and reaching the underlying substrate. If a sufficient purge is not applied, or if molecules become trapped in the porous polymer, these precursor molecules may then react with subsequent ALD precursors leading to a delayed nucleation and eventual growth.[39,61]

In this work we develop a composite hole-injection layer composed of poly(9,9-dioctylfluorene-alt-N-(4-sec-butylphenyl)-diphenylamine (TFB) and Al_2O_3. We employ principles from AS-ALD to form an intermixed TFB-Al_2O_3 layer that blocks pinholes and thus inhibits nonradiative recombination sites in the interface between the perovskite

and the hole-injection/electron blocking layer. The result is an ultrathin transport layer with a very high resistivity to electrons, while efficiently injecting holes. Our champion LED efficiency improves from 12 to 15 % EQE_{EL}, confirming the improved properties of the composite hole-injection layer.

6.3 Results and Discussion

6.3.1 Initial Characterization

For the green perovskite emitter, we employ the commonly used[15,16,20,62–65] material $CsPbBr_3$ within a phenylethylammonium bromide-rich (PEABr) matrix, processed as we have previously reported.[64] The emission wavelength varies depending upon the PEABr content. With 40 mol % excess PEABr in comparison to the CsBr, the wavelength sits within the green emission channel, with a PL peak position of 518 nm (Figure 6.1).

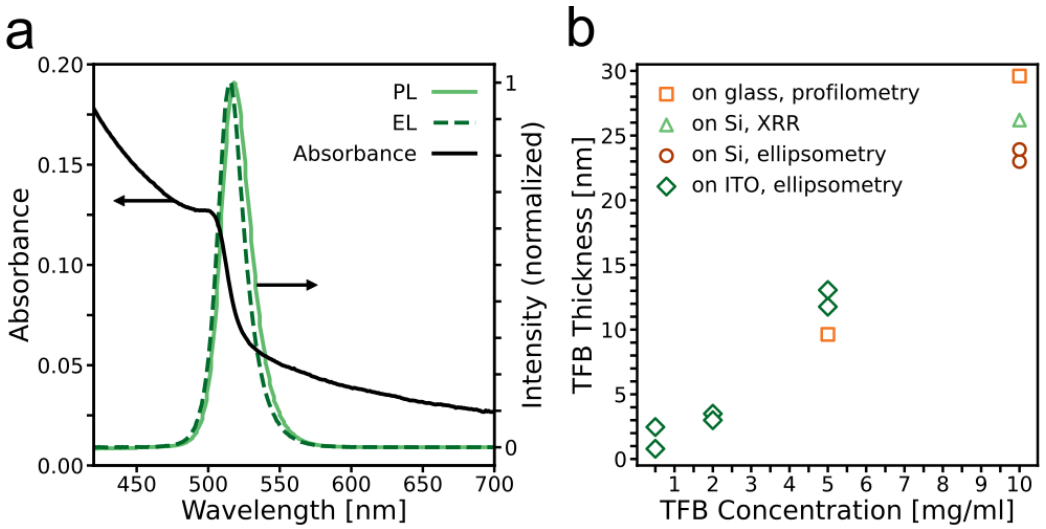

Figure 6.1: (a) Absorbance and PL spectrum of an isolated perovskite film on glass, EL spectrum from an LED. (b) Thickness of the deposited TFB layer on various substrates, measured using profilometry, ellipsometry and XRR.

We integrate the emission layer in LEDs with a p-i-n architecture of ITO / poly(9,9-dioctylfluorene-alt-N-(4-sec-butylphenyl)-diphenylamine (TFB) / LiF / perovskite

/ 2,2',2''-(1,3,5-Benzinetriyl)-tris(1-phenyl-1-H-benzimidazole) (TPBi) / LiF / Al (Figure 6.2 (a)). Using a similar structure, we have previously achieved EQE_{EL} of up to 12 %, but observed a photoluminescence quantum yield ($PLQY$) of up to 28 % from the same complete device stack.[64] The discrepancy between EQE_{EL} and $PLQY$ suggests there is an unrealized potential for higher efficiency in our devices. To improve the operating efficiency of the LEDs in this work, we adapt the HTL to optimize the hole-injection and electron-blocking nature of the p-side of the device.

To investigate how sensitive the LED performance is to the thickness of the hole-transport layer, we start by varying the thickness of the TFB layer by changing the concentration of TFB in the spin-coated solution and measure the $PLQY$ on encapsulated "half-stacks" (ITO / HTL / LiF / perovskite) and EQE_{EL} of devices (Figure 6.2 (b)).

We measure the thickness of TFB layers spin-coated from solutions of different concentration, and on various substrates, by means of profilometry, ellipsometry and x-ray reflectivity (XRR). The results are plotted in Figure 6.1 (b). Using the data in Figure 6.1 (b), we take the mean of the measured values to determine the thickness of TFB layers from solutions with 0.5, 2, 5 and 10 mg mL^{-1} TFB in chlorobenzene. The resulting mean thicknesses and standard deviations are given in Table 6.1. From these mean values, we use linear interpolation to determine the thickness of layers spun with solutions of 1, 3 and 8 mg mL^{-1}. These were interpolated between their nearest values, e.g. 1 mg mL^{-1} was determined by linear interpolation between 0.5 and 2 mg mL^{-1}.

When increasing the thickness of the TFB film, the $PLQY$ continues to increase, from average of 32 % for 1.6 nm TFB thickness to 37 % at 20 nm thickness, whereas the EQE_{EL} drops off when the TFB thickness exceeds 11 nm. Samples with TFB films thinner than 11 nm all yield progressively lower $PLQY$ and EQE_{EL}, but even the thinnest TFB layer in conjunction with the LiF layer enables significantly higher $PLQY$ than the perovskite on the bare ITO surface, with 32 % versus 11 % $PLQY$.

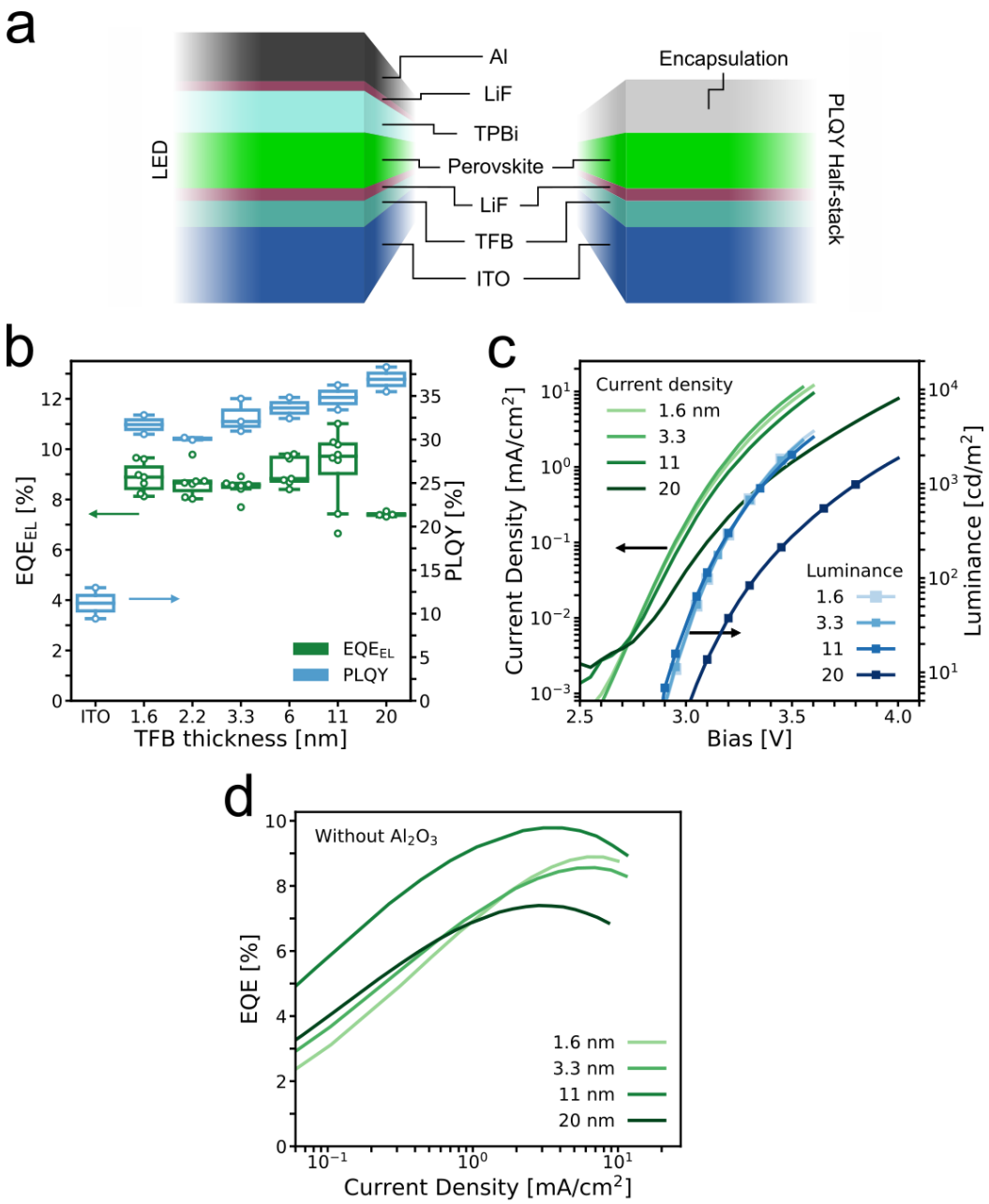

Figure 6.2: (a) Architecture of LED devices and half-stack samples for $PLQY$ measurements; thicknesses are not to scale; (b) devices with varying TFB layer thickness and no Al_2O_3 interlayer, EQE_{EL} values are the highest recorded EQE_{EL} for each device, $PLQY$ values are the average value per sample; (c) JVL characteristics of representative devices with varying TFB layer thickness; (d) EQE_{EL} as function of current density for devices with varying TFB thickness and without an Al_2O_3 interlayer.

Table 6.1: Thicknesses of TFB layers.

TFB Concentration [mg mL^{-1}]	Method	Thickness [nm]	Std.dev. [nm]
0.5	Mean	1.63	1.19
1.0	Linear interpolation	2.17	
2.0	Mean	3.25	0.35
3.0	Linear interpolation	6.00	
5.0	Mean	11.5	1.7
8.0	Linear interpolation	20.0	
10.0	Mean	25.7	2.9

Figure 6.2 (c) shows the voltage-dependence of the current density and luminance (JVL) of representative devices for each thickness. The device with the thickest TFB shows a strong reduction in both current density and luminance compared with the thinner ones. Between the three other devices there is almost no difference in luminance, but the current densities in the devices with the thinnest TFB films are slightly higher than for the more efficient device with 11 nm TFB. The EQE_{EL} as function of current density is given in Figure 6.2 (d).

Comparison of $PLQY$ and EQE_{EL} provides valuable insights into the causes for emission losses because $PLQY$ does not rely on carrier transport and injection to deliver carriers to the emitter, thus current transport losses and recombination losses can be uncoupled. In Figure 6.2 (b), we observe a general trend of increasing $PLQY$ with increasing TFB thickness. This is consistent with possible formation of "pinholes" in thinner TFB films. Contact between the perovskite emission layer with degenerately doped ITO would increase nonradiative recombination at the interface, leading to a reduction in emission, and, under bias, cause reduced selectivity, since electrons would be able to freely flow from the perovskite layer into the ITO. When the TFB thickness is increased, we assume the coverage over the ITO improves and reduced nonradiative recombination at this interface would lead to improvements in $PLQY$. If this is the case, there is a potential to improve the EQE_{EL} of devices with thinner TFB films compared to what we have achieved so far, by enabling improved coverage

of the ITO. Notably, when we increase the TFB thickness above 11 nm, we observe a significant reduction in the injection current density under forward bias and a drop in the EQE_{EL}. It is likely that this either originates from (a) an increased series resistance for hole injection, resulting in an imbalance of electrons and hole current flow through the device, or (b) a reduction in optical outcoupling, with thicker HTLs. An increase in series resistance for hole injection would only reduce EQE_{EL} and not $PLQY$, whereas a reduction in optical outcoupling should reduce both. We observe a monotonic increase in $PLQY$ with increasing TFB layer thickness, however, we do acknowledge that our $PLQY$ measurements are on half-stacks and could thus have a different outcoupling dependency on the thickness. Variations in thickness of this magnitude have been shown to result in changes in outcoupling efficiency.[66] The concurrent reduction in current density with increased TFB thickness implies increased hole-injection resistance as the primary factor reducing the EQE_{EL} for devices incorporating the thickest TFB layers.

6.3.2 Identifying Nonradiative Recombination Pathways and Improving Carrier Selectivity

To improve our understanding of the device performance, we investigate the morphology of the relevant layers in the device. We inspected the ITO and TFB layers by scanning electron microscopy (SEM), but are not able to discern any notable difference, possibly due to the penetration depth of the electron beam (Figure 6.3 (a-c)). We then measured the topography using atomic force microscopy (AFM). Comparing scans of the ITO surface (Figure 6.4 (a)) with scans of TFB thin films on ITO (Figure 6.4 (b-d)) no clear difference can be discerned. The TFB thin films all display a similar topography to the bare ITO, suggesting a conformal deposition of the polymer. There is however a decrease in the root mean square roughness (RMS) of the TFB thin films with increasing film thickness (Table 6.2). The RMS roughness of the underlying ITO surface, at 3.3 nm, is on the same range as the thickness we measured of the thinner

TFB layers employed. The reduction in roughness suggests that the TFB is partially planarizing the ITO substrate. Since the TFB thickness, for the thinner layers, is in the same range or less than the substrate roughness, it is likely that there will be some uncovered regions of ITO. Such uncovered regions protruding the TFB layer could act as contact point with the subsequently deposited perovskite emission layer.

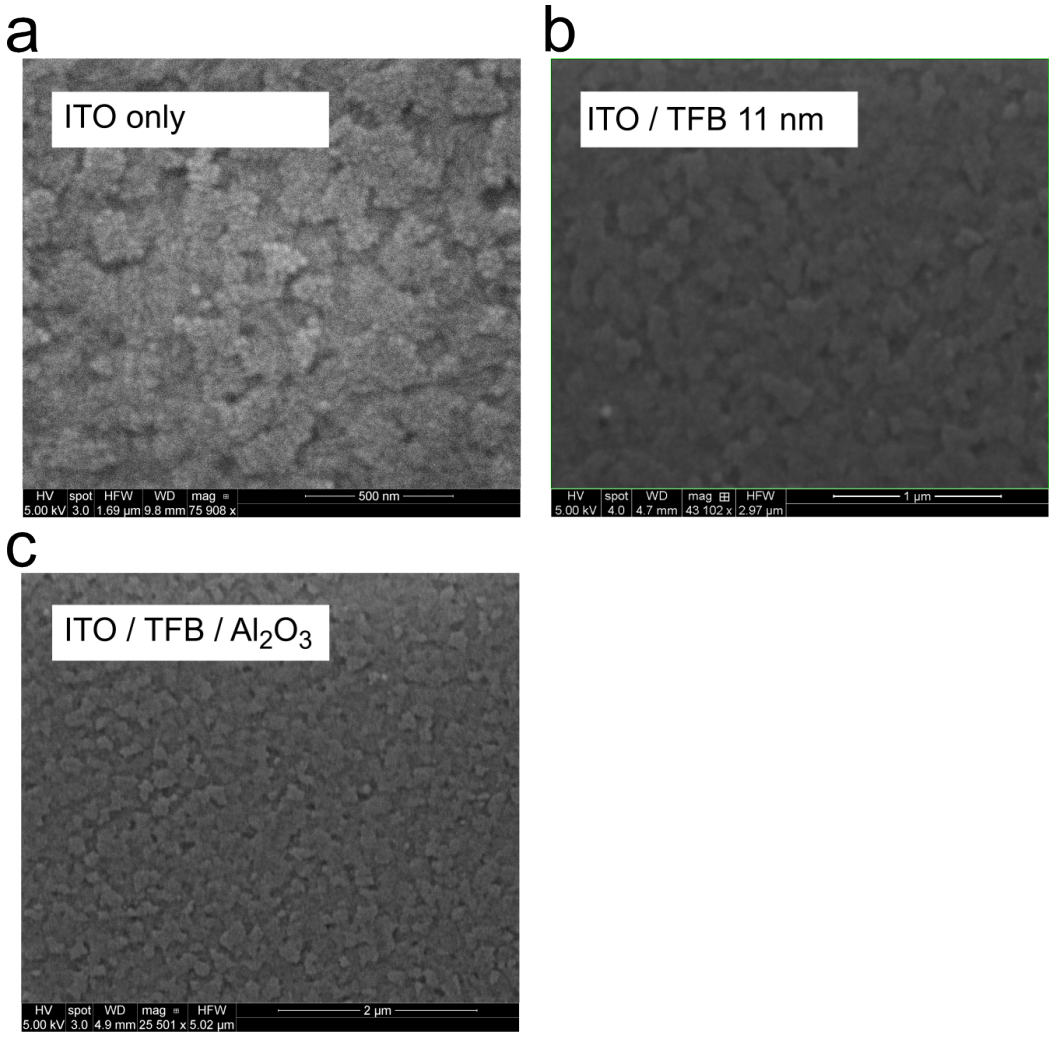

Figure 6.3: (a) SEM micrographs of the ITO substrate (a) and the ITO substrate with TFB (b) and TFB-Al_2O_3 layers (c), respectively.

With this potential for the presence of pinholes in the TFB layer we suspect that the resulting ITO–perovskite interface that can form is increasing nonradiative recombination losses and decreasing the hole-selectivity of the positive contact in our devices. To increase our understanding of how the TFB thickness may affect the

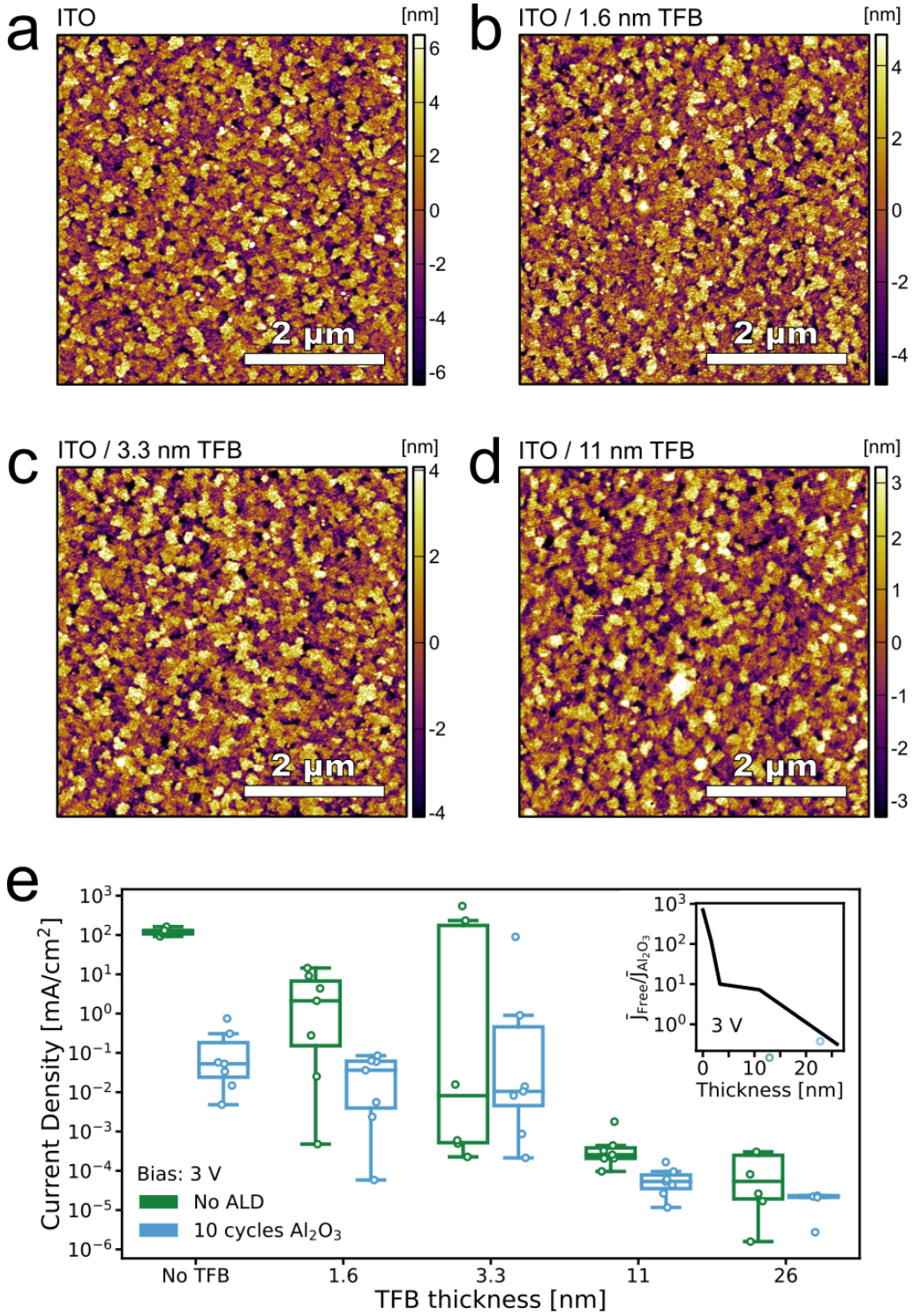

Figure 6.4: (a) AFM micrograph of the topography of the ITO glass surface; (b) ITO with 1.6 nm (0.5 mg mL^{-1}) TFB layer; (c) ITO with 3.3 nm (2 mg mL^{-1}) TFB layer; (d) ITO with 11 nm (5 mg mL^{-1}) TFB layer; (e) current density snapshot at 3 V bias for "electron-only" unipolar devices with varying TFB thickness and with or without the Al_2O_3 interlayer. In the inset in (e), the ratio of the mean of the current densities at 3 V for the Al_2O_3-free and Al_2O_3-covered samples is plotted as a function of TFB thickness.

Table 6.2: Root mean square roughness of surfaces in Figure 6.4 (a-d) determined by AFM.

Stack	Roughness [nm]
ITO	3.3
ITO / 1.6 nm TFB	2.7
ITO / 3.3 nm TFB	2.3
ITO / 11 nm TFB	1.7

selectivity of the positive contact, we construct unipolar, "electron-only" devices with the TFB layer sandwiched between two electron-selective contacts (Figure 6.5 (a)).

In this configuration, the ITO/SnO_2 contact should effectively block hole transport. This means the measured current flowing through the device should be due to electrons traveling through the entire device stack primarily, injected through the TPBi, passing through the SnO_2 and collected at the ITO electrode. When sandwiching a hole-selective material such as TFB between the SnO_2 and TPBi, we expect to see a reduction in measured current density due to the reduced electron transport through the thin-film stack. We do not expect to observe any hole-injection from the ITO/SnO_2 contact, and hence only consider the electron current. TFB layers with incomplete coverage should still allow a substantial electron current because of the bare SnO_2/TPBi interfaces. As such, this device configuration allows us to assess the completeness of the HTL layer coating in a more quantitative manner.

When we scan these unipolar devices (Figure 6.5 (b)), we see a difference in current density of roughly 6 orders of magnitude between the thickest TFB layer and the devices without any TFB. Figure 6.4 (e) shows the current densities of all devices at 3 V bias. The presence of 1.6 and 3.3 nm TFB layers decreases the current density by a few orders of magnitude but shows large variability between devices (green boxes in Figure 6.4 (e)). For 11 nm and above the variability is smaller and the current density is significantly suppressed.

Having identified clear evidence for current leakage through the thinner TFB layers, we hypothesize that this can be inhibited by including an additional thin interlayer of

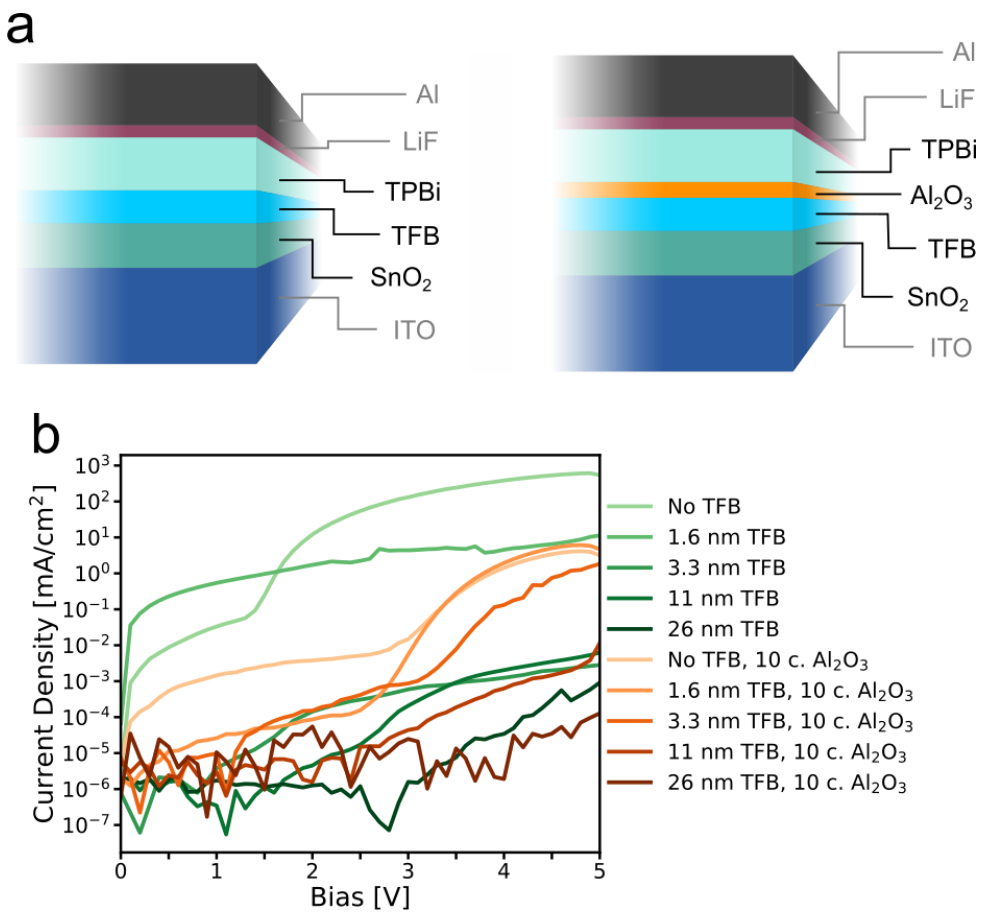

Figure 6.5: (a) Device schematic of the unipolar, electron-only devices with and without the ALD-Al_2O_3 interlayer. (b) JV-characteristics of one representative measurement each on unipolar electron-only devices. The modulus of the current density is plotted because of some negative value data near the noise limit of the instrument that cannot be displayed on a log plot.

an electrically insulating material. We proceed to compare with similar electron-only devices where we deposit a thin interlayer of Al_2O_3 via ALD on top of the TFB.

With an ALD-Al_2O_3 layer on top of the TFB in the sandwich between SnO_2 and TPBi (blue boxes in Figure 6.4 (e)), we see a further reduction in current density across all TFB concentrations. The relative reduction in electron current density due to the Al_2O_3 interlayer is of higher magnitude for the devices with no TFB, where the Al_2O_3 is deposited directly on the SnO_2, and for the thinnest TFB layers.

In the inset in Figure 6.4 (e) we plot the ratio of the mean of the current densities at 3 V for the Al_2O_3-free and Al_2O_3-processed samples ($\bar{J}_{\mathrm{free}}/\bar{J}_{\mathrm{Al_2O_3}}$). Without TFB, the mean current density is 700 times higher without the Al_2O_3-layer. With the thinnest TFB layer, 1.6 nm, the ratio is reduced but remains high at 120. With 3.3 nm and 11 nm TFB, the Al_2O_3 interlayer reduces the electron current density by a factor of 10 and 7, respectively. With a 26 nm TFB layer, the Al_2O_3 layer no longer causes a reduction in current density.

We have inspected ITO substrates with and without SnO_2 by SEM (Figure 6.6). The top-down micrographs (a and b) do not display any notable difference in the surface morphology. However, we note that due to the penetration depth of the SEM beam it is likely we probe deep into the ITO layer.

We also investigated an ITO–SnO_2 sample cross-section, Figure 6.6 (c-f). The SnO_2 layer has partially flaked off the substrate closest to the cleavage plane when the sample was cleaved for the cross-section, revealing both the ITO surface and a thin layer of SnO_2 further into the sample. The SnO_2 layer is visible as one or more layers of nanoparticles over the surface. The coating seems conformal, except for where the layer has flaked off during handling leaving debris on the surface. The micrographs suggest that the SnO_2 layer is somewhat rougher than the ITO substrate.

With ellipsometry of a SnO_2 layer on Si, assuming perfectly flat layers, we estimate the SnO_2 layer thickness to be 15 nm. This corresponds well with the observations from SEM, considering the surface roughness of the real layers.

Despite the differences in morphology of the SnO_2 and ITO layers, the data from unipolar electron-only devices still provides useful information. Figure 6.4 (e) shows that the incorporation of an ALD-Al_2O_3 interlayer provides a larger reduction in electron leakage current for thinner TFB layers than for thicker TFB layers. The roughness of the underlying substrate may affect the overall degree to which the leakage current is reduced for the thinner layers, but we expect the same trend to occur.

6.3.3 Al_2O_3 Interlayer in LEDs

Having seen the reduction in electron leakage current with the ALD-Al_2O_3 interlayer in our unipolar devices, we now incorporate the interlayer into the full LED stack (Figure 6.7 (a)). First, we make devices with varying number of deposition cycles of ALD, where one cycle involves an exposure to TMA and a subsequent exposure to deionized H_2O vapor. We do this on our best performing structure (11 nm TFB) and a clear increase in the EQE_{EL} with a maximum at 10 deposition cycles is observed (Figure 6.7 (b)). The average EQE_{EL} rises from 9.8 % at 0 cycles to 13.5 % at 10 cycles.

The difference in EQE_{EL} between the 0 and 10 ALD cycle samples is significant over the entire current-density range measured (Figure 6.7 (c)) yet the effect on the JV curves is small (Figure 6.7 (d)). This implies that the injected current and series resistance is not strongly influenced by the deposition of the Al_2O_3 interlayer, but the nonradiative current is significantly reduced.

In Figure 6.8 we plot the current density at 3.5 V as function of ALD cycles. The variation in current density is large for each sample type, but larger for 0 and 5 ALD cycles, and there is a large overlap between the boxes in the boxplot. Furthermore, the lower extreme is approximately the same for all sample types, whereas there are larger differences in the upper extreme. This is what would be expected for a reduction in the probability of active pinholes in the device. We also see that there is virtually no difference in the current density for samples with 10 versus 20 cycles of ALD, further

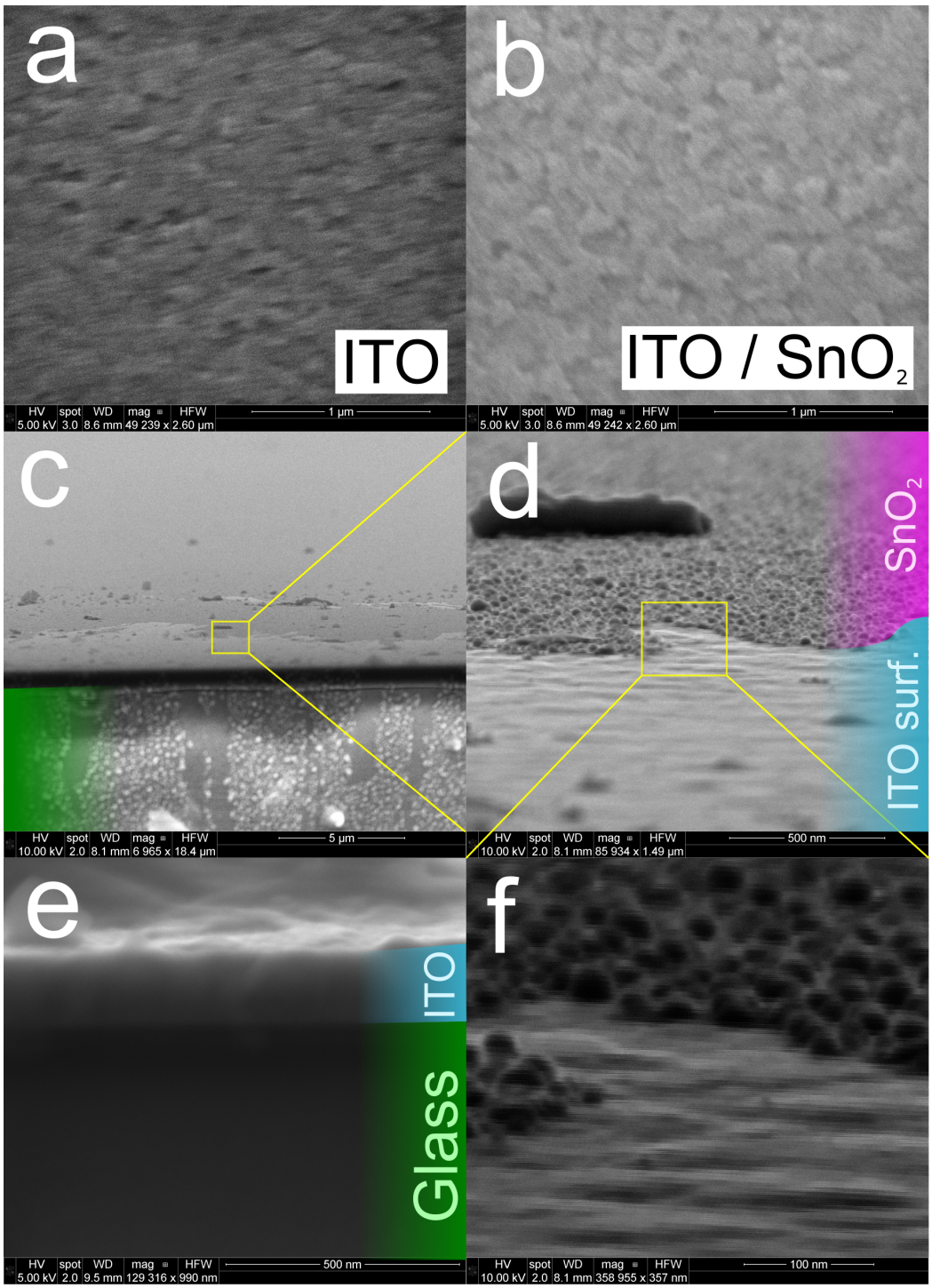

Figure 6.6: SEM micrographs of ITO and ITO-SnO_2 samples. (a) top-down micrographs of the ITO substrate; (b) top-down of ITO-SnO_2 contact; (c) cross-section of ITO-SnO_2 sample showing (from bottom to top) the glass cross-section, the ITO surface close to the cleavage where the SnO_2 has flaked off, and the SnO_2 surface; (d) zoomed area from cross-section in (c); (e) the ITO cross-section with a SnO_2-free surface next to the cleavage plane; (f) zoomed area from (d).

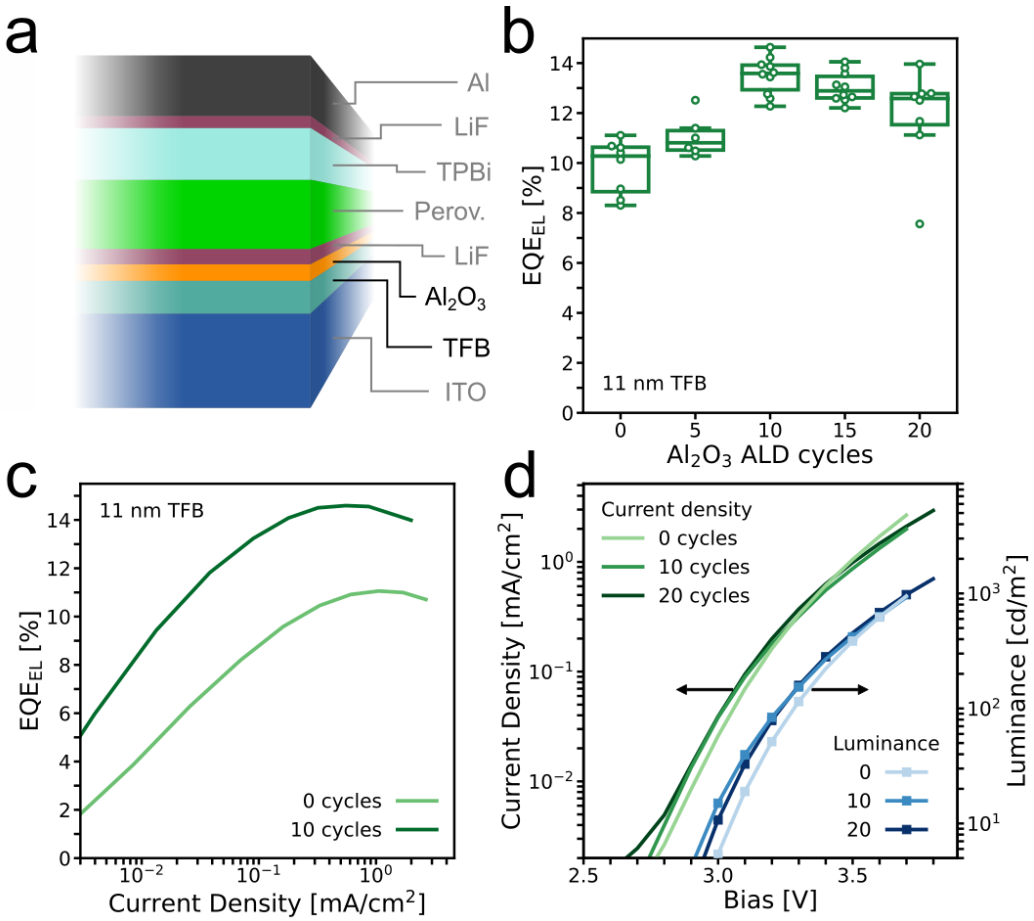

Figure 6.7: (a) Device schematic of the LEDs with the Al_2O_3 interlayer; (b) EQE_{EL} for each device with varying number of ALD cycles; (c) EQE_{EL} as a function of current density for the best performing device with and without the interlayer from the batch in (b); (d) JVL characteristics of the best performing devices with 0, 10 and 20 cycles from the batch in (b).

indicating that the insulating effect of SnO_2 does not decrease the current density except for a reduction in nonradiative current.

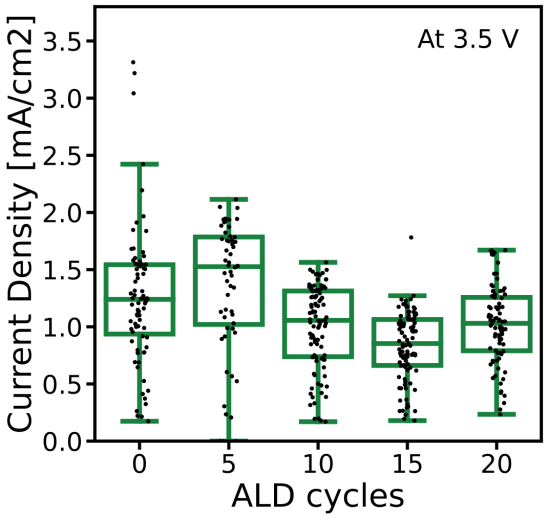

Figure 6.8: The current density at 3.5 V during JV-scans of LEDs made with 11 nm TFB and various numbers of Al_2O_3 ALD cycles. The data comprises 413 scans across 42 different samples.

Using AFM, we measure the topography also of samples of ITO/TFB/Al_2O_3. The effect of the ALD cannot be discerned from the micrographs, where samples with and without the interlayer look similar (Figure 6.9). We also measure the perovskite layer, but do not observe any changes in its morphology that can be attributed to the ALD-Al_2O_3 (Figure 6.10).

If the ALD-Al_2O_3 layer formed a dense and continuous layer on top of the TFB, we would expect to see a considerable reduction in current density through the LED, but we do not observe this even at the highest number of cycles tested (Figure 6.7 (d)). To further our understanding of the impact of this interlayer, we investigated two more configurations: removing the TFB layer and using ITO/Al_2O_3/LiF only as the hole-injection stack (type A); inserting the Al_2O_3 interlayer under the TFB layer i.e. depositing the oxide directly on the ITO before spin-coating the polymer: ITO/Al_2O_3/TFB/LiF (type B); and compare this with the well-performing ITO/TFB/Al_2O_3/LiF hole-injection stack (type C) with 11 nm TFB and 10 cycles ALD-Al_2O_3 (Figure 6.11 (a-b)).

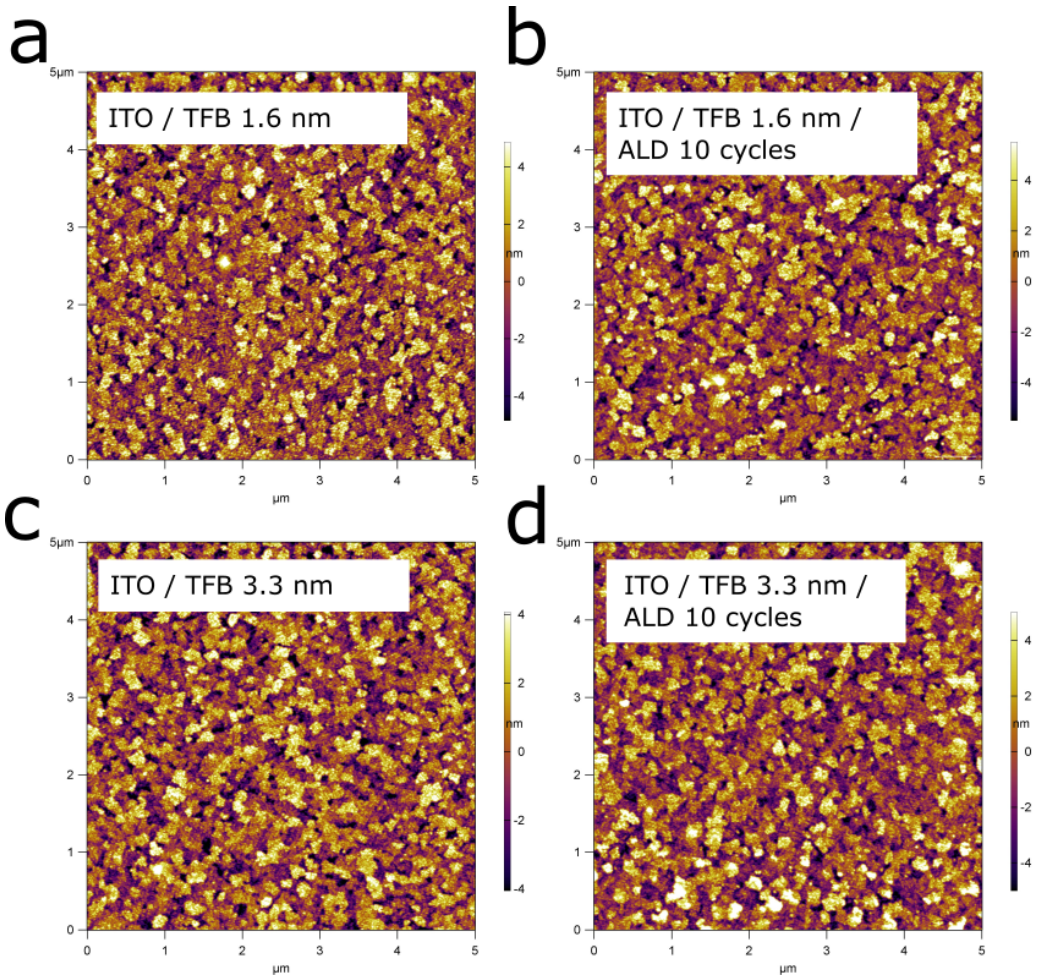

Figure 6.9: AFM micrographs of thin films with and without the ALD-Al_2O_3 layer.

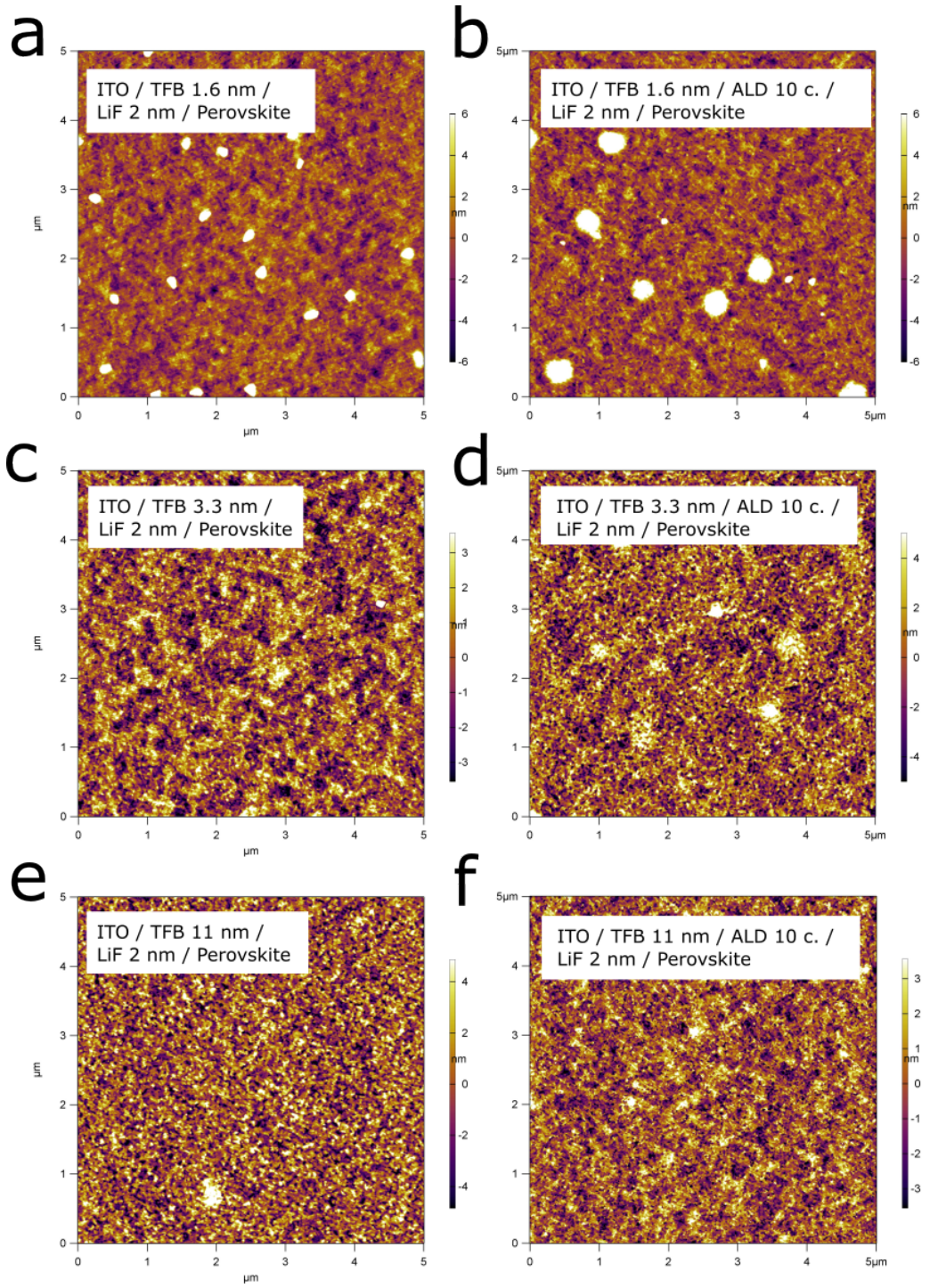

Figure 6.10: AFM micrographs of the perovskite films on various substrates.

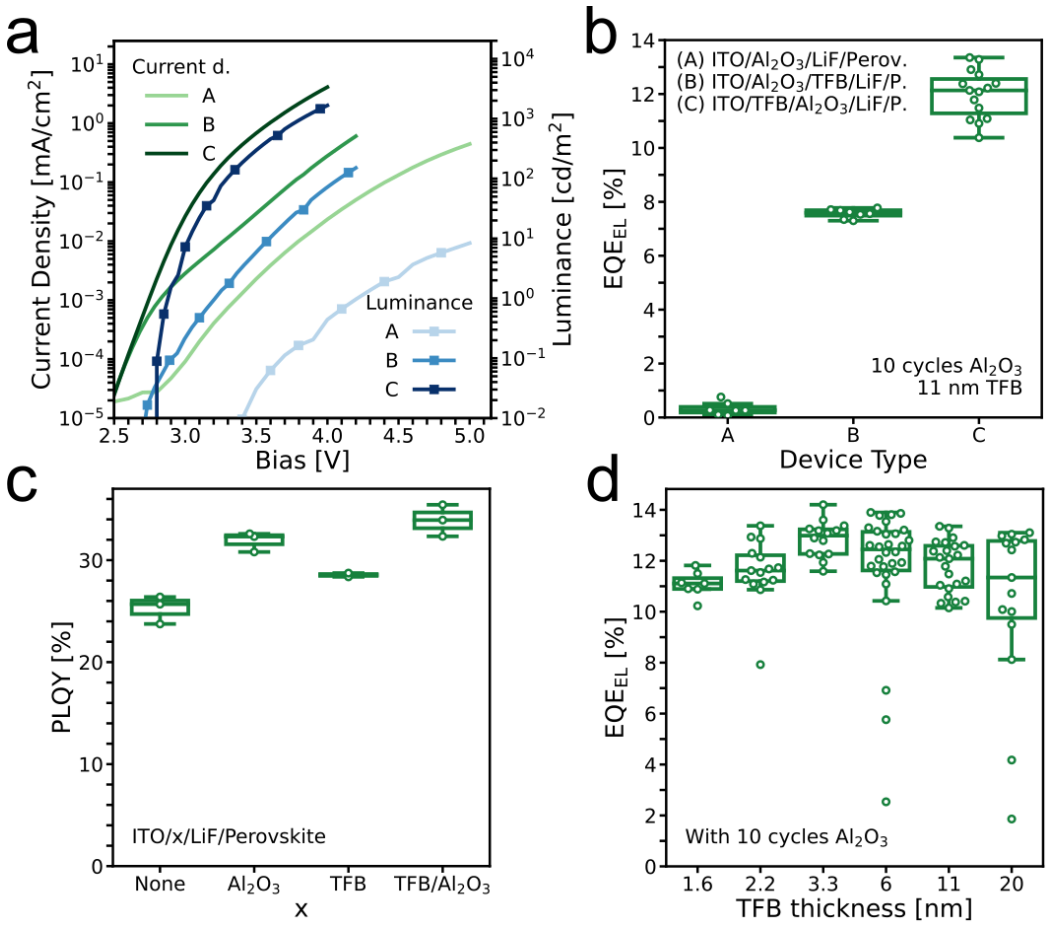

Figure 6.11: (a) JVL characteristics of different configurations of the 10 cycles of Al_2O_3 and 11 nm TFB layers: (i) no TFB HTL, only an Al_2O_3 interlayer; (ii) Al_2O_3 interlayer below the TFB; (iii) Al_2O_3 interlayer on top of the TFB; (b) EQE_{EL} the same type of devices; (c) $PLQY$ of devices with various layer configurations below the LiF wetting layer; (d) EQE_{EL} as a function of TFB thickness with the Al_2O_3 interlayer in place.

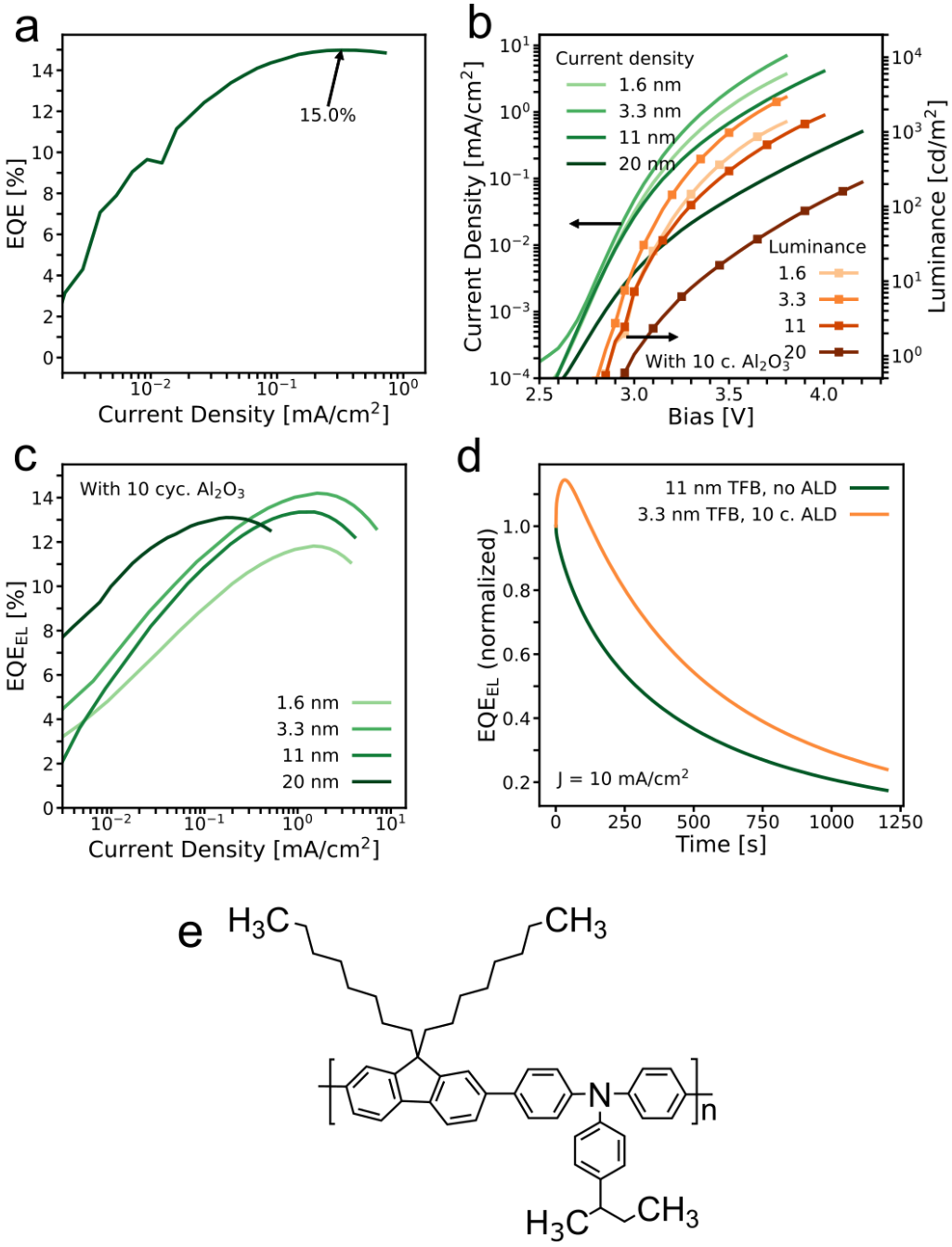

Figure 6.12: (a) Champion device measured in our lab. Device structure ITO/TFB/Al_2O_3/LiF/Perovskite/TPBi/LiF/Al. TFB 11 nm, 10 cycles of ALD. (b) JVL plot of devices with varying thickness of TFB with an Al_2O_3 interlayer (10 cycles of ALD). (c) EQE_{EL} as function of current density for devices with varying thickness of TFB with an Al_2O_3 interlayer. (d) EQE_{EL} as function of time for devices with and without the interlayer. Except for a change in the initial response, the decay rate is largely similar. (e) Skeletal diagram of poly(9,9-dioctylfluorene-alt-N-(4-sec-butylphenyl)-diphenylamine) (TFB).

Without the TFB layer (type A), the LEDs have a very high resistance, the current density is reduced by two orders of magnitude relative to the control (type C) and the efficiency is below 1 %. With the Al_2O_3 directly on the ITO and then TFB above (type B), the current density is increased, but still an order of magnitude below that of the control. The luminance of the type B devices is also much higher than that of type A devices, but more than an order of magnitude lower than the control devices with TFB then Al_2O_3 (type C). These results suggest that the Al_2O_3 deposition does not form a dense, predominantly continuous, insulating layer when applied on top of TFB, but does form a more continuous and insulating layer on ITO. Thus, our original configuration still allows efficient hole injection through the TFB to the perovskite emission layer.

We now inspect the effect of 10 cycles of the aluminum oxide interlayer on the $PLQY$ of half-stacks, as shown in Figure 6.11 (c), and find an increase of 5 % absolute $PLQY$ with the ALD-Al_2O_3 layer processed on top of the 11 nm TFB layer. We also see that the combination of the thin Al_2O_3 and LiF interlayers are able to quite effectively suppress nonradiative recombination at the ITO interface, obtaining high $PLQYs$.

Now that we have found an effective method to improve our contacts by reducing nonradiative recombination, we try to optimize the LEDs further by varying the TFB layer thickness while keeping the ALD-Al_2O_3 layer constant at 10 cycles. As shown in Figure 6.11 (d), the optimum TFB thickness is shifted such that we now find the highest efficiencies in devices prepared with 3.3 nm TFB layers. The champion EQE_{EL} in Figure 6.11 (d) is 14.2 %, but we note that we have reached 15.0 % in a 11 nm device with Al_2O_3 interlayer early in this study (Figure 6.12 (a)) and we therefore expect to be able to obtain even higher efficiencies for this configuration with 3.3 nm TFB and 10 cycles ALD-Al_2O_3. We note that even the devices with 20 nm TFB show a significant improvement in EQE_{EL} with the Al_2O_3 interlayer (comparing the data presented in Figure 6.2 (b) and Figure 6.11 (d)). JVL and $EQE_{EL}(J)$ for the different concentrations with the Al_2O_3 interlayer are given in Figure 6.12 (b) and

(c), respectively. The LED operational stability over time remains largely unchanged by the inclusion of the Al_2O_3 interlayer (Figure 6.12 (d)).

We thus see an improvement in device performance with the Al_2O_3 interlayer across all TFB thicknesses, with a greater change in samples where the TFB coverage is expected to be lower because of the lower thickness. We can attribute this to the difference in growth characteristics of the Al_2O_3 on ITO and on TFB.

In the ALD process of Al_2O_3, the trimethylaluminum precursor reacts with functional groups on the surface to chemisorb on the substrate. In the subsequent steps of the cycle, the gaseous TMA is purged out of the deposition chamber and the second precursor, in this case H_2O, is let into the chamber. The H_2O reacts with the chemisorbed TMA to form a monolayer of aluminum oxide. The nucleation of the Al_2O_3 layer is therefore strongly dependent on the chemistry between the TMA precursor and the substrate surface. As metal oxides, the surfaces of both ITO and SnO_2 are likely to be terminated by hydroxide groups, which react strongly with TMA. Therefore, a short and effective nucleation phase is expected on these surfaces before the process enters the linear growth phase that is characteristic for Al_2O_3 ALD growth.[43]

On the other hand, many polymers do not possess a high density of functional groups for TMA to bind with and are relatively inert to the ALD nucleation process.[61] Inspecting the molecular structure of TFB (Figure 6.12 (e)), it is clear that there are no –OH, –COOH or primary amine groups for TMA to react with. TMA, being a strong Lewis acid, could in theory react with the amine group (Lewis base) on the TFB monomer. However, since this is a tertiary amine, it is not expected to be very reactive.

If TMA cannot readily react on the TFB surface, another possibility is for the gaseous TMA molecules to diffuse into micropores within the polymer layer. If, during the following purge, a fraction of the TMA molecules is unable to escape the pores of the TFB, the TMA will then be free to react with molecules in the next pulse.

This would initiate a nucleation and growth of Al_2O_3 particles within the TFB film, effectively resulting in a composite of a TFB matrix infused with Al_2O_3 particles.

To gain understanding of the growth of the Al_2O_3 interlayer, we perform energy dispersive X-ray spectroscopy (EDS) mapping in SEM on a sample of ITO with 11 nm TFB and 20 cycles ALD-Al_2O_3, where we masked parts of the substrate with polyimide tape during the TFB spin-coating and then removed the tape to expose this area during ALD. The data is shown in Figure 6.13 (a) and Figure 6.14. We see an increased intensity of Al K_α counts in the area with TFB coverage compared to in areas with just ITO. This implies that there is a larger amount of Al_2O_3 in this area. This suggests we may have some Al_2O_3 growth in the TFB pores.

To further investigate the potential intergrowth of Al_2O_3 within TFB, we deposit TFB and TFB-Al_2O_3 layers on silicon substrates and measure the thickness using both profilometry and ellipsometry, see Figure 6.13 (b) and Figure 6.15. We see from Figure 6.15 (a-b) that the thickness determined by the two different methods follow each other closely, except at higher ALD cycles the thickness determined by ellipsometry is consistently slightly higher than the average values given by profilometry. Figure 6.15 (c) shows the increase in thickness as function of ALD cycles relative to the bare TFB (0 cycles). The measured thickness increase exceeds the value expected from linear growth of Al_2O_3 by ALD (1.1 Å per cycle),[43] which would be expected from a continuous film on the TFB surface. In contrast, our deposition of Al_2O_3 directly on a Si substrate with native oxide follows this rate much more closely (Figure 6.15 (b-c)). After 10 cycles, the 11 nm TFB-Al_2O_3 film increases in thickness by 3 to 5 nm, or 30 to 50 %, relative to the pristine TFB film (Figure 6.15 (d)). Much more than the expected 1.1 nm. The layer continues to expand substantially also for 20 and 50 cycles of ALD and the trend is similar for a thicker pristine TFB film of 26 nm.

From this data, we draw the conclusion that the Al_2O_3 likely grows within pores in the TFB film, resulting in swelling of the TFB layer and the formation of a TFB-Al_2O_3 composite layer. The number of deposition cycles explored in devices in this work (0-20 cycles) are also well within the range considered to be the nucleation phase

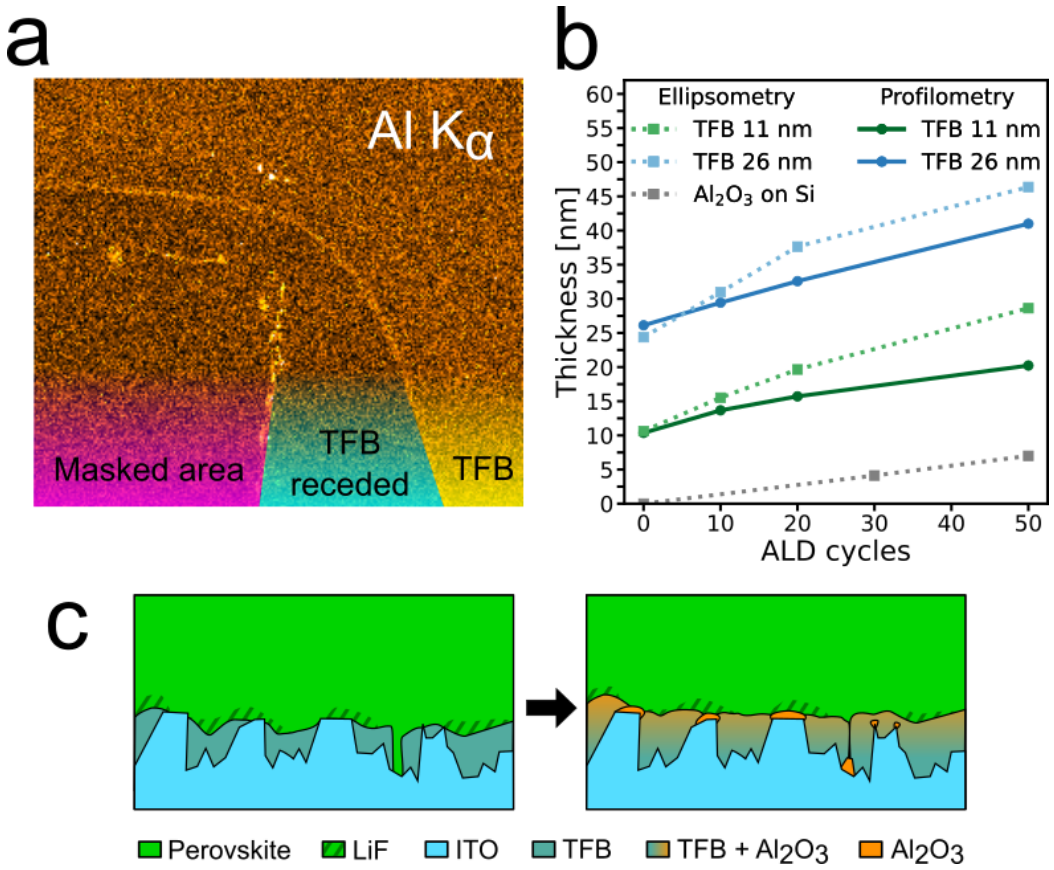

Figure 6.13: (a) Al K_α counts from EDS mapping over a sample with 11 nm TFB on ITO and then 20 cycles ALD-Al_2O_3, where a part of the sample was masked by polyimide tape during TFB spin-coating. Increased brightness indicates higher count intensity. The color coding indicates: (magenta) the area that was masked and is therefore TFB-free; (cyan) an area around the masking tape where the TFB had receded after spin-coating; (yellow) a TFB-covered area; (b) thickness of TFB-Al_2O_3 samples on Si and Al_2O_3 on Si samples as function of ALD-Al_2O_3 cycles, where the thicknesses were determined by profilometry (average values) and ellipsometry; (c) illustration of ALD-Al_2O_3 causing a swelling of the TFB by intermixed growth of Al_2O_3, and growth of Al_2O_3 on exposed ITO surfaces. Not to scale.

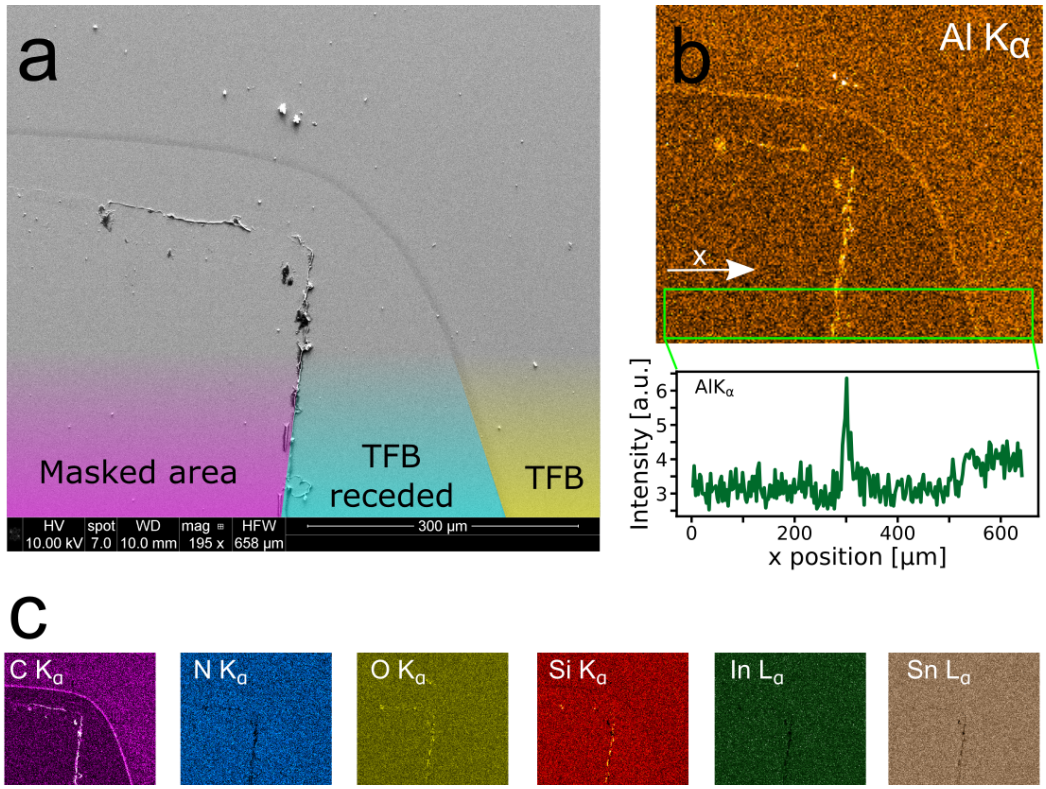

Figure 6.14: (a) SEM secondary electron micrograph of the location on that was EDS mapped. The sample was an ITO substrate with 11 nm TFB and 20 cycles ALD-Al_2O_3, where parts of the sample was masked by polyimide tape during TFB spin-coating. The color coding indicates: (magenta) the area that was masked and is therefore TFB-free; (cyan) an area around the masking tape where the TFB had receded after spin-coating; (yellow) a TFB-covered area. (b) EDS map of the Al K_α counts over the area, with a plot of the average intensity along x within the indicated rectangle. (c) Maps of EDS intensities of other elements over the same area.

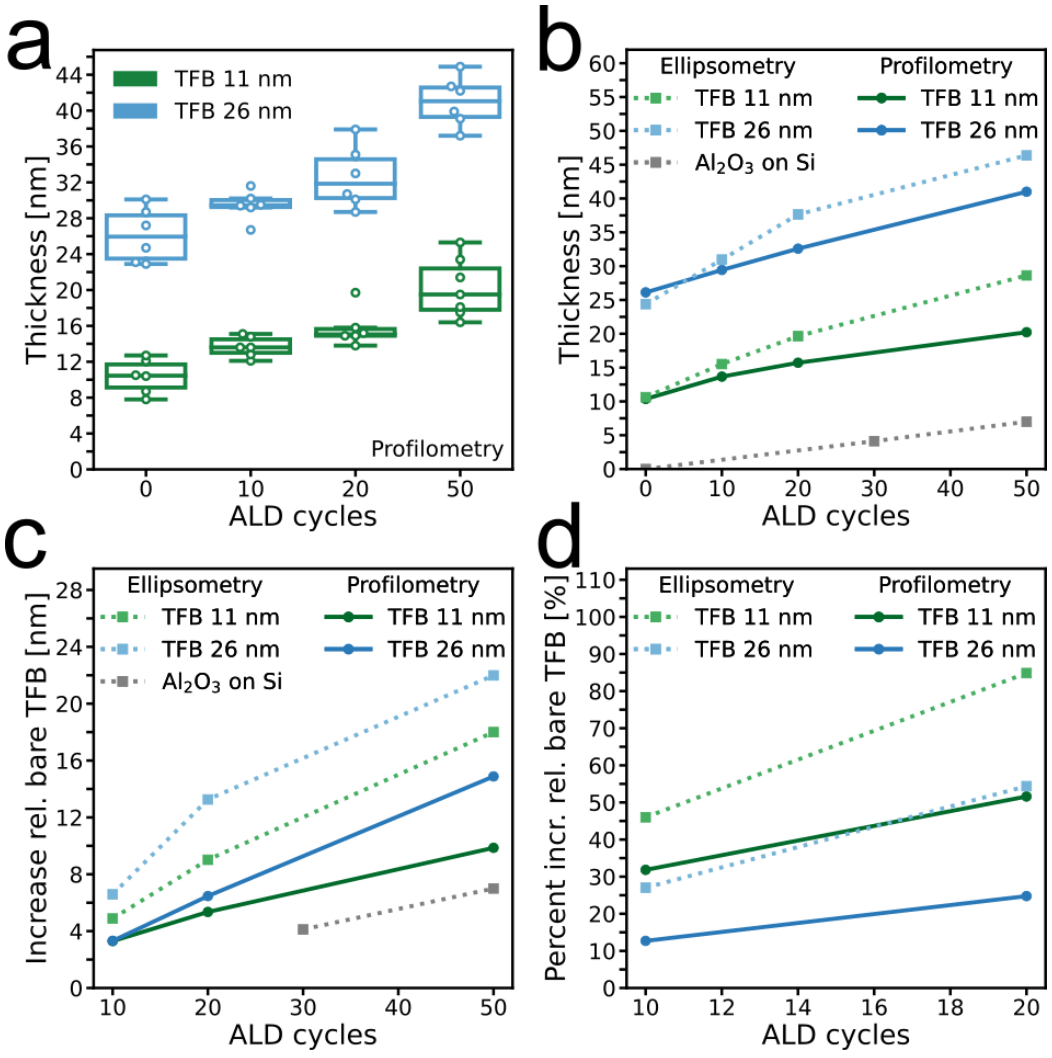

Figure 6.15: (a) Boxplots of profilometry measurements of 6 to 7 samples per physical sample, showing the distribution of results. (b) Thickness of samples as function of ALD-Al_2O_3 cycles exposed to. Thicknesses were determined by profilometry (average values) and ellipsometry. ALD-Al_2O_3 on Si shows close to expected linear growth of 1.1 Å per cycle. (c) The thickness increase for each sample relative to the 0 ALD samples. (d) The percent increase in thickness of samples exposed to 10 or 20 ALD cycles relative to 0 cycles.

for growth on many common polymers, before which a conformal linear growth is reached.[39] This could further help explain why there does not seem to be a conformal, insulating blocking layer of Al_2O_3 formed, despite there being significant volume of Al_2O_3 within the film.

We thus propose that the application of ALD-Al_2O_3 acts by improving the devices in two ways: (1) Any uncovered ITO regions on the substrates may be insulated by a more reactive growth in this area, forming a thin but dense and conformal film, and (2) the surface of the TFB is not insulated but the swelling could also act to seal micropores and cause a more continuous surface for subsequent layers in the device fabrication. See schematic in Figure 6.13 (c).

This premise is consistent with the changes we observed for the different LED device configurations. For our "control" devices, incomplete coverage or pinholes in the TFB film lead to nonradiative electron-hole recombination and poor selectivity at the perovskite interface with the ITO (Figure 6.16 (a)). When applying the ALD-Al_2O_3 process, hole conduction through the TFB is sustained, since the Al_2O_3 does not form a dense, continuous layer capping the TFB, but rather interpenetrates the polymer. This therefore greatly reduces the electron leakage current, while allowing hole-injection current to flow (Figure 6.16 (b-c)). This confines a higher proportion of the injected electrons to the emitter layer, where they can radiatively recombine with the holes. With the TFB-Al_2O_3 HTL, reduction of the initial TFB thickness, even accounting for swelling post ALD, reduces the hole injection resistance, without the drawback of increased nonradiative recombination from the increasingly large area of exposed ITO surface.

We see an EQE_{EL} increase with 10 cycles of ALD-Al_2O_3 also for the thicker TFB layers (Figure 6.11 (d)), which is indicative that there could be other positive effects associated with the TFB-Al_2O_3 composite. The composite could have a better energetic alignment compared to that of neat TFB, facilitating improved hole-injection into the perovskite layer. Another possibility is that the composite aids an enhancement of the following layer depositions, either the evaporated LiF or the

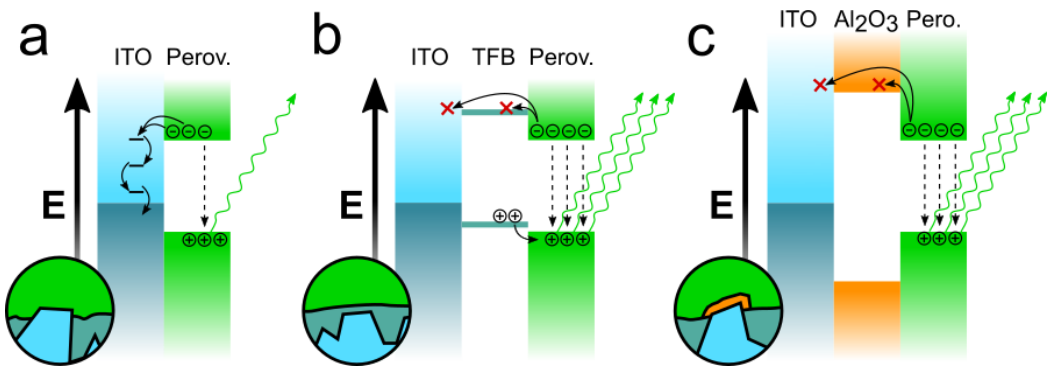

Figure 6.16: (a) Energy band schematic displaying efficient hole injection and electron-blocking behavior with TFB; (b) electron leakage at the ITO–perovskite interface when the ITO is left exposed; (c) efficient electron blocking with Al_2O_3 covering the exposed ITO. Not to scale

spin-coated perovskite layer. However, our experience with this emission layer indicates that the perovskite crystallization is mostly governed by the 18-crown-6 additive and the presence of the LiF wetting layer.[64] It could also be the case that the reduced HTL thickness has improved the optical outcoupling of the device, though over the layer thickness range (between 3 to 11 nm), which is significantly less than the wavelength of light, we would not expect dramatic changes. A thorough optical model would be needed to confirm this, which is beyond the scope of this work.

This technique, exploiting differences in chemical reactivity of ALD precursors and growth modes between the organic HTL and the underlying TCO to achieve selective insulation of leakage pathways, thus widens the optimization window for device design by expanding the range of viable organic charge transport layer thicknesses that can be used to produce highly efficient devices. In our work, the efficiency gain primarily comes from improved selectivity of the contact. However, in other applications the technique also offers the possibility to optimize the optical outcoupling efficiency through variations of layer thickness without losing carrier selectivity. The combination of an insulator by ALD with an organic charge transport layer may in the future be adapted to other organic charge transport layers, other device architectures, such as n-i-p devices, or other fields such as perovskite photovoltaics. Since ALD systems are common in semiconductor research labs, the technique has potential for fast implementation into a large variety of applications. Through commercially available

spatial and roll-to-roll ALD systems, the technique should be suitable for scale up to larger area LED arrays.[67]

6.4 Conclusion

The imperfect wetting associated with solution processing can introduce serious spatial inhomogeneities in PeLEDs, presenting a major challenge to scale-up. This challenge is particularly exacerbated by the requirement to have very thin transport layers for the highest efficiencies. Here, we show how ALD can be exploited to improve the quality of the hole-injection layer and contacts, which we rationalize to be due to preferential blocking of regions with pinholes through both swelling of the polymer layer caused by Al_2O_3 growth in the pores of the polymer and preferential Al_2O_3 growth on exposed TCO surfaces, while the polymer surface remains electronically accessible to the perovskite emitter. The improved TFB-Al_2O_3 contact reduces nonradiative recombination sites where there is contact between the degenerately doped ITO and the perovskite emission layer, improving the selectivity of the contact. This allows us to improve the hole-injection into the emission layer further by reducing the thickness of the HTL, thus reducing the series resistance for hole-injection without introducing additional nonradiative recombination sites. The technique is broadly applicable to a variety of organic transport layers, and could expand the optimization window of a variety of devices architectures without trade-off in performance due to loss in contact selectivity.

In a possible follow-up of this work, a variety of investigations would be interesting. One, the understanding of the deposition mechanisms could be improved by in-situ probing of the mass change during ALD by e.g. deposition on a quartz crystal microbalance and using in-situ ellipsometry. Two, the energetics of the TFB-Al_2O_3 composite could be investigated with e.g. x-ray photoelectron spectroscopy to determine whether there actually are chemical interactions between the species and how this affects the energetic alignment in the device. Three, the charge balance in the optimized devices

could be inspected by e.g. fabrication and characterization of unipolar devices of both polarities. Four, a larger study of the effect of deposition parameters (temperature, dwell time, pressure) would be interesting to see if the properties could be further improved, and if these parameters affect any of the investigation topics suggested previously. Lastly, five, a study on the application of this technique to a variety of organic transport layers would be warranted, as well as using other oxides in the ALD process.

References

1. M. M. Lee, J. Teuscher, T. Miyasaka, T. N. Murakami, and H. J. Snaith, "Efficient Hybrid Solar Cells Based on Meso-Superstructured Organometal Halide Perovskites," *Science*, vol. 338, no. 6107, pp. 643–647, 2012.
2. L. Gao and Q. Yan, "Recent Advances in Lead Halide Perovskites for Radiation Detectors," *Sol. RRL*, vol. 4, no. 2, p. 1900210, 2020.
3. Z.-K. Tan, R. S. Moghaddam, M. L. Lai, P. Docampo, R. Higler, F. Deschler, M. Price, A. Sadhanala, L. M. Pazos, D. Credgington, F. Hanusch, T. Bein, H. J. Snaith, and R. H. Friend, "Bright light-emitting diodes based on organometal halide perovskite," *Nature Nanotech*, vol. 9, no. 9, pp. 687–692, 2014.
4. Z. Hu, Z. Liu, Z. Zhan, T. Shi, J. Du, X. Tang, and Y. Leng, "Advances in metal halide perovskite lasers: synthetic strategies, morphology control, and lasing emission," *Adv. Photon.*, vol. 3, no. 03, 2021.
5. X. Yu, H. N. Tsao, Z. Zhang, and P. Gao, "Miscellaneous and Perspicacious: Hybrid Halide Perovskite Materials Based Photodetectors and Sensors," *Adv. Optical Mater.*, vol. 8, no. 21, p. 2001095, 2020.
6. A. R. Bowman, M. Anaya, N. C. Greenham, and S. D. Stranks, "Quantifying Photon Recycling in Solar Cells and Light-Emitting Diodes: Absorption and Emission Are Always Key," *Phys. Rev. Lett.*, vol. 125, no. 6, p. 067401, 2020.
7. C. Cho, B. Zhao, G. D. Tainter, J.-Y. Lee, R. H. Friend, D. Di, F. Deschler, and N. C. Greenham, "The role of photon recycling in perovskite light-emitting diodes," *Nat Commun*, vol. 11, no. 1, p. 611, 2020.
8. L. M. Pazos-Outón, M. Szumilo, R. Lamboll, J. M. Richter, M. Crespo-Quesada, M. Abdi-Jalebi, H. J. Beeson, M. Vrućinić, M. Alsari, H. J. Snaith, B. Ehrler, R. H. Friend, and F. Deschler, "Photon recycling in lead iodide perovskite solar cells," *Science*, vol. 351, no. 6280, pp. 1430–1433, 2016.
9. S. D. Stranks, R. L. Z. Hoye, D. Di, R. H. Friend, and F. Deschler, "The Physics of Light Emission in Halide Perovskite Devices," *Adv. Mater.*, vol. 31, no. 47, p. 1803336, 2019.
10. T. Chiba, Y. Hayashi, H. Ebe, K. Hoshi, J. Sato, S. Sato, Y.-J. Pu, S. Ohisa, and J. Kido, "Anion-exchange red perovskite quantum dots with ammonium iodine salts for highly efficient light-emitting devices," *Nature Photon*, vol. 12, no. 11, pp. 681–687, 2018.

11. Y. Cao, N. Wang, H. Tian, J. Guo, Y. Wei, H. Chen, Y. Miao, W. Zou, K. Pan, Y. He, H. Cao, Y. Ke, M. Xu, Y. Wang, M. Yang, K. Du, Z. Fu, D. Kong, D. Dai, Y. Jin, G. Li, H. Li, Q. Peng, J. Wang, and W. Huang, "Perovskite light-emitting diodes based on spontaneously formed submicrometre-scale structures," *Nature*, vol. 562, no. 7726, pp. 249–253, 2018.

12. B. Zhao, S. Bai, V. Kim, R. Lamboll, R. Shivanna, F. Auras, J. M. Richter, L. Yang, L. Dai, M. Alsari, X.-J. She, L. Liang, J. Zhang, S. Lilliu, P. Gao, H. J. Snaith, J. Wang, N. C. Greenham, R. H. Friend, and D. Di, "High-efficiency perovskite–polymer bulk heterostructure light-emitting diodes," *Nature Photon*, vol. 12, no. 12, pp. 783–789, 2018.

13. Y. Hassan, J. H. Park, M. L. Crawford, A. Sadhanala, J. Lee, J. C. Sadighian, E. Mosconi, R. Shivanna, E. Radicchi, M. Jeong, C. Yang, H. Choi, S. H. Park, M. H. Song, F. De Angelis, C. Y. Wong, R. H. Friend, B. R. Lee, and H. J. Snaith, "Ligand-engineered bandgap stability in mixed-halide perovskite LEDs," *Nature*, vol. 591, no. 7848, pp. 72–77, 2021.

14. C. M. M. Soe, G. P. Nagabhushana, R. Shivaramaiah, H. Tsai, W. Nie, J.-C. Blancon, F. Melkonyan, D. H. Cao, B. Traoré, L. Pedesseau, M. Kepenekian, C. Katan, J. Even, T. J. Marks, A. Navrotsky, A. D. Mohite, C. C. Stoumpos, and M. G. Kanatzidis, "Structural and thermodynamic limits of layer thickness in 2D halide perovskites," *Proc. Natl. Acad. Sci. U.S.A.*, vol. 116, no. 1, pp. 58–66, 2019.

15. M. Ban, Y. Zou, J. P. H. Rivett, Y. Yang, T. H. Thomas, Y. Tan, T. Song, X. Gao, D. Credgington, F. Deschler, H. Sirringhaus, and B. Sun, "Solution-processed perovskite light emitting diodes with efficiency exceeding 15% through additive-controlled nanostructure tailoring," *Nat Commun*, vol. 9, no. 1, p. 3892, 2018.

16. L. N. Quan, Y. Zhao, F. P. García de Arquer, R. Sabatini, G. Walters, O. Voznyy, R. Comin, Y. Li, J. Z. Fan, H. Tan, J. Pan, M. Yuan, O. M. Bakr, Z. Lu, D. H. Kim, and E. H. Sargent, "Tailoring the Energy Landscape in Quasi-2D Halide Perovskites Enables Efficient Green-Light Emission," *Nano Lett.*, vol. 17, no. 6, pp. 3701–3709, 2017.

17. D. W. deQuilettes, S. Koch, S. Burke, R. K. Paranji, A. J. Shropshire, M. E. Ziffer, and D. S. Ginger, "Photoluminescence Lifetimes Exceeding 8 µs and Quantum Yields Exceeding 30% in Hybrid Perovskite Thin Films by Ligand Passivation," *ACS Energy Lett.*, vol. 1, no. 2, pp. 438–444, 2016.

18. I. L. Braly, D. W. deQuilettes, L. M. Pazos-Outón, S. Burke, M. E. Ziffer, D. S. Ginger, and H. W. Hillhouse, "Hybrid perovskite films approaching the radiative limit with over 90% photoluminescence quantum efficiency," *Nature Photon*, vol. 12, no. 6, pp. 355–361, 2018.

19. M. Abdi-Jalebi, Z. Andaji-Garmaroudi, S. Cacovich, C. Stavrakas, B. Philippe, J. M. Richter, M. Alsari, E. P. Booker, E. M. Hutter, A. J. Pearson, S. Lilliu, T. J. Savenije, H. Rensmo, G. Divitini, C. Ducati, R. H. Friend, and S. D. Stranks, "Maximizing and stabilizing luminescence from halide perovskites with potassium passivation," *Nature*, vol. 555, no. 7697, pp. 497–501, 2018.

20. C. Zou, Y. Liu, D. S. Ginger, and L. Y. Lin, "Suppressing Efficiency Roll-Off at High Current Densities for Ultra-Bright Green Perovskite Light-Emitting Diodes," *ACS Nano*, vol. 14, no. 5, pp. 6076–6086, 2020.

21. J. Wang, N. Wang, Y. Jin, J. Si, Z.-K. Tan, H. Du, L. Cheng, X. Dai, S. Bai, H. He, Z. Ye, M. L. Lai, R. H. Friend, and W. Huang, "Interfacial Control Toward Efficient and Low-Voltage Perovskite Light-Emitting Diodes," *Adv. Mater.*, vol. 27, no. 14, pp. 2311–2316, 2015.

22. Y. Shi, W. Wu, H. Dong, G. Li, K. Xi, G. Divitini, C. Ran, F. Yuan, M. Zhang, B. Jiao, X. Hou, and Z. Wu, "A Strategy for Architecture Design of Crystalline Perovskite Light-Emitting Diodes with High Performance," *Adv. Mater.*, vol. 30, no. 25, p. 1800251, 2018.

23. L. Zhao, K. Roh, S. Kacmoli, K. Al Kurdi, S. Jhulki, S. Barlow, S. R. Marder, C. Gmachl, and B. P. Rand, "Thermal Management Enables Bright and Stable Perovskite Light-Emitting

Diodes," *Adv. Mater.*, vol. 32, no. 25, p. 2000752, 2020.

24. A. Onno, C. Chen, P. Koswatta, M. Boccard, and Z. C. Holman, "Passivation, conductivity, and selectivity in solar cell contacts: Concepts and simulations based on a unified partial-resistances framework," *Journal of Applied Physics*, vol. 126, no. 18, p. 183103, 2019.

25. M. Leskelä and M. Ritala, "Atomic Layer Deposition Chemistry: Recent Developments and Future Challenges," *Angew. Chem. Int. Ed.*, vol. 42, no. 45, pp. 5548–5554, 2003.

26. S. M. George, "Atomic Layer Deposition: An Overview," *Chem. Rev.*, vol. 110, no. 1, pp. 111–131, 2010.

27. R. W. Johnson, A. Hultqvist, and S. F. Bent, "A brief review of atomic layer deposition: from fundamentals to applications," *Materials Today*, vol. 17, no. 5, pp. 236–246, 2014.

28. M. J. Biercuk, D. J. Monsma, C. M. Marcus, J. S. Becker, and R. G. Gordon, "Low-temperature atomic-layer-deposition lift-off method for microelectronic and nanoelectronic applications," *Appl. Phys. Lett.*, vol. 83, no. 12, pp. 2405–2407, 2003.

29. P. O. Oviroh, R. Akbarzadeh, D. Pan, R. A. M. Coetzee, and T.-C. Jen, "New development of atomic layer deposition: processes, methods and applications," *Science and Technology of Advanced Materials*, vol. 20, no. 1, pp. 465–496, 2019.

30. J. Jeong, F. Laiwalla, J. Lee, R. Ritasalo, M. Pudas, L. Larson, V. Leung, and A. Nurmikko, "Conformal Hermetic Sealing of Wireless Microelectronic Implantable Chiplets by Multilayered Atomic Layer Deposition (ALD)," *Adv. Funct. Mater.*, vol. 29, no. 5, p. 1806440, 2019.

31. C.-Y. Chang, K.-T. Lee, W.-K. Huang, H.-Y. Siao, and Y.-C. Chang, "High-Performance, Air-Stable, Low-Temperature Processed Semitransparent Perovskite Solar Cells Enabled by Atomic Layer Deposition," *Chem. Mater.*, vol. 27, no. 14, pp. 5122–5130, 2015.

32. H. M. Yates, M. Afzaal, A. Walter, J. L. Hodgkinson, S.-J. Moon, D. Sacchetto, M. Bräuninger, B. Niesen, S. Nicolay, M. McCarthy, M. E. Pemble, I. M. Povey, and C. Ballif, "Progression towards high efficiency perovskite solar cells via optimisation of the front electrode and blocking layer," *J. Mater. Chem. C*, vol. 4, no. 47, pp. 11269–11277, 2016.

33. A. F. Palmstrom, G. E. Eperon, T. Leijtens, R. Prasanna, S. N. Habisreutinger, W. Nemeth, E. A. Gaulding, S. P. Dunfield, M. Reese, S. Nanayakkara, T. Moot, J. Werner, J. Liu, B. To, S. T. Christensen, M. D. McGehee, M. F. van Hest, J. M. Luther, J. J. Berry, and D. T. Moore, "Enabling Flexible All-Perovskite Tandem Solar Cells," *Joule*, vol. 3, no. 9, pp. 2193–2204, 2019.

34. R. Lin, J. Xu, M. Wei, Y. Wang, Z. Qin, Z. Liu, J. Wu, K. Xiao, B. Chen, S. M. Park, G. Chen, H. R. Atapattu, K. R. Graham, J. Xu, J. Zhu, L. Li, C. Zhang, E. H. Sargent, and H. Tan, "All-perovskite tandem solar cells with improved grain surface passivation," *Nature*, vol. 603, no. 7899, pp. 73–78, 2022.

35. M. Kot, C. Das, Z. Wang, K. Henkel, Z. Rouissi, K. Wojciechowski, H. J. Snaith, and D. Schmeisser, "Room-Temperature Atomic Layer Deposition of Al $_2$ O $_3$: Impact on Efficiency, Stability and Surface Properties in Perovskite Solar Cells," *ChemSusChem*, vol. 9, no. 24, pp. 3401–3406, 2016.

36. M. M. McCarthy, A. Walter, S.-J. Moon, N. K. Noel, S. O'Brien, M. E. Pemble, S. Nicolay, B. Wenger, H. J. Snaith, and I. M. Povey, "Atomic Layer Deposited Electron Transport Layers in Efficient Organometallic Halide Perovskite Devices," *MRS Advances*, vol. 3, no. 51, pp. 3075–3084, 2018.

37. J. W. Elam, C. A. Wilson, M. Schuisky, Z. A. Sechrist, and S. M. George, "Improved nucleation of TiN atomic layer deposition films on SiLK low-k polymer dielectric using an Al2O3 atomic layer deposition adhesion layer," *J. Vac. Sci. Technol. B*, vol. 21, no. 3, 2003.

38. J. D. Ferguson, A. W. Weimer, and S. M. George, "Atomic Layer Deposition of Al $_2$ O $_3$ Films

on Polyethylene Particles," *Chem. Mater.*, vol. 16, no. 26, pp. 5602–5609, 2004.

39. C. A. Wilson, R. K. Grubbs, and S. M. George, "Nucleation and Growth during Al $_2$ O $_3$ Atomic Layer Deposition on Polymers," *Chem. Mater.*, vol. 17, no. 23, pp. 5625–5634, 2005.

40. M. D. Groner, S. M. George, R. S. McLean, and P. F. Carcia, "Gas diffusion barriers on polymers using Al2O3 atomic layer deposition," *Appl. Phys. Lett.*, vol. 88, no. 5, p. 051907, 2006.

41. M. Weber, A. Julbe, S. S. Kim, and M. Bechelany, "Atomic layer deposition (ALD) on inorganic or polymeric membranes," *Journal of Applied Physics*, vol. 126, no. 4, p. 041101, 2019.

42. R. R. Petit, J. Li, B. Van de Voorde, S. Van Vlierberghe, P. F. Smet, and C. Detavernier, "Atomic Layer Deposition on Polymer Thin Films: On the Role of Precursor Infiltration and Reactivity," *ACS Appl. Mater. Interfaces*, vol. 13, no. 38, pp. 46151–46163, 2021.

43. R. L. Puurunen, "Surface chemistry of atomic layer deposition: A case study for the trimethylaluminum/water process," *Journal of Applied Physics*, vol. 97, no. 12, p. 121301, 2005.

44. A. J. M. Mackus, A. A. Bol, and W. M. M. Kessels, "The use of atomic layer deposition in advanced nanopatterning," *Nanoscale*, vol. 6, no. 19, pp. 10941–10960, 2014.

45. K. J. Park, J. M. Doub, T. Gougousi, and G. N. Parsons, "Microcontact patterning of ruthenium gate electrodes by selective area atomic layer deposition," *Appl. Phys. Lett.*, vol. 86, no. 5, p. 051903, 2005.

46. R. Chen, H. Kim, P. C. McIntyre, D. W. Porter, and S. F. Bent, "Achieving area-selective atomic layer deposition on patterned substrates by selective surface modification," *Appl. Phys. Lett.*, vol. 86, no. 19, p. 191910, 2005.

47. R. Chen and S. F. Bent, "Chemistry for Positive Pattern Transfer Using Area-Selective Atomic Layer Deposition," *Adv. Mater.*, vol. 18, no. 8, pp. 1086–1090, 2006.

48. K. S. Park, E. K. Seo, Y. R. Do, K. Kim, and M. M. Sung, "Light Stamping Lithography: Microcontact Printing without Inks," *J. Am. Chem. Soc.*, vol. 128, no. 3, pp. 858–865, 2006.

49. V. Suresh, M. S. Huang, M. P. Srinivasan, C. Guan, H. J. Fan, and S. Krishnamoorthy, "Robust, High-Density Zinc Oxide Nanoarrays by Nanoimprint Lithography-Assisted Area-Selective Atomic Layer Deposition," *J. Phys. Chem. C*, vol. 116, no. 44, pp. 23729–23734, 2012.

50. S. McDonnell, R. C. Longo, O. Seitz, J. B. Ballard, G. Mordi, D. Dick, J. H. G. Owen, J. N. Randall, J. Kim, Y. J. Chabal, K. Cho, and R. M. Wallace, "Controlling the Atomic Layer Deposition of Titanium Dioxide on Silicon: Dependence on Surface Termination," *J. Phys. Chem. C*, vol. 117, no. 39, pp. 20250–20259, 2013.

51. N. F. W. Thissen, R. H. J. Vervuurt, A. J. M. Mackus, J. J. L. Mulders, J.-W. Weber, W. M. M. Kessels, and A. A. Bol, "Graphene devices with bottom-up contacts by area-selective atomic layer deposition," *2D Mater.*, vol. 4, no. 2, p. 025046, 2017.

52. A. J. M. Mackus, M. J. M. Merkx, and W. M. M. Kessels, "From the Bottom-Up: Toward Area-Selective Atomic Layer Deposition with High Selectivity," *Chem. Mater.*, vol. 31, no. 1, pp. 2–12, 2019.

53. A. Sinha, D. W. Hess, and C. L. Henderson, "Area selective atomic layer deposition of titanium dioxide: Effect of precursor chemistry," *J. Vac. Sci. Technol. B*, vol. 24, no. 6, p. 2523, 2006.

54. A. Sinha, D. W. Hess, and C. L. Henderson, "Area-Selective ALD of Titanium Dioxide Using Lithographically Defined Poly(methyl methacrylate) Films," *J. Electrochem. Soc.*, vol. 153, no. 5, p. G465, 2006.

55. A. Sinha, D. W. Hess, and C. L. Henderson, "A Top Surface Imaging Method Using Area Selective ALD on Chemically Amplified Polymer Photoresist Films," *Electrochem. Solid-State Lett.*, vol. 9, no. 11, p. G330, 2006.

56. A. Sinha, D. W. Hess, and C. L. Henderson, "Transport behavior of atomic layer deposition precursors through polymer masking layers: Influence on area selective atomic layer deposition," *J. Vac. Sci. Technol. B*, vol. 25, no. 5, p. 1721, 2007.

57. M. N. Mullings, H.-B.-R. Lee, N. Marchack, X. Jiang, Z. Chen, Y. Gorlin, K.-P. Lin, and S. F. Bent, "Area Selective Atomic Layer Deposition by Microcontact Printing with a Water-Soluble Polymer," *J. Electrochem. Soc.*, vol. 157, no. 12, p. D600, 2010.

58. M. H. Park, Y. J. Jang, H. M. Sung-Suh, and M. M. Sung, "Selective Atomic Layer Deposition of Titanium Oxide on Patterned Self-Assembled Monolayers Formed by Microcontact Printing," *Langmuir*, vol. 20, no. 6, pp. 2257–2260, 2004.

59. X. Jiang and S. F. Bent, "Area-Selective ALD with Soft Lithographic Methods: Using Self-Assembled Monolayers to Direct Film Deposition," *J. Phys. Chem. C*, vol. 113, no. 41, pp. 17613–17625, 2009.

60. J. Huang, M. Lee, and J. Kim, "Selective atomic layer deposition with electron-beam patterned self-assembled monolayers," *Journal of Vacuum Science & Technology A: Vacuum, Surfaces, and Films*, vol. 30, no. 1, p. 01A128, 2012.

61. H. C. Guo, E. Ye, Z. Li, M.-Y. Han, and X. J. Loh, "Recent progress of atomic layer deposition on polymeric materials," *Materials Science and Engineering: C*, vol. 70, pp. 1182–1191, 2017.

62. X. Yang, X. Zhang, J. Deng, Z. Chu, Q. Jiang, J. Meng, P. Wang, L. Zhang, Z. Yin, and J. You, "Efficient green light-emitting diodes based on quasi-two-dimensional composition and phase engineered perovskite with surface passivation," *Nat Commun*, vol. 9, no. 1, p. 570, 2018.

63. M. H. Futscher, M. K. Gangishetty, D. N. Congreve, and B. Ehrler, "Manganese Doping Stabilizes Perovskite Light-Emitting Diodes by Reducing Ion Migration," *ACS Appl. Electron. Mater.*, vol. 2, no. 6, pp. 1522–1528, 2020.

64. J. H. Warby, B. Wenger, A. J. Ramadan, R. D. J. Oliver, H. C. Sansom, A. R. Marshall, and H. J. Snaith, "Revealing Factors Influencing the Operational Stability of Perovskite Light-Emitting Diodes," *ACS Nano*, vol. 14, no. 7, pp. 8855–8865, 2020.

65. B. Zhao, Y. Lian, L. Cui, G. Divitini, G. Kusch, E. Ruggeri, F. Auras, W. Li, D. Yang, B. Zhu, R. A. Oliver, J. L. MacManus-Driscoll, S. D. Stranks, D. Di, and R. H. Friend, "Efficient light-emitting diodes from mixed-dimensional perovskites on a fluoride interface," *Nat Electron*, vol. 3, no. 11, pp. 704–710, 2020.

66. C. Cho and N. C. Greenham, "Computational Study of Dipole Radiation in Re-Absorbing Perovskite Semiconductors for Optoelectronics," *Adv. Sci.*, vol. 8, no. 4, p. 2003559, 2021.

67. P. Poodt, D. C. Cameron, E. Dickey, S. M. George, V. Kuznetsov, G. N. Parsons, F. Roozeboom, G. Sundaram, and A. Vermeer, "Spatial atomic layer deposition: A route towards further industrialization of atomic layer deposition," *Journal of Vacuum Science & Technology A: Vacuum, Surfaces, and Films*, vol. 30, no. 1, p. 010802, 2012.

CHAPTER 7

Thesis Conclusion

The work presented in this thesis has, in the broad sense, treated two different topics: 2 eV halide perovskite solar cells and green halide perovskite LEDs. The wider context for the motivation to research these topics was laid out in Chapter 1, where we briefly explored the the pressing need for a pivot of the energy system towards renewable energy sources and the advantages of photovoltaic solar cells. We discussed the potential for perovskite photovoltaic technologies to add additional value to the solar energy value chain by providing relatively cheap and abundant materials that could be used in tandem or multijunction architectures (with our without silicon), or for lightweight or flexible cells in niche applications. We also saw that halide perovskite have proven promising also for LEDs, and thus there is a motivation also to explore this realm.

In Chapter 2, we reviewed the progress on perovskite triple-junctions, 2 eV absorbers, and the understanding of the very relevant phenomenon of halide segregation. It was clear that the progress on triple-junction solar cells using perovskite absorbers in one or more subcells was trailing far behind that of the double-junction (tandem) counterparts,

and that the same could be said for 2 eV absorbers, on the development of which only a few reports have been published. For researchers, this field then provides a blank canvas open for exploration. Given the high bromide content required to reach 2 eV bandgap with the more typical (multication) FA-based absorbers used for the wide-gap subcell in tandem configurations, it is not unlikely that the development of 2 eV absorbers will take a very different path – as well exemplified by the recent record by Wang et al. using an all-inorganic absorber, which we discussed in Section 2.2. In Chapter 2 we also reviewed the important concepts of quasi-Fermi level splitting and reciprocity between the photovoltaic and light-emitting operation modes.

In Chapter 4, we inspected the magnitude of different losses that make our best neat-FA solar cells deliver power conversion efficiencies at just about half the theoretical maximum stipulated by detailed balance calculations. We saw that the losses were quite equally distributed among the three parameters: FF, J_{SC} and V_{OC}. We then did an investigation into the various contributions to V_{OC} loss and found that nonradiative recombination in the bulk absorber material was the largest culprit by far, followed by nonradiative recombination at the interface with the n-contact. We also did an investigation into the losses caused by halide segregation and found that, although there is a negative effect on V_{OC}, this effect is not as large as the two aforementioned main V_{OC}-losses. On the other hand, our data suggested that J_{SC} was significantly hampered by halide segregation and/or other degradation phenomena under operation, and this could be a much larger issue for the long-term operation of these solar cells.

In Chapter 5, we looked further into the topic of halide segregation and light-induced degradation of 2 eV solar absorbers, but this time on isolated films rather than devices. We saw that the kinetics and spectral evolution of halide segregation was very atmosphere-dependent. Not only dependent on the measurement atmosphere, but also on the history of the sample's atmospheric exposure during dark storage. Most notably, with exposure to oxygen and/or humidity we saw the development of photoluminescence at wavelengths intermediate to the mixed, majority-phase

photoluminescence (shorter wavelengths) and the conventional, fully-segregated photoluminescence (longer wavelengths). This intermediate-wavelength luminescence tended to grow very bright. We also saw that if samples were kept under light for days in ambient air, there was an iodide depletion, resulting in an $FAPbBr_3$-like structure, and the growth of a Pb(OH)Br impurity phase. We postulated that the observation of intermediate-wavelength photoluminescence could be related to iodide-depletion and that growth of Pb(OH)Br along, e.g., grain boundaries, could serve to passivate the perovskite material and lead to the increased brightness.

Finally, in Chapter 6, we found that the p-contact in our green perovskite LEDs was prone to leakage current due to nonradiative recombination at the interface between ITO and perovskite in areas where the ITO was not sufficiently covered by the hole-transporting polymer TFB. We rectified this issue by making a TFB-Al_2O_3 composite using ALD to deposit the Al_2O_3. The ALD-Al_2O_3 process would effectively react with any bare ITO patches and, additionally, we saw evidence of swelling of the polymer-film, indicating likely growth of Al_2O_3 particulates within TFB porosities. Both mechanisms would lead to a better coverage of the ITO film, and we saw an improvement in the efficiency of our LEDs.

To summarize, we have made some initial investigations into the burgeoning field of 2 eV perovskite solar absorbers that highlight some interesting phenomena and important challenges to address. Although we have not managed to obtain clear answers on the cause of the observed halide-segregation and degradation phenomena, nor the exact determination of the negative effects of halide segregation, this work provides a clear imperative that these are issues that should be further addressed by the research community in the near future. The work on our composite TFB-Al_2O_3 p-contact for our LEDs can also be expanded on by the community in the years to come. In one aspect, the idea could be ported to other applications or other combinations of polymers and metals that can be deposited by ALD. In another aspect, our work does not investigate in detail any chemical or electronic effects occurring between the TFB

and the Al_2O_3 that could alter the properties of the pristine material, and this would be an interesting topic for investigation.

In order for monolithic perovskite triple-junctions to reach commercially viable quality, with high efficiency that can justify the increased manufacturing and research cost and with good stability, a few key issues need to be addressed. One, a higher radiative efficiency is required, especially through improved interfaces with the n-contact, but also by improvement of the bulk absorber material. Two, currently observed losses induced during operation need to be understood and rectified. In particular, this relates to the strong decrease in J_{SC}. Three, the solutions to the abovementioned issues need to be implemented in a way that is compatible with the fabrication of a monolithic device. That is, for silicon–perovskite–perovskite devices the fabrication of the 2 eV top cell must not damage the underlying middle cell, and for all-perovskite triple-junctions (typically deposited in order top cell to bottom cell) the 2 eV cell must be sufficiently smooth that it does not cause issues for the fabrication of the subsequent cells, and sufficiently robust that the top cell will not take damage during the remaining processing. In the eye of the author, these should be attainable targets for the research community and industry to reach. The two main questions – with which this thesis also ends – are: How long will it take? And, will the gain with respect to two-junction cells be sufficient to make the economics favourable?